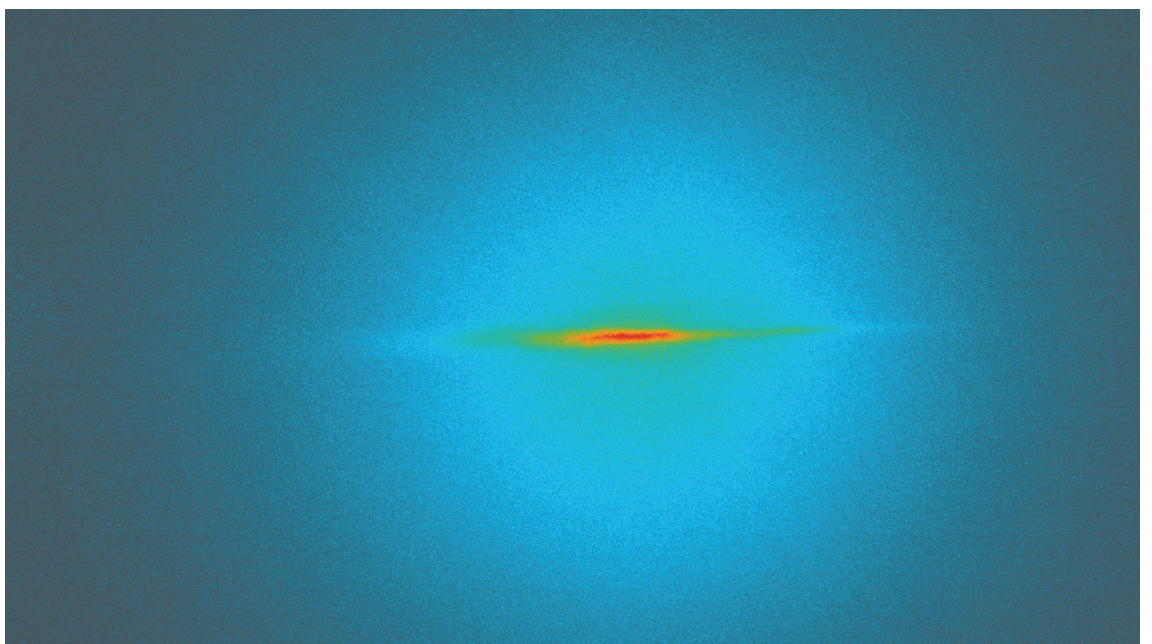


An Optical Dipole Trap in Microgravity

Dem Fachbereich 1 (Physik und Elektrotechnik)
der **Universität Bremen**
zur Erlangung des akademischen Grades
Doktor der Naturwissenschaften (Dr. rer. nat.)
vorgelegte Dissertation von
Christian Vogt, M. Sc.



PRIMUS



1. Gutachter : Claus Lämmerzahl
2. Gutachter : Ernst M. Rasel
Prüfer : Andreas Rosenauer
Prüfer : Dennis Schlippert

Tag der mündlichen Prüfung: 26.04.2019

Abstract:

An Optical Dipole Trap in Microgravity

Optical interferometers are well known for their high precision in several measurement situations. They are based on a readout of phase differences between optical path length. In contrast, atom interferometers rely on the De Broglie wavelength of atoms and their corresponding phase. A cloud of atoms is split and recombined with light pulses, while in between, the atoms are moving freely. These precise quantum tools will enhance a broad variety of measurements, ranging from large scale phenomena like gravitational wave detection to short scale Casimir-Polder forces and everything in between.

The sensitivity of atom interferometers scales with the time squared between light pulses, which is generally limited by gravity and temperature. One technical challenging solution is the realization of atom interferometers in microgravity. While ultra cold atoms can be prepared in optical and magnetic traps, under weightlessness their preparation is limited to magnetic traps until now. These experiments are based on atom chips with highly asymmetric trapping potentials. The improved symmetry of optical traps can improve the most advanced cooling technique, called delta kick collimation, leading to atomic clouds in the yet unreachable femtokelvin range.

This thesis is about the first realization of an optical trapping potential in microgravity. It describes the experimental setup, identifies a molasses technique as the optimal process for dipole trap loading and investigates the further cooling process under the influence and in the absence of gravity.

In optical and magnetic traps, the preparation of ultracold atoms is based on evaporation. However, the underlying physics to drive this process are fundamentally different and for optical traps, evaporation is driven by gravity. It is demonstrated that evaporation from an optical potential performs approximately equal with and without gravity, due to a strong mixing of the trapping potentials in all three spatial dimensions. These findings are confirmed with computational simulations, based on the *Direct Simulation Monte Carlo* method.

Atomic ensembles of rubidium-87 with temperatures as low as ≈ 300 nK were generated in the microgravity environment of the drop tower in Bremen with an evaporation time as short as 0.5 s. The final confining trap was too shallow to be reproduced in a laboratory environment. The findings of this thesis will possibly guide the way to improved atom interferometers, with countless applications in precise sensing. Furthermore, optical potentials in microgravity on their own will open up a broad field of fundamental physical experiments. One example is the applicability of magnetic Feshbach resonances. Allowing almost arbitrary tuning of the interatomic scattering length offers new insights in scattering processes or miscibility scenarios.

Zusammenfassung:

Eine optische Dipolfalle in Schwerelosigkeit

Optische Interferometer sind für ihre hohe Präzision bekannt. Sie basieren auf der Detektion von Phasendifferenzen zwischen verschiedenen optischen Wegen. Atom Interferometer messen hingegen die Phase der atomaren De Broglie Wellenlänge. Dabei wird eine Atomwolke mit Hilfe von Lichtpulsen gespalten und wieder überlagert, während sich die Atome zwischen den Pulsen frei bewegen. Dieses präzise Quantenwerkzeug wird eine breite Palette von Messungen verbessern, von langreichweitigen Phänomenen wie der Gravitationswellendetektion bis hin zur kurzreichweitigen Casimir-Polder-Kraft.

Die Empfindlichkeit von Atominterferometern skaliert dabei quadratisch mit der Zeit, die zwischen den Lichtimpulsen vergeht. Diese wird im Allgemeinen durch Schwerkraft und Temperatur begrenzt. Eine technisch anspruchsvolle Lösung ist die Realisierung von Atominterferometern in Schwerelosigkeit. Ultrakalte Atome können grundsätzlich in optischen und magnetischen Fallen generiert werden. In Schwerelosigkeit ist ihre Herstellung bisher jedoch auf magnetische Fallen beschränkt, die auf Atomchips mit stark asymmetrischem Atomfallen basieren. Durch die Verwendung optischer Potentiale, mit deutlich erhöhter Symmetrie, wird eine Verbesserung der Delta-Kick-Kollimationstechnik erwartet. Hierdurch rücken bisher unerreichbare Temperaturen im Bereich von Femtokelvin in greifbare Nähe.

Diese Arbeit beschäftigt sich mit der ersten Realisierung einer rein optischen Atomfalle in Mikrogravitation. Der Versuchsaufbau wird beschrieben, eine Melasstechnik als optimaler Ladeprozess für die optische Dipolfalle identifiziert und der weitere Kühlprozess mit und ohne Einfluss der Gravitation untersucht.

Sowohl in optischen, als auch in magnetischen Fallen, basiert die Herstellung ultrakalter Atome auf der Verdampfungskühlung. Die Umsetzung dieser Prozesse ist jedoch grundlegend verschieden. Obwohl bei optischen Fallen am Boden die Evaporation durch die Schwerkraft getrieben wird, konnte gezeigt werden, dass die Verdampfung aus einem optischen Potential mit und ohne Schwerkraft in etwa gleich verläuft. Dies kann auf ein starkes Mischen der Potentiale in allen drei räumlichen Dimensionen zurückgeführt werden. Dieses Erkenntnis wird durch Simulationen bestätigt, die auf der direkten Simulation Monte Carlo-Methode beruhen.

Atomare Ensembles aus Rubidium-87 mit Temperaturen bis hin zu 300 nK wurden in der Mikrogravitationsumgebung des Fallturms in Bremen mit einer Evaporationszeit von nur 0,5 s erzeugt. Dabei war das finale Fallenpotential so flach, dass es unter dem Einfluss der Gravitation unmöglich reproduziert werden kann.

Die Ergebnisse dieser Arbeit legen den Grundstein zur Verbesserung von Atominterferometern, mit unzähligen Anwendungen für eine Vielzahl von Präzisionsmessungen. Darüber hinaus eröffnen optische Potenziale in Schwerelosigkeit ein breites Feld physikalischer Experimente. Ein Beispiel wäre die Verwendung magnetischer Feshbach-Resonanzen. Sie erlauben eine nahezu beliebige Wahl der interatomaren Streulänge und damit eine eingehende Untersuchung von Streuprozesse oder Mischungsverhalten.

Contents

1. Introduction	15
1.1. The PRIMUS Project	20
1.2. The scope of this thesis	23
2. Experimental Setup	25
2.1. Laser systems	25
2.2. Vacuum chamber	28
2.2.1. Ovens	28
2.2.2. Source chamber	29
2.2.3. Science chamber	30
2.2.4. The pumping section	30
2.3. Dipole trap laser	33
2.4. Electronics	34
2.4.1. FPGA system	34
2.4.2. Camera computer	37
2.4.3. Control room computer	38
2.5. Operation in weightlessness	38
3. Dipole Trap Loading	41
3.1. The Magneto-Optical Trap	42
3.2. The Optical Dipole Potential	45
3.3. Dipole Trap Loading Schemes	51
3.3.1. Loading from a Magnetic Trap	52
3.3.2. Overlapping MOT and Dipole Trap	53
3.3.3. Loading Directly from the MOT	55
3.3.4. Loading from a Compressed MOT	57
3.3.5. Loading from an Optical Molasses	62
3.3.6. Loading from an Optical Lattice	65
3.4. Determination of Trap Frequencies	66
4. Evaporation in a Dipole Trap	69
4.1. Evaporative Cooling	69
4.1.1. Collisions and Losses	70
4.1.2. Lifetime Measurements	73

Contents

4.2. Simulation techniques overview	76
4.2.1. Doyle's method	76
4.2.2. Discrete evaporation steps	77
4.2.3. Trajectory simulation	77
4.2.4. Truncated Boltzmann distribution	78
4.2.5. Scaling laws	79
4.2.6. Discrete Simulation Monte Carlo (DSMC)	80
4.3. Implementation of the DSMC Method	81
4.4. Dimension of Evaporation	84
4.5. Evaporation in a Single Beam Dipole Trap	86
4.6. Single Beam Evaporation in Microgravity	91
4.7. Improved Evaporation Concepts	95
4.7.1. Crossed Dipole Trap	95
4.7.2. Moving Lenses	98
4.7.3. Lattice Enhanced Cooling	99
4.7.4. Painted Potentials	100
4.7.5. Feshbach Enhanced Rethermalization	102
4.7.6. Hybrid Trap	104
4.7.7. Conclusion to Improved Evaporation Concepts	107
4.8. Realization of a Crossed Dipole Trap	108
5. Conclusion	113
6. Outlook	115
Bibliography	121
A. Danksagung	143

Contents

List of repeated Symbols

a	Average energy carried away by an evaporated atom
a_0	Bohr radius
a_1 and a_2	Acceleration of test bodies
a_s	S-wave scattering length
c	Speed of light
e	Electric charge
g	Gravitational acceleration
I	Laser intensity
k_{eff}	Effective wave vector in AI beams
k_B	Boltzmann constant
L_{3B}	Rate coefficient for three-body recombination
m	The mass of a trapped atom
m_e	Electron mass
N	Particle number
N_{MOT}	Atom number in the MOT
N_T	Number of trapped atoms
n	Atomic density
n_0	Atomic peak density
PSD	Phase space density
$R_{0\text{MOT}}$	Initial MOT loading rate
r	Radial coordinate
U_0	Trap depth
U_{Dip}	Dipole trap potential
T	Temperature
T_0	Minimal achievable temperature in a molasses
t	time
t_{evo}	Free evolution time between laser pulses
\bar{v}	Average velocity
v_p	Most probable velocity in a Maxwell-Boltzmann distribution
w	Beam radius in Gaussian beam
w_0	Beam waist in Gaussian beam
x, y, z	Cartesian coordinates
y_{sag}	Gravitational sag
z_r	Rayleigh length

α	One-body loss coefficient
α_p	Complex polarizability
α_{fr}	Photon induced friction in a MOT
β	Two-body loss coefficient
Γ	On resonance damping rate
Γ_{1B}	One-body loss rate
Γ_{3B}	Three-body loss rate
Γ_{El}	Elastic collision rate
Γ_{sc}	Photon scattering rate
Γ_ω	Classical damping rate for radiative energy loss
γ	Three-body loss coefficient
γ_{CMOT}	Decay rate of a compressed MOT
γ_{eff}	Evaporation efficiency
Δ	Laser detuning from resonance
Δ_F	Width of a Feshbach resonance
Δ_{cool}	Cooling laser detuning
ϵ_0	Vacuum permittivity
η	Relative trap depth
$\eta_{E\ddot{o}t}$	Eötvös ratio
λ	Laser wavelength
σ	Elastic cross section
τ	Determines the speed of evaporation as exponent in power reduction curve
τ_{nev}	Lifetime contributed to natural evaporation
τ_{1B}	Lifetime contributed to one-body loss mechanisms
Φ_{light}	Laser induced accumulated phase in an Atom interferometer
Φ_{tot}	Total accumulated phase in an Atom interferometer
Φ_{path}	Accumulated phase in an Atom interferometer between light pulses
$\bar{\omega}$	Mean trap frequency
ω_{Res}	Atomic resonance frequency
ω_r	Radial trap frequency
$\omega_x, \omega_y, \omega_z$	One directional trap frequency
ω_L	Laser frequency

1. Introduction

We are living in the age of the second quantum revolution (Dowling et al. 2003). The first quantum revolution was about understanding the underlying rules of quantum mechanics. Observations like the particle-wave duality and other breakthroughs are the basis for our understanding of the periodic table, chemical interactions and solid state physics. These scientific achievements led to technical realizations like the laser and modern computers, the fundament of what is generally understood as *Information Age*. Throughout this time we were just observers of quantum effects.

Now is the time to engineer the quantum world to our needs, referred to as the second quantum revolution. An example for this would be the creation of Bose-Einstein condensates¹, a coherent state of matter possibly nowhere else found in the universe².

Several new research fields emerged from the new possibilities. Famous examples are quantum computing (Yanofsky 2007), quantum cryptography (Hughes et al. 1995), quantum clocks (Bize et al. 2005) and quantum metrology. While the goal of quantum computing is a machine that solves complex computational problems with multi-particle wave functions (Shenoy-Hejamadi et al. 2017), quantum cryptography will boost the level of security in confidential information transmission (Ladd et al. 2010). Quantum clocks have reached a stability where they would loose or gain at most a tenth of a second in the entire age of the universe (Marti et al. 2018).

Quantum metrology, also known as quantum sensing, is the science of enhancing measurement accuracies by applying quantum phenomena, such as entanglement or quantum squeezing (Andersen et al. 2016; Lvovsky 2016). One example for a quantum enhanced measurement is the LIGO detector for gravitational waves. This astonishing optical interferometer is able to observe length changes, 1/10.000th of a proton. For several decades precision measurements were based on interferometric schemes. The second quantum revolution now revealed a completely new type of interferometry, called atom interferometry (Cronin et al. 2009), where the role of light and matter is interchanged.

Atom Interferometry

Atom interferometry (AI) is a quantum tool that combines atoms as test masses, with the outstanding readout characteristics of interferometers. Furthermore, it comes with even shorter

¹The theoretical prediction can be found in (Bose 1924; Einstein 1924), first experimental realization in (Anderson et al. 1995; Bradley et al. 1995; K. B. Davis, Mewes, Andrews, et al. 1995).

²Calculations predict the possible existence of BECs in neutron stars

1. Introduction

wavelength than their optical counterparts, which is the basis for accurate measurements. In contrast to photons, atoms strongly interact with magnetic-, electric- and gravitational fields for example. Moreover, they are sensitive to inertial forces (Canuel et al. 2006). Accordingly, atom interferometers have demonstrated a broad range of measurements, such as a determination of the fine structure constant (Wicht et al. 2002; Parker et al. 2018), performance of absolute gravimetry (De Angelis et al. 2009; Peters et al. 1999; Abend et al. 2016), magnetometry (J. P. Davis et al. 2008; B. Barrett, Chan, et al. 2011), rotation measurements (Gustavson et al. 1997; Dutta et al. 2016) and tests of the weak equivalence principle (Schlippert et al. 2014; B. Barrett, L. Antoni-Micollier, et al. 2015).

In optical interferometers, light is split and recombined, giving intensity coded phase information about two different optical path lengths. Atom interferometry utilizes the same principles, making use of atomic wave-like behavior as described by the de Broglie wavelength. Here, light pulses act as splitter, mirror and recombiner for an atomic ensemble. A schematic atom

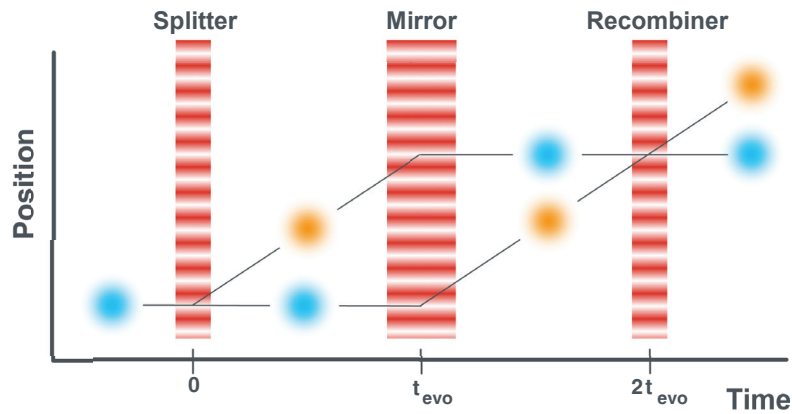


Figure 1.1

Schematic drawing of an atom interferometer in Mach-Zehnder configuration generated by three laser pulses. Light pulses split the wave function of an atom into an upper and a lower arm and recombine them. The assembled phase differences between both paths decide the atom's output port probability. Operating the atom interferometer with a cloud of atoms translates the probabilities into atom numbers. Note that there is only a vertical atomic movement, while the x axis shows temporal evolution.

interferometer is depicted in Figure 1.1. An atomic cloud, initially at rest, is illuminated with two counter propagating laser fields, driving oscillations between different atomic states. These transitions are based for example on Raman transitions³, where the temporal evolution for the population of a ground state $|g\rangle$ and an excited state $|e\rangle$ follow Rabi oscillations. An interaction time (and intensity) of exactly half a Rabi oscillation leads to a coherent and symmetric splitting of the atomic wave function. This means, a detection at this point would reveal half the atoms in the upper arm while the other half stayed at rest in the lower arm. After a free evolution time of

³Another common approach to drive these transitions is based on Bragg diffraction. Completely different approaches for beam splitting are based on the dipole force in a standing wave laser field (Rasel et al. 1995) or an adiabatic potential well splitting (Shin et al. 2004).

t_{evo} the light field is switched on again and drives half a Rabi oscillation. This so-called mirror pulse, reverses the atomic states for every atom, leaving the upper arm at rest and transferring momentum to atoms in the lower arm. The atoms are moving freely once again before they are recombined by the last laser pulse, driving half an oscillation again. The information of phase differences between both arms is now encoded in the population probability of both output ports.

Generally, the differential phase accumulated on both beam paths can be separated in a contribution from the free evolution time and a second one, originating from light interaction (Kasevich and Chu 1992; Storey et al. 1994):

$$\Delta\Phi_{\text{tot}} = \Delta\Phi_{\text{path}} + \Delta\Phi_{\text{light}}. \quad (1.1)$$

Focusing on gravitational measurements: the path contribution vanishes in a uniform gravitational field (A. Peters et al. 2001), resulting in an only laser driven differential phase of

$$\Delta\Phi = k_{\text{eff}} g t_{\text{evo}}^2, \quad (1.2)$$

where k_{eff} is the efficient wave number of the underlying two photon transition and g is the gravitational acceleration. Equation (1.2) identifies two parameters for measurement sensitivity improvements. One possibility is a high k_{eff} value, generated by so called large momentum beam splitters where multiple photons are transferred (Müller et al. 2008; Cladé et al. 2009). The second is a long free evolution time between light pulses, which are only possible with clouds of extremely cold atoms.

Atoms in an interferometer have to be protected from collisions that could affect their phase evolution. For this reason AIs are operated in high vacuum chambers, typically cm sized, while atoms at room temperature have velocities in the order of hundreds of meters per second. The simple derived picture is that atoms have to be measured before they hit any wall of the chamber.

A more detailed look reveals two further aspects to underline the importance of low cloud expansion rates:

- Atoms in interferometers are detected by scattered light or their *shadow*. Both methods demand a certain level of atomic density to function. The slower a non-trapped atomic ensemble expands, the longer its density stays high enough to be recorded.
- Since optical beams can be distorted by inaccuracies of the vacuum windows for example, they can not be considered as perfect plane wavefronts. These deviations get imprinted on the atoms and give an unwanted spatial dependency to the phase (Schkolnik et al. 2015). A reduced expansion rate minimizes this problem (Karcher et al. 2018).

1. Introduction

Low expansion rates are achieved by low temperatures of the atomic ensemble, velocity selective pulses (Kasevich, Weiss, et al. 1991; Biedermann et al. 2017) or additionally applied potentials either guiding the atoms (Akatsuka et al. 2017; Hilton et al. 2018) or slowing them down (Ammann et al. 1997; Hogan et al. 2015).

Regardless of the temperature, another aspect to prevent the realization of long evolution times is gravity. A perfectly cold cloud ($T = 0$) of atoms would not expand, but fall to the bottom of a vacuum chamber, where phase information is lost. Solutions to this problem are huge vacuum chambers, like the 10 m fountains located at Stanford (Dickerson et al. 2013) and Wuhan (Zhou, Xiong, et al. 2011), or an operation in weightlessness, also called microgravity due to residual accelerations.

Cold Atoms on Microgravity Platforms

While first realizations and proof of principle quantum technology devices were huge and heavy setups, they were downsized with deeper understanding of the underlying principles and technical developments. Examples for this are the realization of mobile gravimeters based on atom interferometry and an atomic clock that was operated in space (Liu et al. 2018).

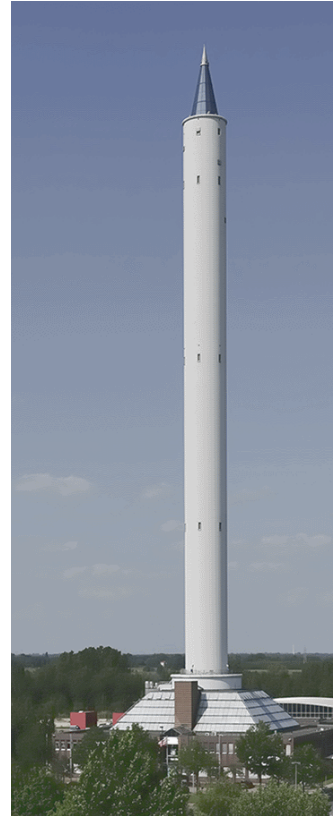


Figure 1.2
The drop tower in Bremen

On one hand, the tendency of building more and more compact devices will lead to commercial applications, e.g. inertial subsea navigation or the search for natural resources. On the other hand, mobile devices open up new possibilities for fundamental research. Experiments on cold atoms in microgravity will enable us to

- *reach even lower expansion rates*: The expansion of a cold atomic ensemble is directly linked to the confining trap it was released from. Shallow trap result in low expansion rates but they are not able to hold the atoms against gravity. In microgravity there are no limits to the trap depth.
- *increase the sensitivity of atom interferometers*: As discussed before, the sensitivity of an atom interferometer scales with the free evolution time squared, as mentioned in Equation 1.2. Long free evolution times can only be observed in microgravity.
- *investigate new phenomena*: Hollow Bose-Einstein condensates, for example, are expected

to exist in neutron stars but have never been realized experimentally due to gravity. They could be investigated in a microgravity environment.

Microgravity can be provided by several different platforms such as drop towers, parabolic flights, sounding rockets, space stations or on satellites. Apart from the last, cold atomic experiments are performed on all of them. The drop tower in Bremen (see Figure 1.2) provides 4.7 s of free fall with low residual accelerations in the range of 10^{-6} g. There, the first BEC- (Zoest et al. 2007) and atom interferometry (Münzinga et al. 2013) in microgravity were demonstrated by the QUANTUS-1 experiment. A second generation (QUANTUS-2) created the, coldest ensemble observed so far. They reached a three dimensional temperature equivalent as low as ≈ 70 pK (Sternke 2018).

In a parabolic flight the first dual species interferometer in microgravity could be demonstrated by the ICE experiment (B. Barrett, Laura Antoni-Micollier, et al. 2016). Generally parabolic flights provide longer microgravity times than drop towers but at the expense of worse quality with residual accelerations in the order of 10^{-2} g.

The first BEC in space was created by the MAIUS mission in 2017 on a sounding rocket (Becker et al. 2018). A peak height of 243 km provided 6 min of weightlessness at 10^{-4} g.

In May 2018 the cold atom laboratory CAL, a multi-user facility, was installed on the international space station. It provides prolonged microgravity times with a variety of residual accelerations depending, for example, on the astronaut's activities. At the time of writing, no results were published.

Almost all the introduced experiments are based on atom chips, providing purely magnetic atom traps. The only exception is the ICE project, which is operating at higher temperatures of several μ K, based on laser cooling. None of them is based on purely optical potentials.

Atom Chips and Dipole Traps

Atom chips are silicon waver with conducting wire structures on their surface (see Figure 1.3). Their magnetic trapping potential forms close to the wires. High magnetic gradients can be reached with relatively low currents and a low power consumption, which is desirable for compact setups and space applications.

Nevertheless, atom chips have several (possible) disadvantageous for future mission with increased sensitivity.

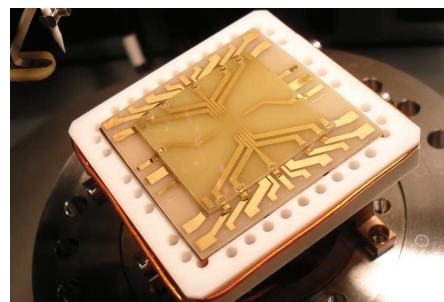


Figure 1.3
Example of an atom chip. The fine wire structures are too small to be seen in this picture. In addition to an external magnetic bias field, variable trapping geometries can be realized. (Image by: W. Herr)

1. Introduction

- A solid surface in the vicinity of cold atoms under investigation might lead to optical clipping problems. Precise manipulation of cold atoms is based on plane wavefronts, which get distorted when the beam is partially blocked or scattered.
- The glued atom chip structure may set a low level on vacuum quality, limiting the ensembles' lifetimes and possibly even exert a force on them, due to the imbalanced background atom source.
- A weak attractive force towards high temperature bodies was discovered (Haslinger et al. 2018), possibly affecting chip trapped atoms due to warm wire structures.
- A final concern is linked to a technique called delta-kick collimation (Castin et al. 1996; Ammann et al. 1997), where the expansion of cold atoms is reduced by applying a trapping field for a short time after some free evolution. Without further details, this technique requires an isotropic, ideally harmonic potential that can not be generated by atom chips. The problem is intrinsic, due the asymmetric setup itself.

Purely optical potentials, called optical dipole traps, may overcome all of these problems at the cost of other drawbacks, as discussed in this thesis.

1.1. The PRIMUS Project

The Einstein equivalence principle, the backbone of the theory of general relativity, is formed by the universality of gravitational red shift (UGR), the local validity of Lorentz invariance (LLI) and the universality of free fall (UFF) (C. M. Will 2009). The scope of PRIMUS (*Präzisions Interferometrie unter Schwerelosigkeit / Precision Interferometry in weightlessness*) are high precision atom interferometry measurements to test the validity of the UFF, in the drop tower in Bremen. The UFF, which is also known as the Einstein weak equivalence principle (WEP), describes gravity driven trajectories of test masses as independent of their composition, as long as self-gravity can be neglected⁴. This statement is tantamount to an equality between inertial and gravitational mass.

The specific search for violations of the equivalence principle is motivated by nothing less than a combined theory between the standard model and the theory of relativity. While the former describes electromagnetic, weak and strong interactions, the latter describes gravitational forces.

⁴In cases with self-gravity the strong equivalence principle is valid.

A unified theory for both has not been found yet. An simple example of the incompatibility can be found in the center of a black hole for example. While the massive object and it's surrounding space phenomena, such as gravitational lensing or the Lense–Thirring effect, are well described by the theory of general relativity, which predicts a point-like singularity at its center. Looking at this from a quantum point of view, a perfectly localized object is simply impossible and the conflict remains irresolvable in current theories.

Theories including violations of the WEP are for example the spin-0 dilaton in string theory (Damour 1994; Damour et al. 2002), chameleon fields (Khoury et al. 2004; Elder et al. 2016), an introduced light U boson (Fayet 2017), the gravitational standard model extension (Hohensee et al. 2013; Kostelecký et al. 2009) and spacetime fluctuations (Göklü et al. 2008). The validity of the Einstein equivalence principle has been tested for centuries, long before Einstein was born. The idea of mass equality dates back to the time of Galileo, testing gravity driven accelerations on tilted surfaces and Newton's experiments on pendulums. The test sensitivities are quantified through the Eötvös ratio

$$\eta_{\text{Eöt}} = 2 \frac{|a_1 - a_2|}{|a_1 + a_2|} \quad (1.3)$$

with the accelerations of two test bodies 1 and 2, where a valid WEP leads to a ratio of zero. The most precise ground based tests are operated on torsion pendulums and reach $\eta_{\text{Eöt}} = 0.3 \pm 1.8 \times 10^{-13}$ (Schlamminger et al. 2008; Wagner et al. 2012), while the absolute best result so far was achieved by the Microscope satellite with an Eötvös ratio of $\eta_{\text{Eöt}} = [-1 \pm 9(\text{stat}) \pm 9(\text{syst})] \times 10^{-15}$ comparing titanium and platinum cylinders as test bodies.

State of the art WEP tests with quantum objects demonstrated sensitivities of $\eta_{\text{Eöt}} = 1.0 \pm 1.4 \times 10^{-9}$ for test bodies in different hyperfine states (Rosi et al. 2017), $\eta_{\text{Eöt}} = 2.8 \pm 3.0 \times 10^{-8}$ for different isotopes of the same element (Zhou, Long, et al. 2015) and $\eta_{\text{Eöt}} = 0.3 \pm 5.4 \times 10^{-7}$ for different elements as test bodies (Schlippert et al. 2014). The number of stated results alone is giving an idea that the *one and only* test of the WEP is not possible. Quantum sensor based experiments are assumed to outperform classical tests in the future but since no one knows what exactly to search for, each separate experiment plays an important role in the endeavor of discovering new physics (Damour 1996). Following this strategy another spectacular approach is testing the free fall of antimatter (Kimura et al. 2015). Competitive space operated quantum based sensors are proposed with anticipated sensitivities of $\eta_{\text{Eöt}} = 1 \times 10^{-15}$ (Aguilera et al. 2014; Altschul et al. 2015) or even 5×10^{-16} (Williams et al. 2016).

The PRIMUS project was started as a complementary approach to the already existing experiments on cold atoms based on the atom chip technology. Therefore, it will perform WEP test with different atomic species, rubidium and potassium, but focuses strongly on the preparation of quantum test bodies in microgravity. This preparation will, in contrast to all other experiments in the drop tower, occur in an optical dipole trap. PRIMUS approaches to generate temperatures

1. Introduction

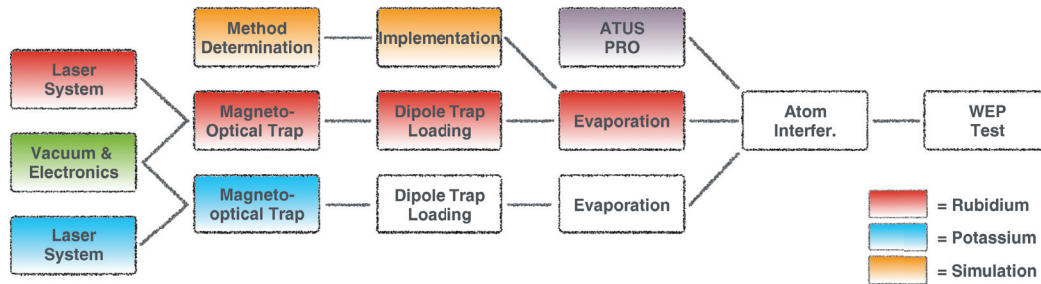


Figure 1.4

Reduced pictogram of the PRIMUS project milestones. Laser systems, vacuum chamber and electronics are assembled for rubidium and potassium. Rubidium can be trapped magneto-optically and optically on ground and in microgravity, followed by evaporative cooling. Potassium can be captured on ground in a three-dimensional MOT, simultaneously with or separate from rubidium. Simulations were implemented for the evaporation process, as well as for the atom interferometry. White boxes are open work packages.

below $1 \mu\text{K}$ in a purely optical potential, in microgravity.

This project is a collaboration between the Center of Applied Space Technology and Microgravity (ZARM) in Bremen and the Institute of Quantum Optics in Hannover and can generally be divided into four branches:

The Drop Tower Atom Interferometer: An atom interferometer to test the validity of the WEP in microgravity with an atomic ensemble prepared in an optical potential. This branch includes the green, red, blue and white boxes in Figure 1.4. A brief description of the set up follows in Chapter 2 and all experimental data discussed here originate from this experiment.

The Atlas Experiment: An experimental setup to test for violations of the WEP in most parts identical to what is planned in the drop tower but in a laboratory environment. It realized the, up to now, most precise validation of the WEP with two different atomic species (Schlippert et al. 2014). The experiment, operating for over a decade at the IQO in Hannover, joined PRIMUS in the current funding period in 2016.⁵

Theoretical Simulations: Theoretical support was delivered by the ATUS I and II (Atominterferometrie unter Schwerelosigkeit) projects, running in parallel with PRIMUS. In the third funding period both projects were united. The outcome is a C++ based open source program to solve the non linear Schrödinger equation, in particular the Gross-Pitaevskii equation (Stuckenberg et al. 2018; Marojević et al. 2016). The algorithm numerically simulates atom interferometry with Bose-Einstein condensates for different interaction processes like Bragg or Raman pulses (purple box in Figure 1.4)

Neither atom interferometry nor Bose-Einstein condensates are implemented in the drop tower experiment yet. For this reason, the C++ package could not be used in the context of this thesis. Numerical implementations for the evaporative cooling process were developed independently

⁵Before that, Atlas was a subcontractor to PRIMUS.

of the ATUS team and are discussed in Chapter 4.2. In Figure 1.4 these efforts are represented by the orange boxes.

A Stable Microwave Reference: The microwave reference branch is the oldest part of the PRIMUS project. A high finesse drop tower proof cavity was set up, providing an optically generated microwave reference, to precisely match the splitting beam frequencies in an atom interferometer, with the atoms respective hyperfine splitting. Furthermore, a frequency comb was planned to phase link Raman splitting pulses for different atomic species. This branch was discontinued since the need for these techniques, to gain high precision in atom interferometry, was outdated by the evolution of double diffraction (Lévêque et al. 2009).

The resulting highly stabilized laser system paves the way for other precision experiments in microgravity, such as optical clocks (Resch 2016).

The current status of the project is (partially) depicted in Figure 1.4. Separate laser systems for the optical cooling of rubidium and potassium with their respective electronics, and an ultra high vacuum chamber were assembled (Kulas 2016). Magneto-optical trapping could be realized for both species simultaneously (not in this thesis) and for rubidium even in microgravity. Furthermore, optical trapping and evaporation were applied with different trapping geometries in microgravity.

For simulations of the evaporation process, the flexible *Direct Simulation Monte Carlo* method and a fast calculation based on truncated Boltzmann distributions were identified as best choices for the given situations. Both were implemented in a *Matlab (Python)* code. For the simulation of expected atom optics, a simulation called ATUS PRO was prepared.

In the attempt to bring cold atom technology into space and perform ground breaking experiments, such as a possible violation of the weak equivalence principle, none of the mentioned experiments/projects can be looked at separately. A basic understanding has to be gained and new approaches have to be developed in laboratory environments, as in PRIMUS done by the ATLAS-experiment. These findings must be demonstrated and refined in microgravity environments with high repetition rates and great accessibility, like drop towers or parabolic flights and are the foundation for space missions on space stations, sounding rockets or satellites. As such, this thesis understands itself also as a guide for future space missions to effectively implement dipole trapping in space.

1.2. The scope of this thesis

In the bigger context of quantum gases in weightlessness this thesis portrays the first realization of a dipole trap, operating in microgravity. Its performance is analyzed and compared to ground based experiments. Furthermore, specific differences between both scenarios are investigated theoretically, using numerical simulations. Acting as a pathfinder experiment for future space

1. *Introduction*

missions the most effective way for evaporative cooling is identified, while keeping technical constraints in mind.

The thesis is organized as follows: The **second** chapter briefly describes the experimental setup assembled by the author and Sascha Kulas, ending with a short description of the drop tower in Bremen and how the system operates within it.

The **third**, chapter explains all cooling and trapping techniques prior to an evaporation, including the loading procedure of a dipole trap and its applications in microgravity. Chapter **four** deals with the process of evaporation from an optical potential. The technique of evaporative cooling is presented and simulation approaches are discussed. Experimental results with and without gravity are provided, followed by a theoretical investigation of more sophisticated evaporation techniques. The chapter closes with initial results for an improved evaporation strategy, a crossed dipole trap geometry. Finally, a conclusion of the presented results (Chapter **five**), and an outlook on future possibilities within the PRIMUS project and beyond (Chapter **six**), are given.

2. Experimental Setup

The entire experimental setup, designed to fit the characteristic drop tower demanded structure, can be seen in Figure 2.1. A cage system of 4 aluminum stringers houses seven aluminum/plywood/aluminum compound platforms, each with an area of 0.35 m^2 . For drop tower operation a hermetically sealed hull surrounds the capsule, providing atmospheric pressure while the tower itself is evacuated. The tip at the bottom of our structure reduces impact forces in the deceleration phase at the end of a drop.

The relatively complex system can be broken down into several subsystems and described separately, which is done in this chapter. Briefly, we are operating a 2D^+ -MOT (Magneto Optical Trap), to trap and cool atoms along two dimensions. The atoms are provided by heated atomic reservoirs, called ovens. The cooled atoms are transferred from the source vacuum chamber, to the science chamber, where we operate a 3D-MOT. In here, the atoms are loaded into an optical dipole trap.

All the information needed to understand the presented experimental results are given in this Thesis. For a deeper insight, a more detailed description can be found in (Kulas 2016).

2.1. Laser systems

All lasers, except for the dipole trap, are located on the uppermost platform of the system. These are the so called cooling and repumping lasers to cool atoms in a standard MOT configuration, a reference laser and two, in future needed Raman lasers to manipulate cooled atoms and perform atom interferometry. Similarly tasked lasers are integrated for potassium and rubidium. While both elements were operated in the system, this thesis focuses on experiments on rubidium only. Results for potassium can be found in a master thesis (Blanke 2016) written by Nena Blanke. In addition to the stated results in this reference, a double MOT with both species present at a time could be realized as a project milestone.

A schematic drawing of the rubidium laser system can be found in Figure 2.2. The reference laser, called master laser, is a DFB (Distributed Feedback) Diode, frequency locked to the atomic crossover transition $^2S_{1/2}, F = 3 \rightarrow ^2P_{3/2}, F' = 3, 4$ of rubidium-85 (Bjorklund et al. 1983). For this purpose a rubidium gas cell in a Doppler free saturation spectroscopy setup is installed. The master laser acts as a reference for the other lasers.

The same type of laser provides repumping light, resonant with the $F=1 \rightarrow F'=2$ transition of the rubidium-87 D-2 line. A MOPA (Master Oscillator Power Amplifier) manufactured by the FBH (Ferdinand-Braun-Institut, Leibniz-Institut für Höchstfrequenztechnik) provides the

2. Experimental Setup

cooling light. It provides up to 2 W of output power in the frequency range between the $F=2 \rightarrow F'=3$ transition and up to 200 MHz detuned to the red. Light from this laser is also used for fluorescent detection of atomic ensembles.

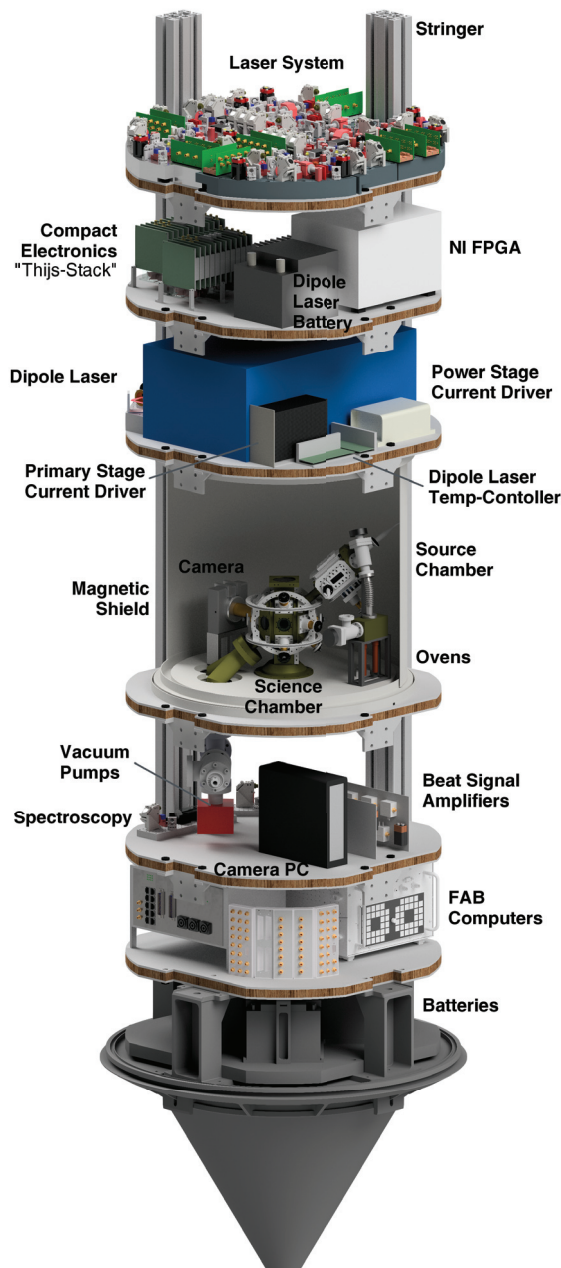


Figure 2.1
The entire experimental setup designed for drop tower operation.

The laser system itself is set up in a modular way on separate aluminum breadboards of 4 mm thickness, which are optically connected via fibers. The first module carries the above described lasers for laser cooling. A small fraction of light is guided to fast photo diodes where two beams are overlapped and form a beat signal, slow enough to enable a frequency stabilization. Cooling and repumping laser are, in contrast to the potassium system, referenced on the master laser. The major part of optical power is coupled into an optical fiber and guided to the next module, the distribution module. Here, both beams are separated individually into a beam for the 3D- and 2D-MOT. 2D cooling and repumping beams are overlapped, fed through an AOM (acousto-optic modulator) and coupled into the designated fiber leading to the science chamber. In the same way, except for separate AOMs, 3D light is coupled into the fiber leading to the science chamber. AOMs in the optical paths are used for intensity control. Since they are not able to block beams completely, both paths also feature a mechanical

shutter. A third module hosts the not yet used Raman laser system and all three modules are present for rubidium and potassium.

All of the above described system is mounted on aluminum breadboards where the bottom side is honeycomb structured, saving weight by providing a high mechanical stability, while 3 mm bolt holes in a rectangular pattern at 10 mm distance are placed on the top side, leading to a stable and highly compact optical system. Holders for optical elements such as mirrors, lenses or isolators were custom designed (Grzeschik 2017). Moving parts are spring-loaded and can be fixed with set screws. This design is mandatory for drop tower operation with its significant forces of up to 40 g acting on the system. A sufficient position stability, to conserve fiber coupling efficiencies under changing temperature conditions¹, is provided by water cooling. Copper heat sinks are directly bolted on the laser board structures. Furthermore a black anodized aluminum coverage surrounds the laser system. It serves as protection against environmental influences and laser safety feature for the experimentalists.

The generated laser light is guided from the laser board to the vacuum chamber via optical fiber

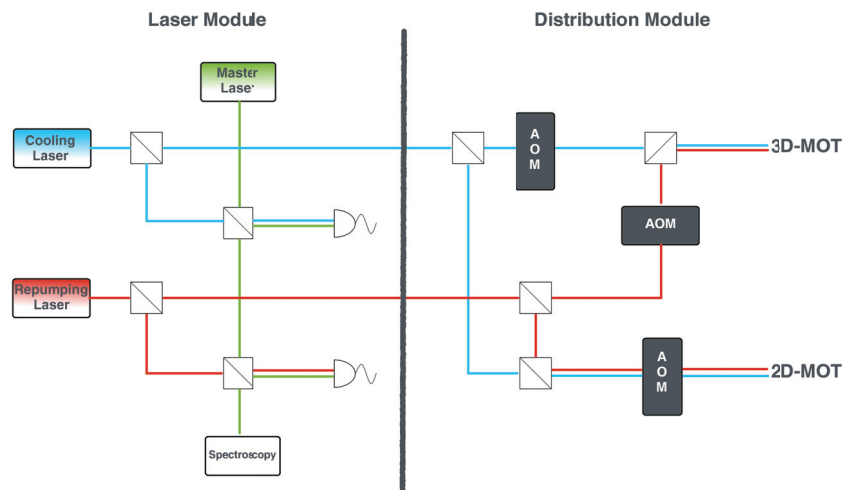


Figure 2.2

Schematic drawing of the laser light generation and distribution. Cooling and repumping laser are referenced to a master laser locked on a spectroscopy cell. Both beams are overlapped and send to the 3D- and 2D-MOT respectively. AOMs act as fast shutters.

splitters. A 2x6 splitter provides light for the standard 3D-MOT configuration in the science chamber for both atomic species. The source chamber is fed with laser light from a 2x4 splitter, with two main ports for the 2D-MOT in retro reflection configuration and two lower powered ports for additional pusher and retarder beams. This 2D⁺-MOT configuration provides a high atomic flux with a narrow velocity spread (Dieckmann et al. 1998).

¹The ambient temperatures in the laboratory and the drop tower can easily differ more than 10 °C.

2.2. Vacuum chamber

To perform experiments on cold or ultracold atoms, a vacuum system is needed to shield them from room temperature atoms, bringing energy into the system. The employed vacuum system can be divided into four subsystems, namely, the ovens, the source chamber, the science chamber and the pumping section.

In the ovens, atoms are released from a solid to gas phase. From here they diffuse into the source chamber where the $2D^+$ -MOT operates. In our science chamber, where the 3D-MOT is located, atoms are transferred into the dipole trap and get evaporated, while the pumping section assures a proper vacuum quality ($<10^{-9}$ hPa, see Section 4.1.2) for the entire system.

Apart from the highly magnetic pumping section, the vacuum system is equipped with a two layered magnetic shield made out of mu-metal. Its design is closely related to the concept used in the MAIUS mission (Kubelka-Lange et al. 2016; Kubelka-Lange 2017).

2.2.1. Ovens

Atoms are released from a heated reservoir, called oven. The main part is a homemade copper tube, closed on one end and with a Conflat sealing on the other. The design is similar to commercially available Pinch-Off-Tubes, as can be seen in Figure 2.3. The sealing is mounted into a bored blank flange, which is bolted against the vacuum chamber. A glass ampoule carrying either 1 g of rubidium or 1 g of potassium in its natural isotopic abundance is placed inside. It is inserted before the assembly of the oven, in environmental pressure conditions. Under sufficient vacuum conditions the tube is mechanically deformed, breaking the glass inside. This procedure allows to bake-out the oven section together with the rest of our vacuum system, which required for the low pressures needed.

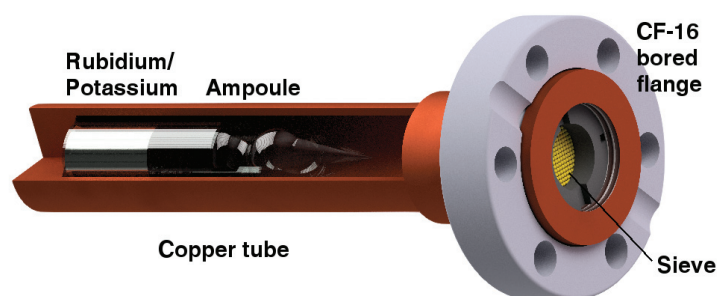


Figure 2.3

CAD drawing of the oven design. Parts of the copper tube are invisible in this picture to open up the view on the inserted glass ampoule. The number of interfaces is reduced, by designing the sealing as a part of the copper tube. This results in a robust and reliable system.

The amount of released atoms is governed by the element's vapor pressure and can be

manipulated by a heating wire on the outside of the copper tube, where higher temperatures lead to a higher atomic density. The operating temperature has to be carefully chosen, since a high density reduces the efficiency of a $2D^+$ -MOT due to additional collisions, a low density reduces the amount of trapped atoms. Furthermore, rubidium reacts with indium, which is used as sealing component for most of the vacuum windows. This was unknown in the planning phase of the vacuum setup but is reported from similar experimental setups as well. Even though the process is not fully understood, there seems to be a connection between rubidium pressure in the chamber and degradation time. Considering this the rubidium oven operates at about 40 °C.

To protect the vacuum system from glass splinters or liquid rubidium (potassium) a bronze sintered sieve is integrated at the oven's top. It consists of connected, sintered, balls with a diameter of approximately 1 mm. The resulting maximum size for particles to pass is 100 μm . Its feasibility to prevent liquid rubidium from penetrating has been experimentally verified (Seidel 2014).

Two of these ovens, one for each atomic species, are mounted onto a 5 way titanium block which is connected to the source chamber with a bellows and a valve, shown in Figure 2.5.

2.2.2. Source chamber

The source chamber is a titanium vacuum chamber with outer dimensions of 120 mm x 52 mm and the purpose to capture and precool atoms from the background vapour, provided by the ovens. With two retro reflected laser beams and four magnetic coils in racetrack configuration, atoms are magneto-optically trapped in two dimensions. Retro reflection approximately halves the demand on laser power, without significantly decreasing the MOTs performance. A possible power imbalance between incoming and reflected beam can be compensated for, by a slightly asymmetric magnetic field.

Since a $2D^+$ -MOT (Dieckmann et al. 1998) configuration is applied, in addition to the trapping beams, a pusher beam along the non trapped axis, pushes atoms towards the science chamber. To prevent atoms from getting too fast to be further trapped, a retarding beam along the opposite direction, decelerates them slightly. A differential pumping stage, a copper bolt with a small 1.5 mm hole in it, maintains a pressure difference between the source and the science chamber. In this design the $2D^+$ -MOT can operate at relatively high rubidium background pressure of approximately 10^{-9} mbar, without affecting atoms in the science chamber. Furthermore, it features a 45° angled surface to reflect the retarding beam into the desired direction.

2. Experimental Setup

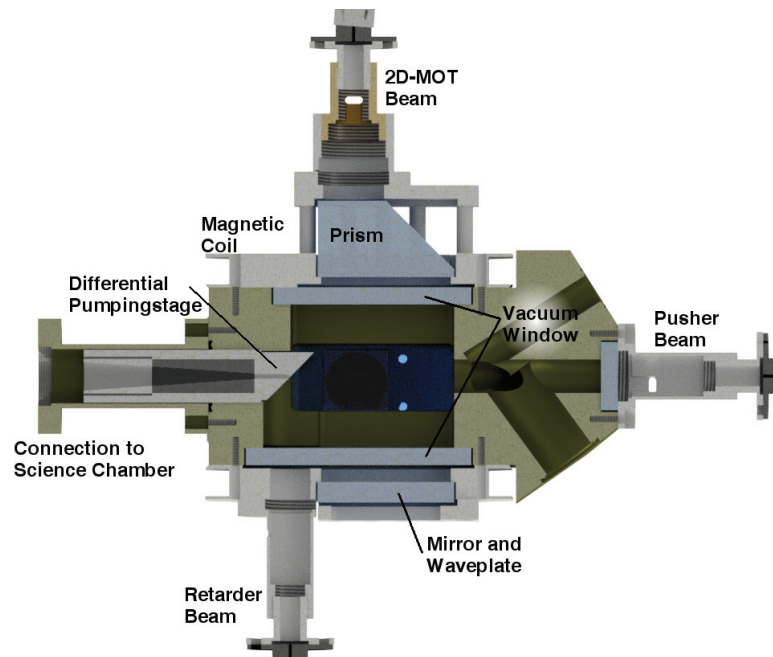


Figure 2.4

The source chamber operating in a $2D^+$ -MOT configuration. Visible is the fiber entrance at the top and a prism spreading the incoming beam out. After passing the chamber, the light is retro reflected and crosses the chamber again. While on the right-hand side the pusher enters, on the left-hand side the differential pumping stage with a small diameter hole and the reflective 45° surface are visible.

2.2.3. Science chamber

The science chamber can be described as the heart of the whole experimental setup. It is connected to the source chamber and the pumping section (see Figure 2.5), located close to the center of our drop capsule to minimize movement caused by slight rotations in free fall.

The chamber is made out of titanium, thus minimizing magnetic stray fields and is equipped with 19 windows for optical accesses. Six individual beams in combination with a magnetic coil in Maxwell configuration form a standard three dimensional magneto optical trap (3D-MOT). A camera, including imaging system and a large area photo diode are used as independent detection systems. The dipole trap beam is focused to the center of this chamber by a single lens. Two additional magnetic coils in Helmholtz configuration can be used to cancel residual magnetic fields.

2.2.4. The pumping section

The pumping section is connected to the science chamber via a CF 16 connector opposite the source chamber. An in house designed Y-piece avoids right angles in the setup, to maintain a high flux of residual gas atoms into the pumping area. Its location is chosen to collect

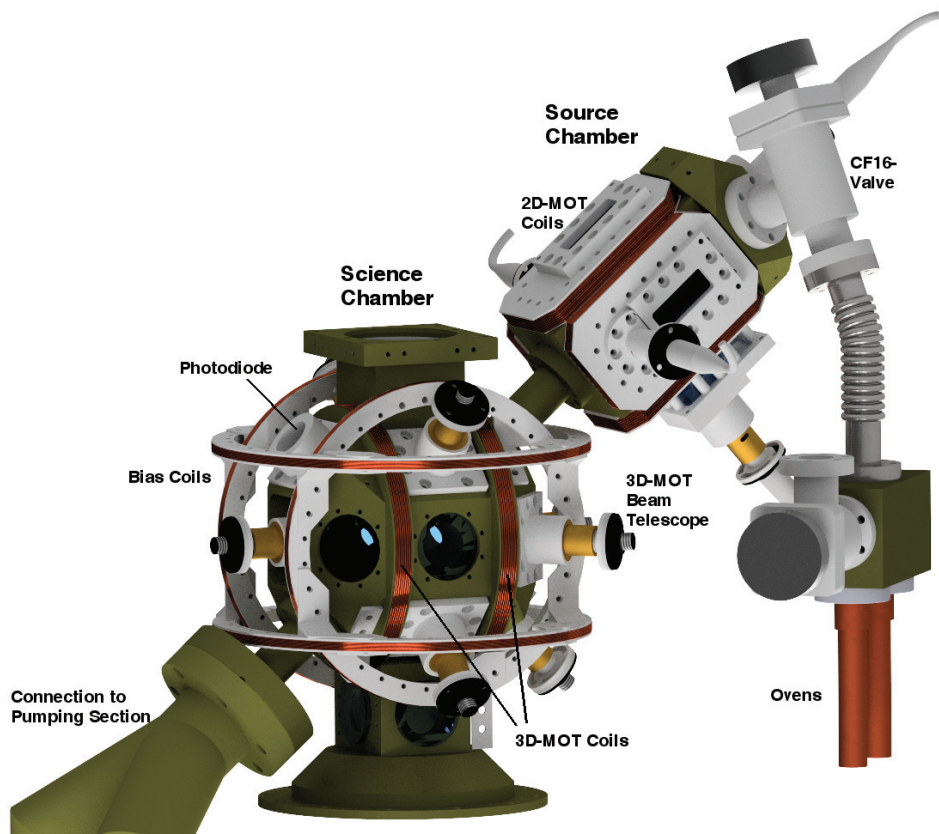


Figure 2.5
Ovens, source chamber and science chamber detailed information is given in the text.

2. Experimental Setup

the emitted atoms from the source chamber, which were not caught in the 3D-MOT while passing it. Both arms of the Y-piece lead into a vacuum pump. One side carries a Capacitorr D-200 [SAES] non evaporable getter pump (NEG) the other a Nextorr D-100-5 [SAES]. The first one contains several sintered porous disks made of St172, a combination of zirconium powder and St707 (zirconium, vanadium and iron) (SAES 2007; SAES 2017). This vacuum pump is capable of trapping $H_2, H_2O, CO, CO_2, O_2, N_2$ and hydrocarbons, with a pumping speed of 200 l/s for H_2 , while rare gases can not be absorbed. To activate and reactivate this getter material, temperatures above 450 °C are required. This is clearly more than indium seals can take, but the distance between both is large enough to avoid any melting problems.

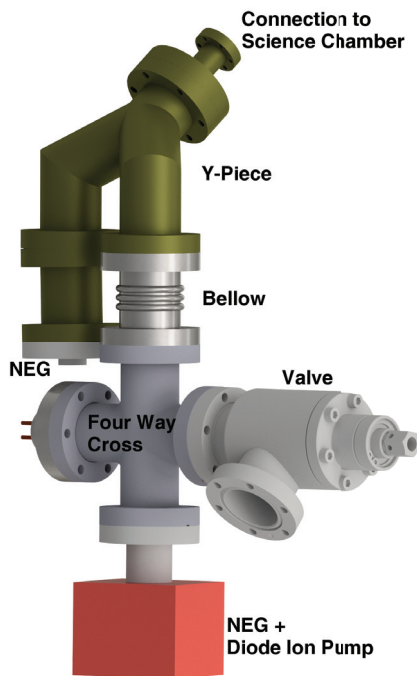


Figure 2.6
Drawing of the pumping section. The uppermost CF16 connection links the pumping section to the science chamber. Two arms are equipped with different vacuum pumps while one also carries the valve connection for a turbomolecular pump.

The Nextorr pump on the other arm of the Y-piece is a combination of an NEG and a diode ion pump. While the getter material is the same one as what is used in the Capacitorr, due to less material its pumping rate is smaller by a factor of two. The diode ion pump is capable of trapping rare gases with up to 6 l/s. Both pumping techniques complement each other to maintain the high vacuum quality required for experiments on cold atoms.

As one can see in Figure 2.6, a 4 way cross and a valve were attached to this arm as well. To uncouple the resulting impact forces from the rather small connection to the science chamber, while in drop tower operation, a bellow was implemented just before the cross. This design furthermore avoids mechanical over determination. The valve is used to connect a turbomolecular pump to pre-evacuate the system before operation. On the residual cross port an electrical feedthrough was installed, connecting an rf-antenna to drive atomic microwave transitions with the surrounding environment.

2.3. Dipole trap laser

The dipole trap laser is a thulium based fiber laser manufactured by the LZH (Laser Zentrum Hannover e.V.). The primary stage emits light at a wavelength of 1949 nm with a linewidth of 0.1 nm and is followed by a power stage. Both sections are based on Tm^{3+} -ion doped fibers, pumped by laser diodes at a wavelength of 793 nm (S. D. Jackson et al. 2007). The available laser power is restricted to a bit more than 20 W at the output port by an optical isolator, which is not suited for higher energy density levels. It features a linear polarization with an extinction factor of >15 dB. From the trapping point of view, polarization only gets important when the geometry is switched to a crossed dipole trap configuration giving rise to interference caused substructures of the trap.

In our case, the linear polarization is used to manipulate the laser's intensity, by using a Pockels cell and two Glan-Laser prisms (see Figure 2.8). The first prism further increases the incoming polarization to a extinction ratio of ≈ 50 dB. A $\lambda/2$ waveplate in front of the polarizer is used to maximize the transmitted power. While passing the Pockels cell, the polarization can be turned by applying a high voltage of up to 6.5 kV to the cell. At maximum voltage, the polarization is turned by 90° , becoming perpendicular to the incoming beam. Depending on the applied voltage, a certain fraction of light passes the second Glan-Laser prism. One technical constraint is that only the transmitted beam of a Glan-Laser prism is well polarized. With this setup the beam intensity can be modulated between 5 mW and 7 W, measured after passing the vacuum chamber.

In Figure 2.7 one can see the characteristic non linear transfer function of a Pockels cell, described by a cosine, making it difficult to get a proper active intensity stabilization. The problem has been approached before by our project partners, but the solution could not yet be adapted to our system (Matthias 2013).

The dipole trap laser has to be carefully designed to withstand the harsh drop tower environment. The main issues are decelerations of up to 40 g during impact, which are tackled with a robust mechanical design. The second problem is a lack of cooling water supply while dropping. Generating 20 W of optical power requires 300 W of electrical power in the final stage alone. In this case, the generated heat is absorbed by a phase changing material. It is assembled just beneath the power amplifying laser diodes, allowing an operation at full power for five minutes,

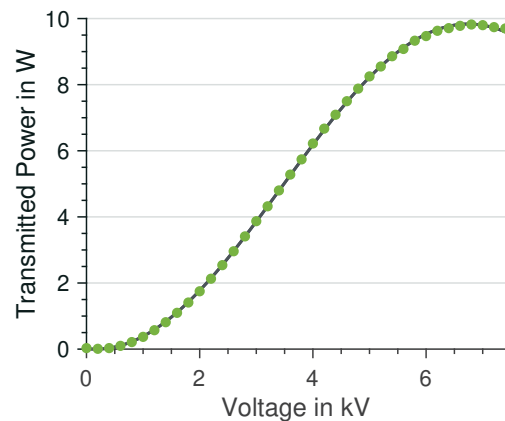


Figure 2.7
Dipole laser intensity dependence on Pockels cell voltage.

2. Experimental Setup

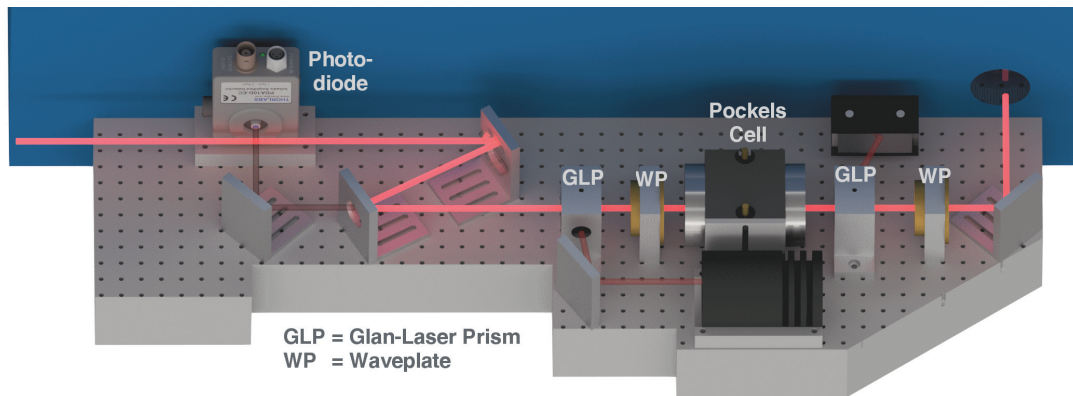


Figure 2.8

Setup to modulate the intensity of the dipole laser. The fraction of light passing the assembly is dependent on a voltage applied to the Pockels cell. Further information is given in the text.

without external cooling (Damjanic 2013). Afterwards the material has to be charged again by external water cooling.

A long term power stability of 0.1 %, mentioned in the laser's manual, is only valid after a certain warm up time. This is not the case for drop tower measurements, since the available electrical power is not sufficient to keep the laser running for the required time. Realistic power variations between drops are estimated to be around 3 %.

2.4. Electronics

Electronics in a drop tower experiment have to be light and compact, due to the limited space available. In some cases it is possible to choose commercially available off the shelf products, some tasks require specific customized solutions. This section will explain the major electronic components. The entire system is once again subdivided into three subsystems (see Figure 2.9) namely the FPGA system, the camera computer and the control room computer were the latter is only used in drop mode operation. FPGA and camera PC are controlled by a single windows PC called Lab PC.

2.4.1. FPGA system

Communication with the FPGA (Field Programmable Gate Array) is managed by Labview software based on developments of the QUANTUS collaboration (Herr 2013) with slight modifications to match our experimental needs. It splits into time-dependent and time-independent executions. The first category implies actions, for example switching lasers on and off, setting temperatures, providing trigger signals, setting up our camera configuration and locking lasers to the right frequencies, as well as receiving information about temperatures or laser powers. Time dependent variables are wrapped in a sequence assembled on the lab

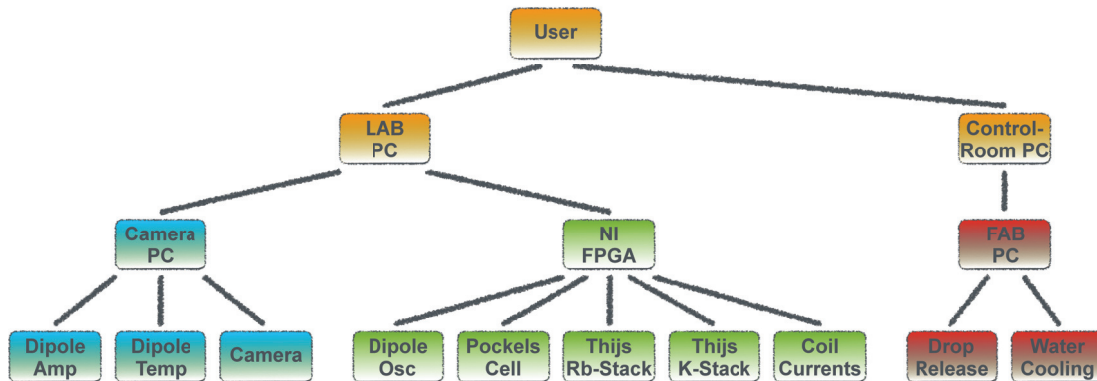


Figure 2.9
Schematic drawing of the experiments electronics. Several computers can be accessed by the user controlling different subsystems.

computer including frequency shifts, several triggers, magnetic field control and laser power levels. The FPGA stores the experimental sequence and, running with a Labview real-time environment, provides a sufficient timing for every step. In this manner, it can be understood as the heart of our experiment's electronics. Execution times are limited by an internal clock rate of 40 MHz. Time-independent tasks are looped through the FPGA and handed over to the execution devices in the lowest row in Figure 2.9.

Dipole oscillator driver: The dipole oscillator is operated with a home-made laser current driver. Its output current is manually controlled only. It is statically set to 2.8 A by a potentiometer, but can be remotely switched on via an enable TTL trigger, provided by an FPGA systems digital out.

Pockels cell driver: The pockels cell is driven by a high voltage amplifier [10HVA24, Ultravolt]. The output can be enabled by an FPGA provided digital output trigger, while the desired voltage is set by an analogue signal from the FPGA system. The incoming voltage varies between 0 and 6.5 V and is amplified by a factor of one thousand. In Figure 2.10 on can see the output voltages plotted over time. With a rise time of $26 \text{ V}/\mu\text{s}$ (Figure 2.10(a)) and the same fall time (Figure 2.10(b)), the device is suitable for experiments like ours, where a critical step is the release of cold atoms from the trap. If it takes too long, temperature measurements, relying on free expansion of the atomic cloud, will be distorted. Another important parameter is the noise spectrum, which directly translates into power noise of the dipole trapping laser, leading to heating in the trap. By replacing the HVA with a more sophisticated but not drop resistant amplifier, featuring a lower noise level, it could be demonstrated that voltage noise is not limiting our cooling or trapping performance.

Thijs Stack: The Thijs stacks, one for rubidium and one for potassium, are an assemblage of stacked in- and output cards to control mainly our laser system, but also e.g. to operate the ion

2. Experimental Setup

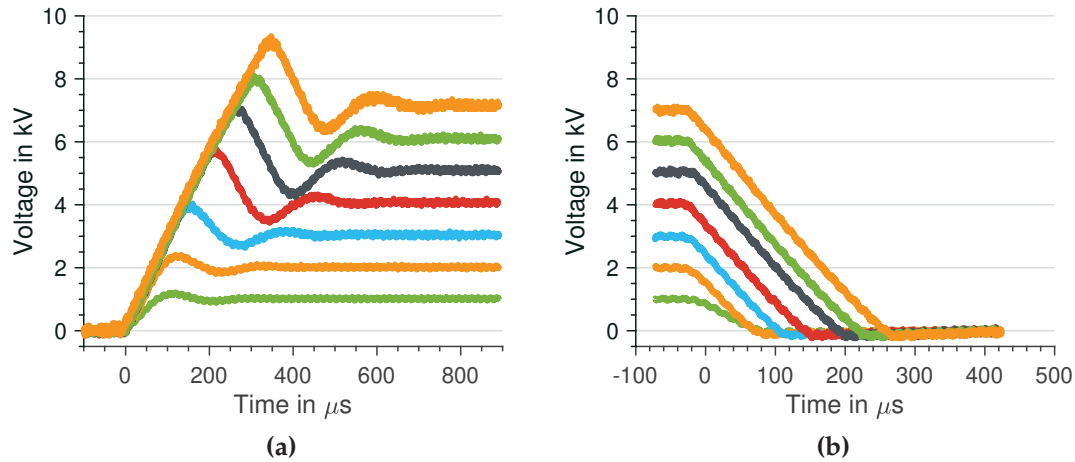


Figure 2.10

Rise (a) and fall (b) behavior of the Pockels cell high voltage driver. Both slopes were determined to be around $26 \text{ V}/\mu\text{s}$. While voltage decreases appear almost linear voltage increases feature an overshoot.

pump in drop mode. These compact electronics have been developed by Thijs Wendrich² at the IQO in Hannover and were not only used for drop tower experiments but also on a sounding rocket in space. Different $100 \text{ mm} \times 100 \text{ mm}$ cards can be stacked together, depending on the experimental demands. The only necessary building blocks are a power supply- and an FPGA connection (or USB or Ethernet) card. Communication between the Stack and the FPGA is realized by the corresponding T-Bus (see footnote) system, developed for this purpose alone. In our system, laser controller cards provide currents, to drive all the lasers, except for the dipole trapping one. A frequency card stabilizes laser frequencies by analyzing the input beat node measuring photodiodes and responding via PI controlled modulated currents on the laser controller cards' outputs. DDS (Direct Digital Synthesis) cards generate sinusoidal signals for AOMs with variable frequency and amplitude. The relatively low signal is amplified to the required power level of approximately 30 dB by external rf-amplifiers [Mini Circuits]. A shutter card operates shutters within the laser system. Temperature controller cards maintain stable laser temperatures via Peltier elements, assembled at different locations on the lasers' housings. Since their setpoint is defined by a potentiometer on the card itself, it is impossible to change it remotely. This turned out to be an essential drawback, since the setpoint changes automatically with electronics temperature. This turned out to be a problem for drop tower measurements. Thus, they were replaced by alternative commercially available temperature controllers [Meerstetter]. Results in this thesis were recorded with both setups. Apart from the laser system, a UHV card produces a high voltage supply for the ion getter pump, maintaining a good vacuum quality in drop tower operation.

²Several experiments are based on this technology but no dedicated publication is available. Information can be mainly found in PhD thesis utilizing Thijs-Stack (also T-Stack) and T-Bus (Kulas 2016; Rudolph 2016; Grzeschik 2017; Sternke 2018)

Coil Currents: The various magnetic field generating coils were operated by numerous current drivers over the years of testing. Unsuitable for our PRIMUS-project were the drivers used in the QUANTUS-collaboration and a solution based on an H bridge, most of all because of their reliability. One working solution is a simple mechanical relay connecting the coils with its battery supply. In this basic solution, the operation current is determined by hardwired load resistors of different values. This rather easy and robust solution comes with the drawback of fixed current values that of course can't be remotely controlled. To overcome this problem, compact and robust current drivers [Servowatt] were purchased, which are running on DC power and deliver up to 192 W output power. With rise times of 1 ms and fall times in the order of 0.5 ms operating on the 3D-MOT coils (see Figure 2.11) the Servowatt driver performance is sufficient. Both solutions were used for the measurements in this thesis. For the data recorded the current source played no role.

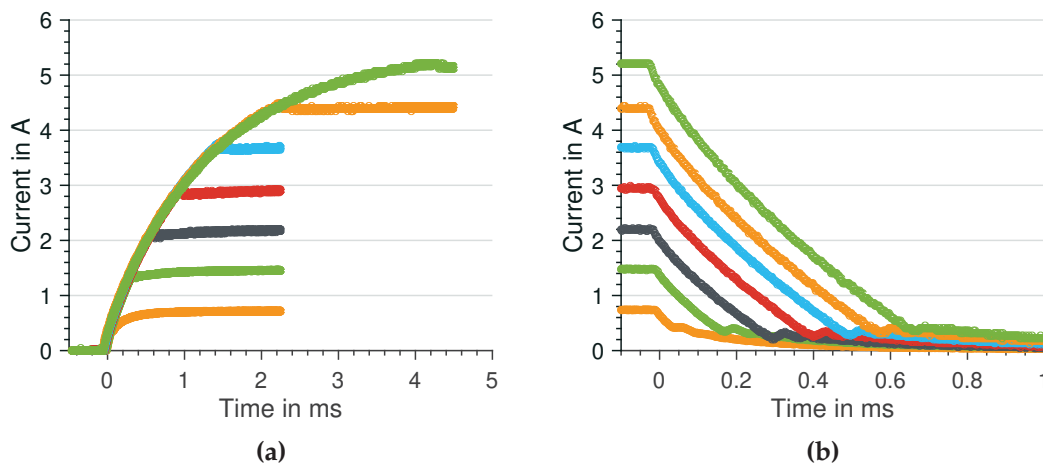


Figure 2.11

Rise (a) and fall (b) behavior of the coil current drivers purchased from Servowatt. Measurements were taken on the 3D-MOT coils operating at around 3.6 A resulting in a switch off time of approximately half a millisecond.

2.4.2. Camera computer

The camera computer is a windows based mini-PC with outer dimensions of 200 mm × 200 mm × 40 mm equipped with a solid state hard drive. It connects to the few capsule components that can not be controlled by the real time PXI system.

This includes the camera, a PCO1400, that only comes with a firewire connection and drivers incompatible with real time systems. While the captured pictures are bypassed to the LAB PC in ground operation the images are stored on the camera PC in drop mode. The existing wifi connection, in the drop tower, is not fast and reliable enough to transfer picture sized data while dropping.

2. Experimental Setup

Furthermore, the temperature controllers [LAIRD Technologies, TC-XX-PR-59] for our dipole trap laser come with windows based drivers only. The demanded RS-232 signal is provided by an USB port of the computer and translated by an external converter.

The last connected device is the dipole laser power stage current driver. The computer is used to set laser power and status readout. The final on/off switching is realized by a single TTL trigger provided by the FPGA system, since it is critical in timing. To protect the laser from malfunctions, it is always switched off before the impact in drop operation.

2.4.3. Control room computer

This computer is part of the drop tower facility and is not exclusively used by our experiment. It is connected to the capsule integrated FAB PC (Fallturm-Betriebsgesellschaft, Drop Tower Operation and Service Company) and provides the interface for cooling water supply. Colling water is only available in the waiting position in the top of the tower. The FAB-PC furthermore controls the drop release mechanism. It disconnects one second after receiving a trigger signal, generated by the FPGA system. It also collects drop related data like capsule pressure, voltages or impact forces as shown in Figure 2.12.

2.5. Operation in weightlessness

To run the experiment in a microgravity environment, the drop tower in Bremen was chosen. It is a tower with a total height of 146 m, housing a 122 m evacuable steel tube. Experiments can be released at a height of 110 m providing a free fall time of 4.7 s, after which the experimental device is captured in a container filled with polystyrene balls, 8 m of height. In our case, this leads to a deceleration of about 36 g, where g describes the Earth's gravitational acceleration (Figure 2.12(d)). A catapult mode, doubling the available free fall time, can not be used by the PRIMUS experiment because of its size.

Operating the system under weightlessness is restricted to not more than 2 drops per day and drops have to be booked typically one year in advance. For this reason measurement campaigns have to be planned well and repeated measurements for improved statistics are impossible in most cases.

The entire setup was designed for the operation in the drop tower. For this reason it features several accumulators, as it can be seen in Figure 2.1, enabling an autonomous operation during the flight. This reflects in the nomenclature of voltages in the system, referred to multiples of the installed lithium iron phosphate battery cells. The working voltage of a single cell lies in between 3.3 V and 3 V so a voltage of 2C refers to a voltage of $\approx 6.4 \text{ V}^3$. The battery platform delivers seven different voltages: 1C, 2C, 4C, 6C, -2C, -4C and -6C.

The whole procedure starts by checking the systems' performance on ground, followed by the

³The indication of a C-value for batteries normally describes its maximum output current. Following this notation, the C here has to be replaced by an S.

capsule handover to the drop tower facility employees. It takes about 30 minutes to encapsulate the device with a hermetically sealing hull, transport it into the tower and lift it up to the release position. Due to limited available energy, the lasers are switched off during this period. After establishing a proper data communication, the drop tube is evacuated for almost two hours. Sufficient local thermal equilibrium on the laser board is ensured by turning the lasers on, one and a half hours before the dropping. This procedure provides stable laser powers and polarization.

The power consuming dipole trap is activated only 10 minutes prior to the drop, leading to a strong power instability in the range of 3%. A pre-programmed sequence is uploaded to the FPGA and determines the experimental steps within the drop itself. After the impact, most parts of the system are switched off and it takes another half an hour to refill the vacuum tube with air. The experiment is recovered by the drop tower employees and handed over to the scientists within another 20 minutes. After the accumulators have been recharged and the system is checked for damages the procedure starts over again.

In Figure 2.12 experimental data from the whole drop procedure can be seen. In (a) the accumulator voltages over the whole procedure of evacuation, dropping and recovery are plotted. Three characteristic curves are shown. The 2C voltage decreases over time and sudden drops can be seen when lasers are switched on. The expected plateau with more or less constant voltage follows a fast initial drop. Switching lasers off lifts the voltage again. The 4C voltage is buffered during the evacuation period, as is the 6C voltage, not shown here. One can see it decreasing for 10 min, until the capsule is connected to the supply voltages at its waiting position at the top of the tower. Over the time of evacuation, it stays constant and drops just before the capsules release, after it has been disconnected. The -4C voltage curve is representative for all negative voltages. They do not feed any power consuming devices making them uncritical for experimental sequences.

Figure 2.12(b) shows three temperature curves and the pressure inside our capsule. The temperatures of laser board (orange line) and electronics platform (green line) are recorded with a single thermistor each. Thus, these are local values. Both curves rise, while the experiment is prepared and transferred to its waiting position. After 10 min of data recording, the cooling water supply is activated and both curves decrease until the lasers are switched on. The sudden increase is an measurement artifact, caused by an electrical ground shift. Towards the end of the evacuation time, when the system operates at full power, the laser system gets warmer, despite the cooling water. This was not found to be a problem.

The temperature evolution inside the FAB computer is immune to the environmental influence and rises constantly throughout the entire sequence.

The capsule pressure has no effect on any component but as the system is hermetically sealed, it acts as a global temperature signal. It confirms the increased temperature towards the end of the evacuation time.

The Capsule is equipped with different accelerometers. The measurements from a small range,

2. Experimental Setup

three axis, device are plotted in Figure 2.12(c). The microgravity time of 4.7 s becomes visible. Figure 2.12(d) shows the information from a larger range, single axis device, which records a deceleration of approximately 36 g, constantly for all executed droppings.

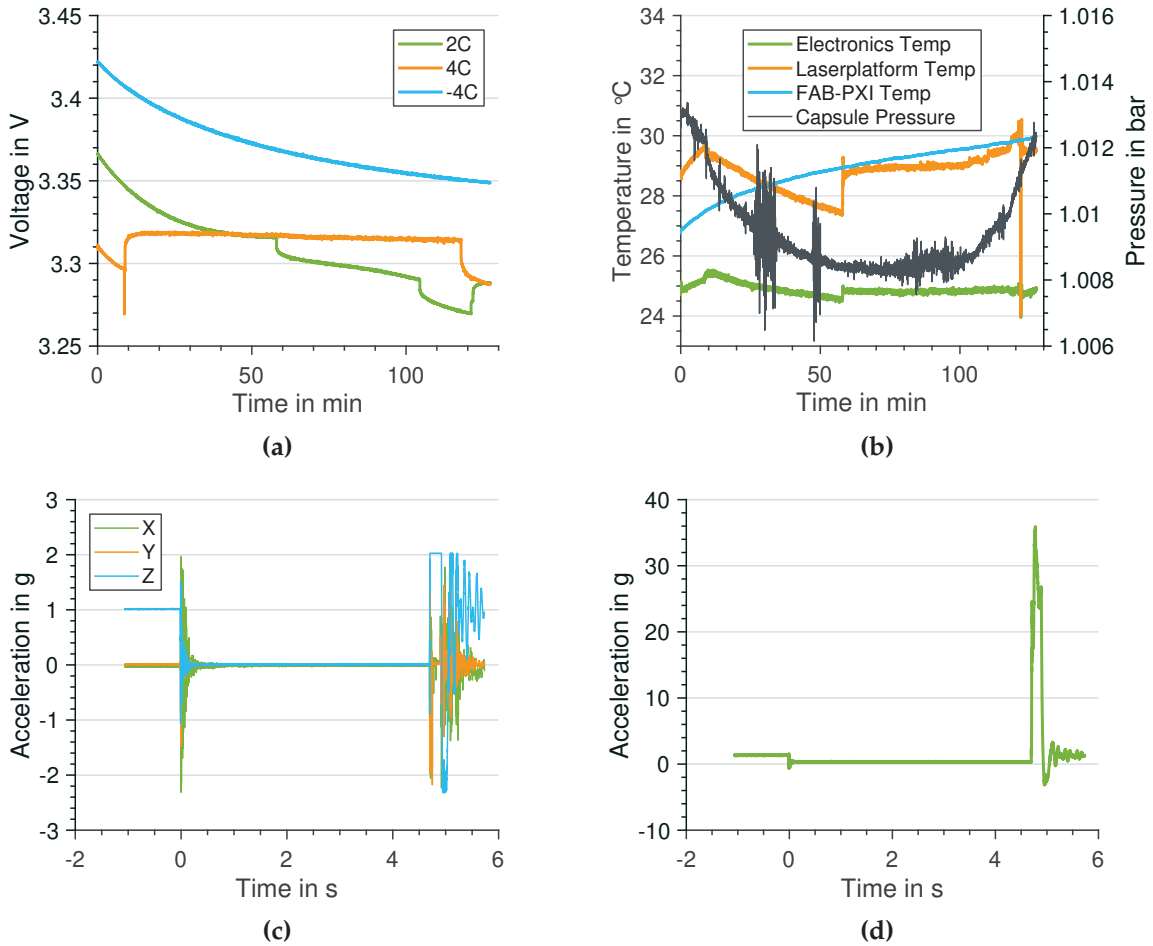


Figure 2.12

Experimental capsule data from a drop sequence. In (a) one can see the accumulators voltages over time for better visibility the values are divided by its respective number of accumulator cells. (b) shows temperature and pressure data, (c) displays the forces acting on the capsule around and during the drop on a small scale while (d) shows the forces on a larger scale with a focus on the impact force. Further information can be found in the text.

3. Dipole Trap Loading

Optical trapping potentials for atoms, molecules or larger objects are generally considered as *optical tweezers*. First applied to trap latex spheres in the year 1970 (A. Ashkin 1970)¹, they became a tool with broad applications mainly in physics and biology. Biologists can trap and manipulate e.g. viruses (A. Ashkin and Dziedzic 1987), bacteria (Diekmann et al. 2016) and living cells (H. Zhang et al. 2008)². Physicists apply optical tweezers to nanoparticles (Dienerowitz et al. 2008; Hebestreit et al. 2018), ions (Schneider et al. 2010; Schaez 2017) and atoms.

Three different forces are important in the context of optical tweezers. The first one is a force along the beam direction, originating from momentum transfer from photons to the object, upon absorption or reflection, called radiation pressure. Apart from molasses-like configurations (Dalibard 1988) it is not used for trapping. Due to our choice of a wavelength far detuned from resonance, less than one photon per second is scattered (Ivanov 2007) making radiation pressure negligible for this thesis.

The second force is called gradient radiation pressure and acts on transparent objects that are large compared to the trapping wavelength. The mechanism is based on refraction of the beam while penetrating the object's surface (A. Ashkin 1970; Shaevitz 2006). It attracts particles along an intensity gradient, for Gaussian beams toward the center, perpendicular to the beams propagation direction. In axial direction the force pulls towards the beam waist. Since the trapped atoms in this thesis are small, compared to the trapping wavelength, gradient radiation pressure forces do not appear in the described experimental setup.

The third one is a gradient force as well. It acts on objects much smaller than the trapping wavelength and is based on induced dipole moments giving it the name (*optical*) *dipole force*. Respectively the formed trap is referred to as (*optical*) *dipole trap*, a sub-category to general optical tweezers, first realized for atoms in the year 1986 (Steven Chu, Bjorkholm, et al. 1986). Based on the AC-Stark effect, internal atomic energy levels are shifted, resulting in attractive or repulsive forces towards areas with high laser intensities. These traps typically have trap depths in the order of a few 100 μK making it impossible to catch atoms at room temperature. For this reason other cooling steps have to precool the atoms before they can be loaded into the dipole potential.

¹For his work on optical tweezer Ashkin was awarded with the Nobel prize for physics this year.

²Reference (Lang et al. 2003) is a sorted collection of papers for biologically motivated literature, while a review article can be found in (Svoboda et al. 1994)

3. Dipole Trap Loading

This chapter describes the precooling techniques necessary to load atoms into the dipole trap, contains a more detailed explanation for the dipole potential and sheds light on the loading process itself.

3.1. The Magneto-Optical Trap

Magneto-optical traps (MOTs) (Raab et al. 1987) are used to cool atoms from room temperature to a few hundred μK . Because they are well described in literature (Metcalf et al. 1999) this will only be a brief summary of the main features with an emphasis on the interplay between MOT and dipole trap, which is strongly influenced by the utilized trapping laser frequency.

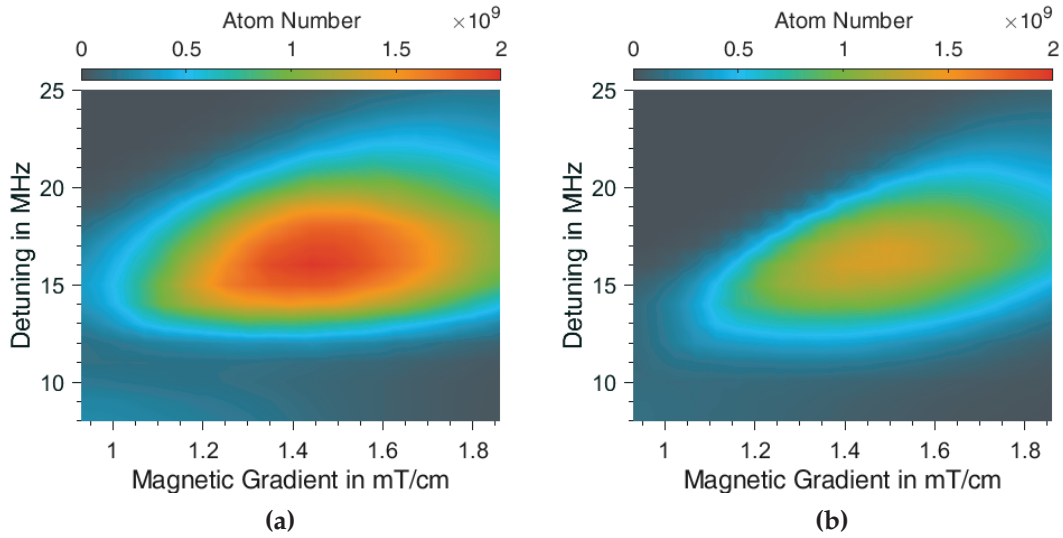
In a MOT, atoms are slowed down via photon momentum transfer. For a cooling mechanism it is mandatory to only absorb photons from the direction opposite to the atom's movement in order for them to be slowed down. This is guaranteed by a cooling laser frequency detuned to the red, so with less energy, with respect to an atomic transition. The atom's velocity causes a Doppler shift bringing the atomic resonance closer to the photon energy.

Illuminating atoms with six laser beams, a counter propagating pair in each spatial dimension, results in a velocity dependent deceleration force. An additional force with spatial dependence is provided by an external magnetic quadrupole field which removes the degeneracy between different magnetic sublevels. In combination with circularly polarized MOT beams this gives rise to a spatially dependent probability to absorb photons.

Rubidium-87 is cooled using the $5^2S_{1/2} (F=2) \rightarrow 5^2P_{3/2} (F'=3)$ transition (D₂ line) coming with a loss channel into the $5^2S_{1/2} (F=1)$ state. For this reason, in addition to the cooling laser light, a second laser frequency is applied to bring atoms back into the cooling transition. The second laser, as mentioned in 2.1, is called repump laser. It is not detuned with respect to the atomic transition and therefore needs a lot less power than the cooling one.

According to this, the critical parameters to run or optimize a MOT's performance are both laser powers, their ratio, the cooling light's detuning and the magnetic field strength. In Figure 3.1a) one can see the number of atoms caught in the trap with respect to the cooling laser detuning and the current, driving the magnetic field. Optimal performance is observed with a detuning of 16 MHz (2.6 times the natural line width) and a current of 3.1 A, equal to a magnetic field gradient of $1.4 \frac{\text{mT}}{\text{cm}}$.

The available cooling laser intensity is limited to a few mW per beam. In this range no saturation effects could be observed and more power leads to more atoms in the trap with an almost linear dependency. Because one laser feeds both MOTs, the two dimensional and the three dimensional, the power ratio has to be chosen carefully. Best results were observed with the values in Table 3.1 while the performance is insensitive to variations in repumping laser power.

**Figure 3.1**

Atom number optimization in the 3D-MOT with respect to the magnetic field gradient and cooling laser detuning. *a)* Measurement with maximum cooling laser intensity, *b)* Measurement with decreased cooling laser power.

	2D-MOT	3D-MOT
Cooling laser	2x 20 mW	6x 7 mW
Repumping laser	2x 1 mW	6x 0.5 mW

Table 3.1

Chosen laser powers in 2D- and 3D-MOT.

Operating the apparatus in microgravity in some cases led to a reduction of the available laser power, due to altered thermal conditions. While hanging in the drop tower's vacuum tube for one and a half hours, thermally induced mechanical stress, on the holders for optical components, degraded the laser platform's performance, despite the activities to counteract this problem described in Chapter 2.

Since magneto-optical trapping is based on the atom's scattering rate, which depends on laser power and detuning, the consequences of a reduced laser power on the MOT performance were investigated and plotted in Figure 3.1b). The observed reduction in atom number, in this particular case 25%, does not lead to fewer loaded atoms in the dipole trap. An optimal loading performance is achieved, by almost the same detuning and magnetic gradient parameters, independent of laser power. For this reason no adjustments between drop tower and laboratory operation have to be made. For potassium we observed a stronger dependency. Thus in this case, the cooling laser detuning and the magnetic gradient must carefully be matched to the available laser power (Blanke 2016).

3. Dipole Trap Loading

Operating the system in optimal condition leads to $\approx 1.8 \times 10^9$ atoms loaded in 3 s. The corresponding loading curve is plotted in Figure 3.2. To smooth out the high scatter in the fluorescence measurement, the data points were fitted to

$$N_{MOT}(t) = \frac{R_{0MOT}}{\alpha} \left(1 - e^{(-\alpha t)}\right). \quad (3.1)$$

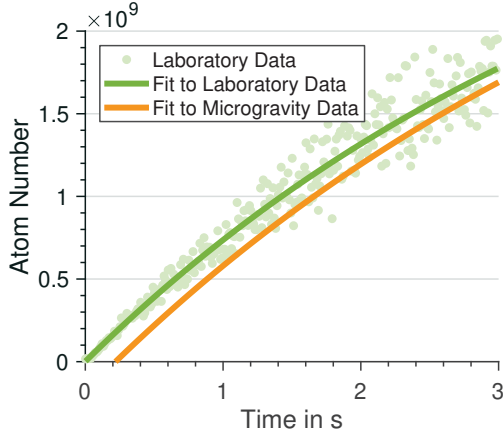


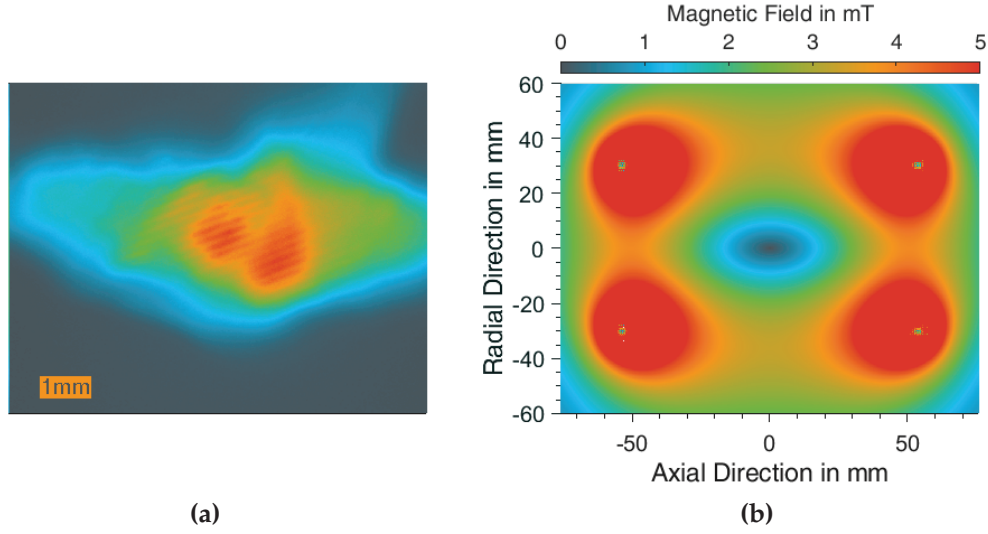
Figure 3.2
The MOT's loading curve. Approximately 1.8×10^9 atoms can be loaded within 3 s. Green points are fluorescent detection data while the green line is the corresponding fit to Equation (3.1). The orange line represents a loading data collected in microgravity, the underlying data points are not shown and the curve is shifted by 200 ms for better visibility.

Here $N_{MOT}(t)$ is the number of atoms which are loaded into the MOT, R_{0MOT} is the initial trap loading rate, α describes losses caused by collisions with residual background gas atoms and t is the loading time. The initial loading rate is determined to be $R_{0MOT} = 8.32 \times 10^8 \frac{\text{atoms}}{\text{s}}$ for operation with and without gravity. The corresponding loss rates are $\alpha = 0.24$ and $\alpha = 0.21$ respectively. This means, the slight observable difference in the loading performances in Figure 3.2, is caused by vacuum quality differences. These are related to changes over month. Therefore gravity has no influence on the loading behavior of the MOT.

A false color image of a fully loaded MOT can be seen in Figure 3.3 (a). Two main features should be pointed out in this picture, namely a slight fringe pattern in the trap center and the elongated shape. While the fringe patterns most likely are caused by an imperfect

beam alignment as described by Steane *et al.* (Steane et al. 1992), the elongated shape represents the underlying magnetic field, as it is visible in Figure 3.3(b). Here the magnitude of the magnetic field is simulated in arbitrary units. Four red areas surround the coil intersection with the illustrated plane, indicated by smaller areas with less magnetic field. Intersection points in radial direction belong to the same coil. The angle of view in Figure 3.3(a) and (b) is shifted by 45° to each other still indicating the difference in gradients along different directions.

To summarize the MOT performance results, one can say that it works very well as a source for cold atoms. The amount of atoms and loading rate are appropriate for further cooling steps and set a reliable foundation for dipole trap loading. In microgravity and on ground, identical performances could be demonstrated.

**Figure 3.3**

(a) A fluorescence image in false colors of a fully loaded MOT with approximately 10^9 atoms. Notice a radial anisotropy for the atomic density and fringe patterns in the center caused by imperfect beam alignment (Steane et al. 1992). (b) A simulation of the magnetic field magnitude for the given setup. The magneto-optical trap is placed right in the center of this picture and clearly explains its anisotropy. Further information is given in the text.

3.2. The Optical Dipole Potential

The theory of dipole traps is well described in (Grimm et al. 1999) and the following paragraph is based on their work.

In a classical picture, an atom, consisting of a nucleus and an electron, is polarizable by an external field and can be described as an harmonic oscillator. An oscillating external field $E(r, t) = \hat{e}\tilde{E}(r)\exp(-i\omega_L t) + c.c.$, such as a laser field, induces an oscillating polarization of the atom described as $p(r, t) = \hat{e}\tilde{p}(r)\exp(-i\omega_L t) + c.c$ with the unit polarization vector \hat{e} , the driving frequency ω_L and the amplitude of the dipole moment \tilde{p} . The amplitude of the electric field and its counterpart in the polarization are linked with the complex polarizability $\alpha_p(\omega_L)$ as

$$\tilde{p} = \alpha_p(\omega_L)\tilde{E}. \quad (3.2)$$

Taking the temporal average of the interaction energy leads to the dipole potential

$$U_{Dip} = -\frac{1}{2}\langle pE \rangle = \frac{1}{2\epsilon_0 c} \text{Re}\{\alpha_p\}I(r), \quad I(r) = \frac{1}{2}\epsilon_0 c |\tilde{E}(r)|^2 \quad (3.3)$$

with ϵ_0 the vacuum permittivity, c the speed of light, and I , the driving field's intensity. The angled brackets denote the temporal average over several oscillations, while the factor of one half accounts for an induced rather than a static dipole moment. The gradient of Equation (3.3) is the dipole force mentioned above. It is caused by dispersive interaction of the induced dipole

3. Dipole Trap Loading

moment with the gradient of the driving field. For this reason, only the real part of the complex polarizability is included in the calculation. The imaginary part, however, describes power absorption from the electric field and can be written in a similar manner

$$P_{Abs} = \langle \dot{p}E \rangle = \frac{\omega_L}{\epsilon_0 c} \text{Im}\{\alpha_p\} I(r). \quad (3.4)$$

In a quantum mechanical picture, this absorption is based on scattering events. To get a useful equation for the associated scattering rate Γ_{sc} one replaces the driving field energy with a stream of photons that can be absorbed and reemitted by the atom

$$\Gamma_{sc}(r) = \frac{P_{Abs}}{\hbar\omega_L} = \frac{1}{\hbar\epsilon_0 c} \text{Im}\{\alpha_p\} I(r). \quad (3.5)$$

Obviously, the complex polarizability of the atom under investigation plays a major role in trapping and scattering, as explained above. It is once again approached in a classical picture, the Lorentz model (Lorentz 1906; Kopitzki 1993).

The picture of a nucleus and one electron is still valid. In the Lorentz picture, both bodies are connected with a spring and the electron moves in one direction (x) only. The corresponding eigenfrequency ω_{Res} to this oscillator represents the optical transition in a two level atom. Radiated energy is described by Larmor's formula for an accelerated charge (Larmor 1897; J. D. Jackson 1999). Integrating the equation of motion

$$\ddot{x} + \Gamma_{\omega_L} \dot{x} + \omega_{Res}^2 x = -\frac{e}{m_e} E(t) \quad (3.6)$$

leads to the desired expression for the complex polarizability

$$\alpha_p(\omega_L) = \frac{e^2}{m_e} \frac{1}{\omega_{Res}^2 - \omega_L^2 - i\omega_L \Gamma_{\omega_L}}, \text{ with } \Gamma_{\omega_L} = \frac{e^2 \omega_L^2}{6\pi\epsilon_0 m_e c^3} \quad (3.7)$$

where Γ_{ω_L} is the classical damping rate for radiative energy loss. By introducing the on-resonance damping rate $\Gamma = (\omega_{Res}/\omega_L)^2 \Gamma_{\omega_L}$, this formula can be altered to

$$\alpha_p(\omega_L) = 6\pi\epsilon_0 c^3 \frac{\Gamma/\omega_{Res}^2}{\omega_{Res}^2 - \omega_L^2 - i(\omega_L^3/\omega_{Res}^2)\Gamma} \quad (3.8)$$

giving reasonable results for weak driving fields, as it is the case in most dipole traps, especially far-off-resonance traps, like the one used in this experiment. For strong driving fields, saturation would become relevant that have to be treated with quantum theory.

Inserting Equation (3.8) into Equation (3.3) and (3.5) results in

$$U_{Dip}(r) = -\frac{3\pi c^3}{2\omega_{Res}^3} \left(\frac{\Gamma}{\omega_{Res} - \omega_L} + \frac{\Gamma}{\omega_{Res} + \omega_L} \right) I(r) \quad (3.9)$$

and

$$\Gamma_{sc}(r) = -\frac{3\pi c^3}{2\omega_{Res}^3} \left(\frac{\omega_L}{\omega_{Res}} \right)^3 \left(\frac{\Gamma}{\omega_{Res} - \omega_L} + \frac{\Gamma}{\omega_{Res} + \omega_L} \right)^2 I(r). \quad (3.10)$$

Applying the rotating wave approximation (Metcalf et al. 1999), valid for detunings $\Delta \equiv \omega_L - \omega_{Res}$ much smaller than the resonance frequency ($|\Delta| \ll \omega_{Res}$), and setting $\omega_L/\omega_{Res} \approx 1$ gives

$$U_{Dip}(r) = \frac{3\pi c^3}{2\omega_{Res}^3} \frac{\Gamma}{\Delta} I(r) \quad (3.11)$$

and

$$\Gamma_{sc}(r) = \frac{3\pi c^3}{2\hbar\omega_{Res}^3} \left(\frac{\Gamma}{\Delta} \right)^2 I(r). \quad (3.12)$$

These equations reveal two important general properties of dipole traps. First, the sign of the detuning Δ defines whether the dipole force (∇U_{Dip}) is attractive or repellent (see Equation (3.11)). Working with red detuned light, i.e. with less energy than the atomic resonance ($\Delta < 0$), the potential becomes negative and atoms are attracted to areas with high intensity. Using blue detuned light ($\Delta > 0$) results in a positive potential, repelling atoms from areas with high intensities. Both techniques were used in the past (Davidson et al. 1995; Grimm et al. 1999) but the red detuned traps (Steven Chu, Bjorkholm, et al. 1986) are a lot more common, mainly because of their simpler application. This thesis will only use red detuned dipole traps.

The second important property regards the ratio between scattering rate and dipole potential depth. Since the scattering of photons increases the energy of the trapped atomic ensemble, this is a counteracting effect to the goal of cooling atoms. While the potential scales linearly with Γ/Δ the scattering rate scales with its square. For this reason far-off-resonance traps (FORTs) were designed to create equally deep traps with less optically induced heat. Of course a larger detuning demands higher laser powers to keep the potential depth at a comparable value.

Furthermore, the intensity distribution in these formulas is important for optical traps. The most simple way to realize a dipole trap is a single focused Gaussian beam. This trap geometry will be used in all the dipole trap loading experiments in this chapter.

Gaussian beams are solutions to the paraxial wave equation, originating from the Helmholtz equation (Milonni et al. 2010). They are a good representation for real laser beams and their intensity distribution reads

$$I(x, y, z) = \frac{2P}{\pi w_0} \left(\frac{w_0}{w(z)} \right)^2 e^{-2\frac{x^2+y^2}{w(z)^2}}. \quad (3.13)$$

While x , y and z are Cartesian coordinates and the beam propagates in z direction. P represents the laser power. w_0 is called beam waist and describes the beam radius at the point with the smallest beam diameter. $w(z)$ describes the beam radius in dependence of the axial coordinate z and is related to w_0 as

3. Dipole Trap Loading

$$w(z) = w_0 \sqrt{1 + \left(\frac{z}{z_r}\right)^2} \quad (3.14)$$

where z_r is called the Rayleigh length, the axial distance from the waist to the position where the beam expanded to $\sqrt{2}w_0$. $w(z)$ is defined by the area where the beam intensity dropped to $1/e^2$ of its value on the z axis. This is possible, since every cut in the x - y plane gives a Gaussian beam profile. Further relations for the Rayleigh length and beam waist can be found:

$$z_r = \frac{\pi w_0^2}{\lambda} \quad \text{and} \quad w_0 = \frac{\lambda f}{\pi \omega(z_L)} \quad (3.15)$$

with the wavelength λ , focal length f of the focusing lens and the beam radius $\omega(z_L)$ at the position of the lens z_L . Thus, for a fixed wavelength λ the beam waist w_0 is determined by f and $\omega(z_L)$. Referring to the dipole trap loading, the area enclosed by the laser beam is of great importance.

Experimentally, the waist of a Gaussian beam can be measured by the knife edge method (Suzaki et al. 1975), where a sharp edge is slowly translated through the beam, perpendicular to its propagation direction, while the transmitted power $P(x_{\text{knife}})$ is recorded. Blocking the laser beam slowly results in a dataset as shown in Figure 3.4 (green dots). Fitting these data to

$$P(x_{\text{knife}}) = \frac{P_0}{2} \left[1 - \operatorname{erf} \left(\frac{\sqrt{2}(x_{\text{knife}} - x_0)}{w(z)} \right) \right] \quad (3.16)$$

is a precise and easy way to determine the beam radius. The evolution of a beam's width is investigated by repeated measurements along several positions of the beam. Executing knife edge measurements on the actual apparatus is limited by the compact experimental setup. Thus, measurements were done at three positions along the beam path between laser and vacuum chamber. The results can be seen as dots in Figure 3.5.

The beam diameter can also be calculated by applying ray transfer matrix analysis (Brooker 2007). Here, a complex beam parameter $\frac{1}{q} = \frac{1}{R} - \frac{i\lambda}{\pi n w(z)^2}$, where n is the refractive index and R is the radius of curvature, is evolved over distance by applying transfer matrices for all optical elements and free space the beam passes.

In Figure 3.5 this calculation is done for the experimental setup. According to private

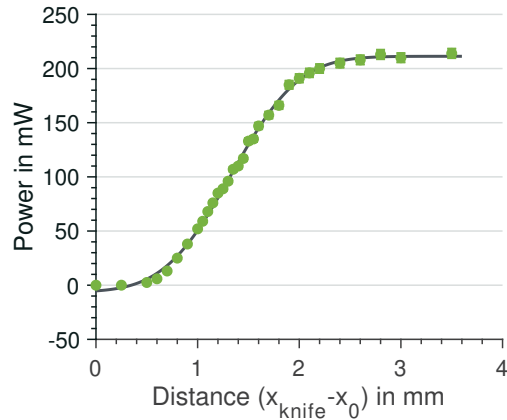


Figure 3.4
Exemplary knife edge measurement to determine the width of the dipole laser beam.

communication with the manufacturer, the single collimating lens inside the dipole laser has a focal length of 3 mm. Although great care has been taken in positioning this lens, an optimal collimation can not be realized. The measured gray dots in Figure 3.5 deviate strongly from the green line which represents the case of optimized collimation. A more realistic behavior is described by the simulated orange line. Even though it cannot be measured directly, a focus between laser and vacuum chamber is likely. Figure 3.5(b) is a magnified view of the beam diameter close to the beam waist in the center of the vacuum chamber. According to this calculation atoms will be loaded into a dipole trap with a beam waist in the range of 30-40 μm .

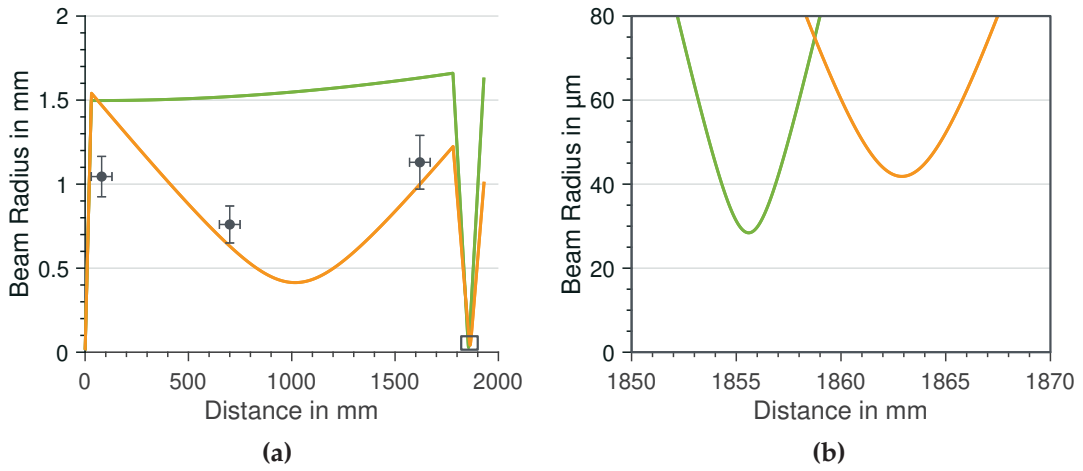


Figure 3.5

Dipole laser beam radius evolution on the path towards the dipole trap. Lines correspond to simulations based on the ray transfer matrix method, dots are knife edge measurements. The green line represents the case of a perfectly collimated beam, the orange curve is a fit to the measured datapoints. (a) Complete single beam path from the emitting laser fiber facet to the vacuum chambers back end. (b) A magnified view of the beam waist inside the vacuum chamber.

With all of these information it is possible to calculate the expected dipole potential. Inserting Equation (3.13) into (3.3) and introducing $r = \sqrt{x^2 + y^2}$ leads to the expression

$$U_{Dip}(r, z) = U_0 \left(\frac{w_0}{w(z)} \right)^2 e^{-2\frac{r^2}{w(z)^2}}, \quad \text{with} \quad U_0 = -\frac{\text{Re}\{\alpha_p(\omega_L)\}P}{\epsilon_0 \pi c w_0^2}. \quad (3.17)$$

We assume all atoms to be close to the trap center, a valid assumption based on evaporation dynamics in traps with interacting atoms that are constantly following a Boltzmann distribution (see: Chapter 4). In this case, the radial distribution is small compared to the beam waist while the axial one is small compared to the Rayleigh length. A second order Taylor series expansion of U_{Dip} around the center of the trap leads to the expression of a harmonic oscillator (Grimm et al. 1999)

3. Dipole Trap Loading

$$U_{Dip}(r, z) \approx U_0 \left[1 - 2 \left(\frac{r}{w_0} \right)^2 - \left(\frac{z}{z_r} \right)^2 \right] = -U_0 + \frac{1}{2} m \omega_r^2 r^2 + \frac{1}{2} m \omega_z^2 z^2 \quad (3.18)$$

with two different trap frequencies in the radial and axial direction

$$\omega_r = \sqrt{\frac{4U_0}{m w_0^2}} \quad \text{and} \quad \omega_z = \sqrt{\frac{2U_0}{m z_r^2}}. \quad (3.19)$$

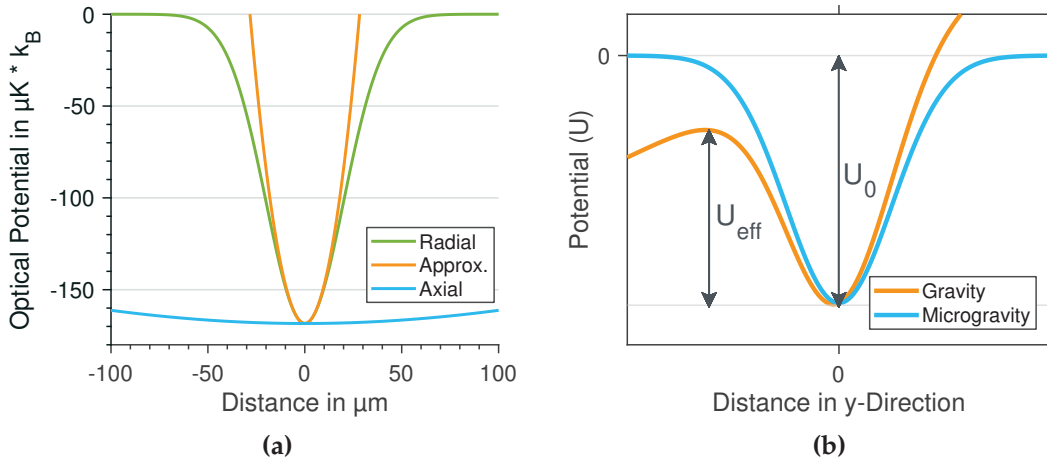


Figure 3.6

Calculated potential for a single beam dipole trap with a beam waist of $40 \mu\text{m}$. (a) The calculated potential in radial direction according to Equation (3.17) (green), compared to the harmonic approximation described by Equation (3.18) (orange) for a trapping power of 5 W. In the center of the trap, where the atoms are located, they agree well. The blue line is the calculated potential in axial direction for comparison. Atoms are obviously less confined in this direction. (b) A comparison of the optical potential with and without the effect of gravity. Gravitation contributes to the total potential with a constant gradient which leads to an effectively lowered trap depth U_{eff} .

As a simplification, these are often summarized in the mean trap frequency

$$\bar{\omega} = (\omega_x \omega_y \omega_z)^{(1/3)} = (\omega_r^2 \omega_z)^{(1/3)}, \quad (3.20)$$

the geometric mean in all spatial directions. Since most optical and magnetic traps are generally considered harmonic near their center, the trap frequency sufficiently characterizes a given potential. Classically it describes at which frequency atoms oscillates in the trap, which determines, for example, the number of collisions in a certain time period.

If temperature and atom number are know, trap frequencies can be used to calculated the atomic peak density in a trap with

$$n_0 = N \bar{\omega}^3 \left(\frac{m}{2\pi k_B T} \right)^{3/2}, \quad (3.21)$$

a formula valid for MOTs, magnetic and optical traps.

For comparison, the dipole potential is plotted in Figure 3.6(a) in dependence of its radius. The harmonic approximation (orange line) is in good agreement with the realistic potential (green line) near the trap center. The harmonic approximation in axial direction is displayed as well (blue line), to give an idea of the reduced confinement along the single beam trap.

While operating a dipole trap on ground, gravity alters its potential by adding a constant gradient. In most cases, the axial direction is oriented perpendicular to gravity, resulting in an expression for the entire potential

$$U_{Dip}(r, z) = U_0 \left(\frac{w_0}{w(z)} \right)^2 e^{-2\frac{r^2}{w(z)^2}} + mgy. \quad (3.22)$$

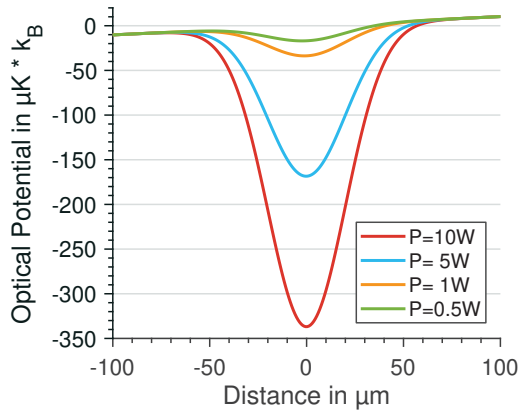


Figure 3.7
Dipole trap potentials for different laser powers in radial direction including gravity, the relative contribution of which rises with lower trapping powers.

Writing the trapping potential in y -direction as $U_{Dip}(y) = \frac{1}{2}m\omega_r^2 y^2 + mgy$ and searching for its minimum results in the formula (Ospelkaus-Schwarzer 2006)

$$y_{sag} = -\frac{g}{\omega_r^2} \quad (3.23)$$

for the gravitational sag.

3.3. Dipole Trap Loading Schemes

This section will focus on efficient loading strategies for optical dipole traps. Basically this depends on temperature and density of the initial atomic cloud. Dipole traps, which typically

Gravity has two effects on the optical trapping potential, a lowered effective trap depth and a shift of the trap center.

As depicted in Figure 3.6(b), the potential along gravity is effectively lowered and atoms can escape in this direction with less kinetic energy than they would need for any other direction. For this reason, in addition the definition of the trap depth U_0 , an effective trap depth U_{eff} is defined. The importance of a distinction between both values depends mainly on the trap depth, as it can be seen in Figure 3.7.

The second effect, a trap center displacement called gravitational sag (S. Will 2012), can easily be described in terms of trap frequen-

3. Dipole Trap Loading

have trap depths in the order of a few $100\ \mu\text{K}$ are not capable of trapping atoms at room temperature. For this reason some kind of pre-cooling must be done prior to the loading itself. Dipole potentials are conservative. An atom passing the trap can not be trapped by the potential itself, because it is accelerated towards the center of the trap as much as it is decelerated by leaving it. Therefore, trapped atoms were either situated inside the trap volume before the trap is switched on, with sufficiently low kinetic energy, or they lost energy by collisions with other atoms, or photon scattering, while passing the trap.

This section will introduce theoretical approaches to determine efficiencies for the most common dipole trap loading scenarios. From a theoretical point of view, all the introduced techniques have in common that they can to be considered as: *loading from an atomic reservoir*. An important difference in the description is whether the reservoir is in equilibrium, as in a magnetic trap, or out of it like in a molasses.

Furthermore, experimental results for the most promising strategies are presented. Choosing the ideal technique for the PRIMUS project to achieve high loading rates is constrained by the need for a certain simplicity in the experimental setup, to provide reliable results in the extreme conditions of the drop tower.

3.3.1. Loading from a Magnetic Trap

Loading from a magnetic trap allows for a relatively easy theoretical description since the atomic reservoir is in equilibrium and photon interaction is not present. For this case, three important trap loading parameters were identified (Comparat et al. 2006), namely the post-collision probability for an atom to be in a state which is kinetically low enough to be captured, the collision rate inside the trap and the atomic flux into the trapping region. In this simple picture, atoms are not lost from the trap, as they would be in reality by two-body inelastic collisions or Majorana losses (Majorana 1932; Brink et al. 2006), for example. Simulating the loading process in this model results in the fraction of all atoms that are trapped in the dipole potential and a loading time at which equilibrium is achieved. Losses in this approach can be introduced in terms of the collision times, where the static character of the solution is preserved.

A more complex model for the same situation, including temporal behavior, results in a loading curve similar to the one seen in Figure 3.9 (Landini, S. Roy, Roati, et al. 2012).

For this experiment, magnetic traps are excluded, since they require high currents, which are difficult to implement in a drop capsule. The approach of cooling atoms in a magnetic trap on a so-called atom chip works well in microgravity (Zoest et al. 2007; Rudolph et al. 2011). These devices minimize power consumption by in-vacuum wire structures³ but come with other disadvantageous explained in the introduction in Chapter 1.

³Lately atom chips were also placed outside the vacuum cell (Squires et al. 2016) or became part of it (Du et al. 2004; Du 2005).

3.3.2. Overlapping MOT and Dipole Trap

The transition of atoms from one trap to another is most effective, if both traps are operated simultaneously, at least for a short time. In the particular case of a MOT and a dipole trap, this may worsen both individual performances, up to a point where loading gets impossible. The interaction behavior mostly depends on the wavelength of the dipole trap λ . As mentioned in the introduction to this chapter, the trapping mechanism can be understood as an AC-stark shift of internal atomic energy levels (Dalibard and Cohen-Tannoudji 1985; Alt 2004). As described in Section 3.1, a MOT works on transitions between the same energy states. Since the dipole trap is smaller than the MOT, this results in an effective spatial variation for the MOT beam detunings. These were carefully optimized to match the magnetic gradient and laser power in the experimental setup.

The introduced two level system is, of course, a simplified model to understand the dipole trapping basics. A more sophisticated description of the complex polarizability $\alpha_p(\omega_L)$ including all relevant optical transitions shows that it is possible to lower or raise energy levels of excited and ground states individually (Grimm et al. 1999). Three possible cases will be discussed here with its most typical exemplary representatives. The following section is exclusively related to rubidium.

Dipole trapping at $\lambda \approx 1 \mu\text{m}$: Trapping in this range rises the excited state, resulting in a MOT beam detuning to the red. A MOT can still be operated but with altered performance. Atoms in the excited state are repelled from the trap center while a reduction in absorption from the MOT beams leads to a higher density for ground state atoms. It is possible to load a dipole trap in these conditions directly from a MOT (Arnold et al. 2011; Nes 2008; W. Hung et al. 2015) but it is more common to implement an intermediate step like a magnetic trap (J. Will 2007; Chisholm et al. 2018) or different optical potentials (Kinoshita et al. 2005).

Dipole trapping at $\lambda \approx 1.5 \mu\text{m}$: In the range around $1.5 \mu\text{m}$ the excited state is lowered significantly. Creating a reasonable trap depth results in a crossing for excited and ground state energy levels. Standard MOT operation is no longer possible but atoms can still be directly loaded by largely detuning the MOT beams as will be explained in Section 3.3.4 (Clément et al. 2009). The problem can also be overcome by introducing an intermediate magnetic trap (Lin et al. 2009).

Dipole trapping at $\lambda \approx 10 \mu\text{m}$: A dipole trap this far away from all optical resonances of rubidium acts equally on all energy states. A situation like this is called **Quasi Electro Static Trap (QUEST)**. Both, excited and ground state are shifted by the same amount in the same direction and do not affect the MOT's performance at all, so atoms can be trapped directly (M. D. Barrett et al. 2001; Cennini et al. 2003).

In the experiment, described in this thesis, rubidium atoms are trapped with a wavelength of $\lambda \approx 2 \mu\text{m}$. This regime lies between the two latter cases described above and behaves as expected. The excited state is lowered a bit stronger than the ground state. For the laser power provided by our trapping laser ($<10 \text{ W}$), it is not possible to have them crossed. Cal-

3. Dipole Trap Loading

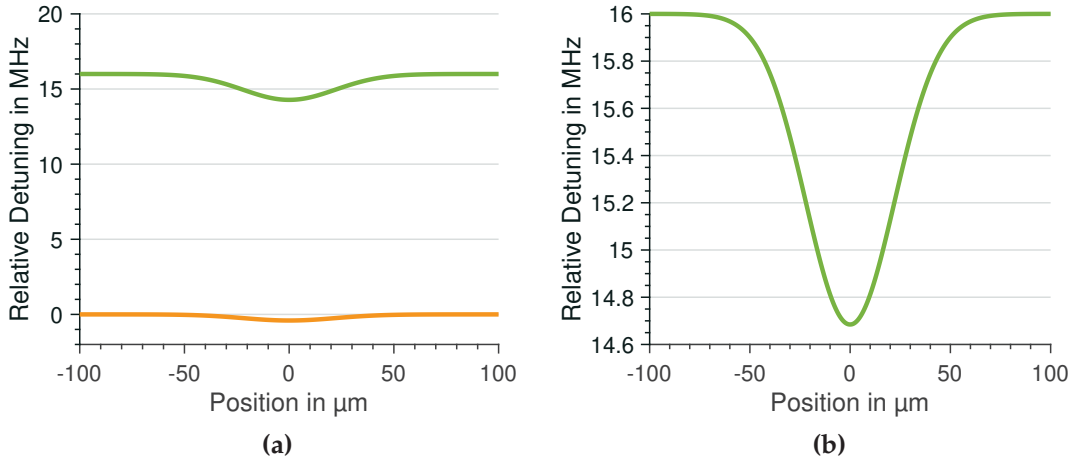


Figure 3.8

Spatial dependency of dipole laser induced energy shifts for the parameters of our experimental setup. (a) Illustrated is the situation in a MOT configuration. Far away from the center the ground and excited energy states are displaced by 16 MHz corresponding to the optimal cooling light detuning in our experiment. Towards the center, due to energy shifting based on the AC Stark effect, both energy levels are differently effected, leading to a spatial dependent effective detuning. (b) Energetic distance between both states. An effective shift of 1.3 MHz does not disturb MOT operation.

culations for the specific conditions of our experimental setup are shown in Figure 3.8. Here one can see the undisturbed MOT detuning of 16 MHz at the dipole trap edges. Towards the trap's center, the detuning is decreased by 1.3 MHz to 14.7 MHz (Figure 3.8 b). The consequences of this are of minor importance to the overall performance, as can be seen in Figure 3.1.

Further Thoughts on Wavelength Choice

When building a complex experimental apparatus to operate in weightlessness, simplicity is the key. This has also been considered in the choice of dipole trapping wavelength. On one hand, a $10 \mu\text{m}$ trap, as it is provided by CO_2 lasers, is easily directly loadable from a MOT. It has the highest confinement along the beam axis, due to a small Rayleigh length, in a single beam configuration (Equation (3.14)) and, as described in Equation (3.12), atom losses from the trap, caused by scattering processes, are strongly suppressed. On the other hand, this wavelength requires special optics and a higher laser power to provide the desired trap depth, in comparison with shorter wavelength. For $1 \mu\text{m}$ and $1.5 \mu\text{m}$ traps the direct loading from a MOT is difficult and requires more complex schemes. Furthermore, a larger Rayleigh length means less confinement in beam direction and an increased energy transfer from photon scattering events on the trapped ensemble. The chosen wavelength of $2 \mu\text{m}$ combines all the named advantages with no scientific drawbacks. So far, only the limited availability of commercial lasers and optical elements hinders a wider spread in current applications.

3.3.3. Loading Directly from the MOT

The most simple technique to load a dipole trap is: cooling the atoms in a MOT, switching it off, and immediately turn on the dipole trap laser (Brantut et al. 2008). No interaction between both traps has to be considered, however only a small fraction of atoms is captured. Basically all atoms initially inside the trapping area with energy lower than the trap depth are captured, reducing the trapping probability, in one dimension, to the two ratios of σ_0/w_0 and $U_0/k_B T_0$ (Gaaloul et al. 2006). σ_0 represents the size of a Gaussian distributed atomic cloud while w_0 is the dipole laser beam waist.

Another way to overcome the problem of incompatible MOT and wavelength combinations is to operate them alternately (Miller et al. 1993). If switching is fast enough, atoms will see a time averaged potential from both traps. However, the effective laser power in time averaged dipole potentials is lower than the provided optical power by the laser making loading less effective.

Attention should be paid to theoretical models of these simple cases because they deliver the basis for more sophisticated procedures. If atoms are loaded from a standard MOT the atomic reservoir is still in equilibrium, but photon interaction has to be involved. In the most simple case of a QUEST, or any other dipole trap that does not affect the MOT performance, a simple static equation is a good approximation for the number of loaded atoms (O'Hara, Granade, et al. 1999a)

$$N_T = nV_{FORT}F(\eta). \quad (3.24)$$

Here N_T represents the number of trapped atoms, n is the atomic reservoir density, V_{FORT} the trap volume and $F(\eta)$, proportional to $\left(\frac{U_0}{k_B T}\right)^{3/2}$, gives the number of trapped atoms in relation to all atoms inside the trap area.⁴

Most choices of wavelengths will lead to some kind of interplay between MOT and dipole potential. Kuppens *et al.* determined the detuning and intensity of the MOT beams as key parameters for an efficient dipole trap loading (Kuppens et al. 2000). The loading dynamics are well described by

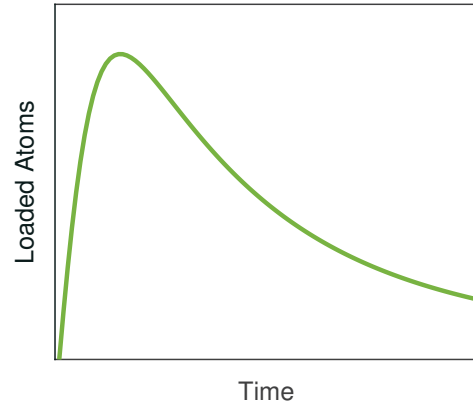


Figure 3.9
Theoretical dipole trap loading curve described by Equation (3.25). An initially high loading rate decreasing in time is followed by a loss dominated regime, defining an optimal loading time.

⁴Basically the same assumptions were taken in (Ahmadi et al. 2005), leading to a slightly different representation some people may find more convenient.

3. Dipole Trap Loading

$$\frac{dN_T}{dt} = R_0 e^{-\gamma_{MOT} t} - \alpha N_T - \beta N_T^2 \quad (3.25)$$

with the number of trapped atoms N_T , the initial loading rate R_0 , the MOTs loss rate caused by the decreased MOT performance γ_{MOT} , a density independent loss rate α and a density dependent loss rate β . Since α is dominated by encounters between trapped and residual gas atoms, it is strongly correlated to the vacuum quality of the system. The value for β is equal in any experiment, depending on the atomic species and its state population. Anyway, both, α and β can be extracted from the observed linear and the quadratic loss term, respectively.

In Figure 3.9 one can see an efficient loading dominated by the loading rate from Equation (3.25) in the beginning followed by a domination of loss mechanisms.

In order to maximize the number of trapped atoms, one has to maximize the initial loading rate while minimizing loss mechanisms. Several effects can lead to loss of atoms from the trap as it is discussed in Chapter 4, but as long as MOT and dipole trap operate at the same time they are dominated by MOT light induced radiative escape effects. The initial loading rate can theoretically be described by (Kuppens et al. 2000)

$$R_0 = \frac{1}{4} n_{MOT} \bar{v} A P_{Trap}, \quad (3.26)$$

where n_{MOT} means the atom number density in the MOT, $\bar{v} = \sqrt{k_B T / m}$ is the average velocity and A describes the effective dipole trap surface area; P_{Trap} is the probability to catch an atom

$$P_{Trap} = \frac{1}{2} \left\{ 1 - \operatorname{erf} \left[\frac{\bar{v}}{\sqrt{2}\sigma_b} \left(1 - \sqrt{\frac{\alpha_f \tau}{m}} \right) \right] \right\}. \quad (3.27)$$

This formula was derived from the idea of atoms with a narrow velocity distribution entering the trap and interacting with photons while they are crossing the trapping region (τ is the oscillation period in the trap). Photon interaction leads to a velocity broadening, represented by σ_b , and friction, implemented in α_f with

$$\sigma_b = \sqrt{\frac{1}{3} \left(\frac{\hbar k}{m} \right)^2 \Gamma_{sc} \frac{\tau}{2}} \quad \text{and} \quad \alpha_f = -2 \frac{s_0}{(1+s_0)^2} \hbar k^2 \frac{\delta \Gamma}{\Delta_{cool}^2 + \Gamma^2/4}. \quad (3.28)$$

Here Γ_{sc} describes the photon scattering rate, $s_0 = I/I_{sat}$ is the saturation parameter, Δ_{cool} the cooling light detuning and Γ the natural line width of the cooling transition.

Another important criterion for an efficient loading is the spatial overlap between MOT and dipole trap. Apart from the interplay between both traps, a coinciding trap center was found to be less efficient than a slight displacement in the dipole trap's beam direction. This shift leads to a wider trapping beam diameter with a sufficiently potential deep trapping potential (Szczepkowicz et al. 2009). In (Kuppens et al. 2000) the trap depth dependent optimal displacement was found to be on the order of half a MOT diameter. Because the actual value

depends on various parameters for the MOT and the dipole trap, this value can only give an idea of the possible optimal displacement.

The major drawback of this technique is the relatively high temperature of transferred atoms. In the current setup, MOT trapped atoms have kinetic energies in the order of the dipole trap's potential depth. An efficient loading under these conditions is impossible.

3.3.4. Loading from a Compressed MOT

From Equation (3.24), it is obviously favorable to have high atomic densities and low temperatures for the efficient loading of a dipole trap, directly from a MOT. Slight modifications of the MOT's magnetic field or detuning can compress the atomic cloud and increase the loading efficiency tremendously. While these so-called compressed MOTs (CMOTs), are effective in preparing the loading process, they are inefficient in trapping atoms. Therefore, CMOTs are generally operated for short times, in the range of ms, as an additional step to a standard MOT, before transferring or releasing an atomic ensemble.

Temperature reduction:

Generally the lowest attainable temperature in a MOT is expected to be the Doppler-limit, which is $140 \mu\text{K}$ for rubidium-87. In contrast, the lower limit in a molasses (see Section 3.3.5) is the recoil limit with 362 nK . Without further detail, an optical molasses describes the same situation as in a MOT, but without any external magnetic fields. The absence of magnetic fields enables polarization gradient cooling, which allows for sub-Doppler temperatures.

Since the MOT operates on a magnetic quadrupole field, the exact center of a MOT is magnetic field free, providing the same conditions as given in a molasses. In fact, polarization gradient cooling occurs in an area around the MOT center, where the Zeeman-shift is smaller than the ground state's ac-Stark shift. Therefore, the lowest attainable temperature in a MOT (T_0) is equivalent to the equilibrium temperature for (low-density) atoms in a molasses. While the sub-Doppler cooling effect is negligible for standard MOT operating parameters, it becomes significant for larger cooling light detuning as applied in a CMOT. In these conditions the relation

$$T_0 \propto \frac{I_{MOT}}{\Delta_{cool}} \quad (3.29)$$

with the MOT light intensity I_{MOT} and the cooling light detuning Δ_{cool} can be found.

Furthermore, the cooling mechanism of a MOT is based on absorbed photons, which later on are isotropically reemitted. With a certain probability, scattered photons will be reabsorbed by other atoms in the cloud (D. W. Sesko et al. 1991). This process amplifies with atom number and increases the energy transfer into the atomic ensemble. A high reabsorption rate will thus lead to higher temperatures with the relation (Cooper et al. 1994)

$$T \propto N_T^{1/3} + T_0. \quad (3.30)$$

3. Dipole Trap Loading

According to Equation (3.30) and (3.29), a lower temperature in a CMOT can be realized by a lower atom number, higher detunings and less power in the cooling light beams. An additional reduction of the repumping beam intensity results in an increased number of atoms in the $F=1$ state for rubidium-87, an effect known as *dark MOT* (Ketterle, K. B. Davis, et al. 1993). A large amount of atoms are in this way shifted out of resonance for any cooling light, thus reducing reabsorption.

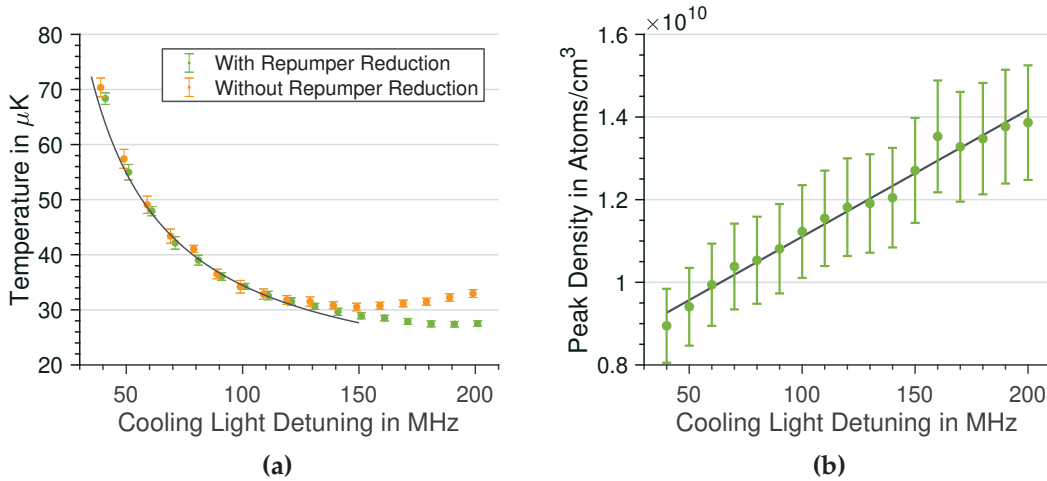


Figure 3.10

(a) Temperature dependency of the cooling light detuning in a compressed MOT. Measurements with (green) and without (orange) a further repumping beam reduction are shown. Up to 150 MHz, both situations can be described by the inversely proportional temperature dependency on the detuning $T \propto 1/\Delta$ from Equation (3.29), depicted by the solid line. Temperatures were determined by the time of flight method⁵. (b) The same procedure of increased cooling light detuning also leads to an increased atomic density in the CMOT with the linear dependency predicted in (Perrin 2014).

In Figure 3.10 (a) one can see the influence of an increasing cooling laser detuning. Starting with a MOT temperature above $200 \mu\text{K}$ for 16 MHz (not shown here) the ensemble cools down rapidly with increased cooling light detuning. The solid line marks the inverse proportionality $T \propto 1/\Delta$ indicated in Equation (3.29). Clearly, both data sets, i.e. with and without the repumping light reduction, show this inverse proportionality up to 150 MHz. Up to this frequency, a repumping laser intensity reduction has only a minor effect on the atoms. Above 150 MHz both lines separate. While an intensity reduction further cools the atoms, the temperature starts to rise again for a fully repumped system. The same behavior can be found in (Maic Zaiser 2010)⁶. Larger detunings can not be realized in the experiment due to hardware limitations. This is tolerable since, according to the trend in Figure 3.10(a) only a modest improvement can be expected. The effect of the dark MOT is also illustrated in Figure 3.11(a). While a lowered

⁵Time of flight (TOF) measurements refer to a technique where atoms, released from a trap, are thermally expanding and the temperature is determined from the cloud size after a certain time of flight. Here the spatial distribution is recorded by fluorescence on a CCD camera (Pyragius 2012). This is different from the more common technique where atoms are falling through a probe beam (Lett et al. 1988).

⁶Detunings in this reference have to be multiplied by 2π .

repumping intensity is only efficient for very small values of only a few hundred $\frac{\text{mW}}{\text{m}^2}$, a thousand times less than for standard MOT operation, shutting off this light reverses the desired effect.

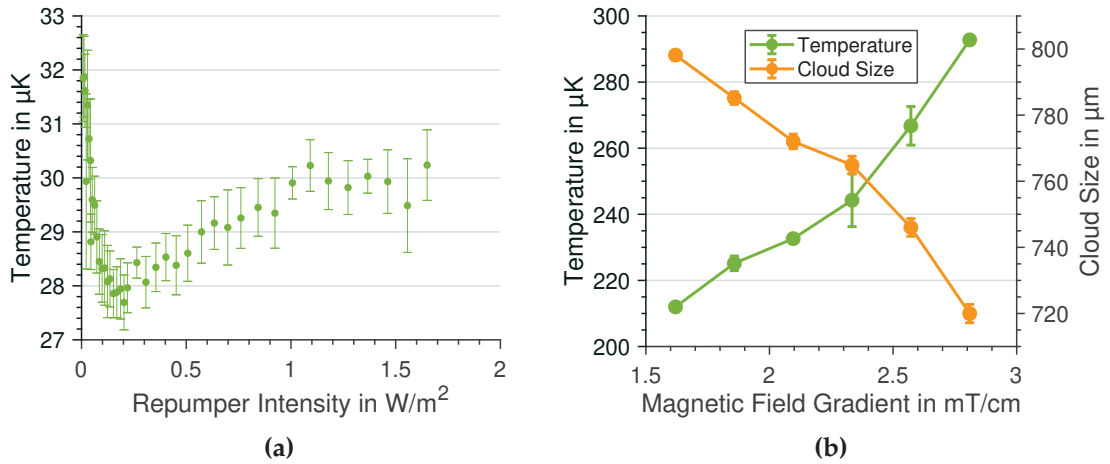


Figure 3.11

(a) Shown is the temperature dependency on repumping laser power. A large number of atoms in the $F=1$ state, reduces the intensity of scattered light in the ensemble, this directly translates to lower temperatures. (b) Temperature and cloud size of a compressed MOT over the magnetic field gradient in the chamber. A steeper gradient increases the ensemble's density but also leads to higher temperatures.

Density increase:

Photon scattering does not only affect the cloud's temperature but also its density by reabsorption effects, light induced collisions (D. Sesko et al. 1989) and hyperfine changing collisions (Gallagher et al. 1989; Gensemer et al. 1997). If a photon is scattered within the ensemble and gets reabsorbed by another atom, it is easy to see that a momentum of $2\hbar k$ was transferred. Thus, acting as a repulsive force which lowers the density. Accordingly, the temperature decreasing scheme introduced above, acts density increasing as well. This behavior is illustrated in Figure 3.10(b).

Another approach to reach high densities is to increase the magnetic gradient (Petrich et al. 1994), which goes along with an undesired temperature increase. Measurements shown in Figure 3.11(b) demonstrate this behavior in our setup. No parameters could be found to improve the FORT loading efficiently by increasing the magnetic gradient.

CMOT times on the order of a few ms are insignificant, compared to evaporation times in the order of seconds. Nevertheless, it was tested how fast the temperature decrease can be established, resulting in only one ms until the final temperature is reached. In experimental sequences, performed in the drop tower, this time was stretched anyway to guarantee a smooth and stable frequency shift. This measurement is an impressive example of how fast optical cooling techniques are, compared to evaporative cooling. The latter is introduced in Chapter 4 as a further cooling step. Since time is a critical factor in most applications, and especially in the

3. Dipole Trap Loading

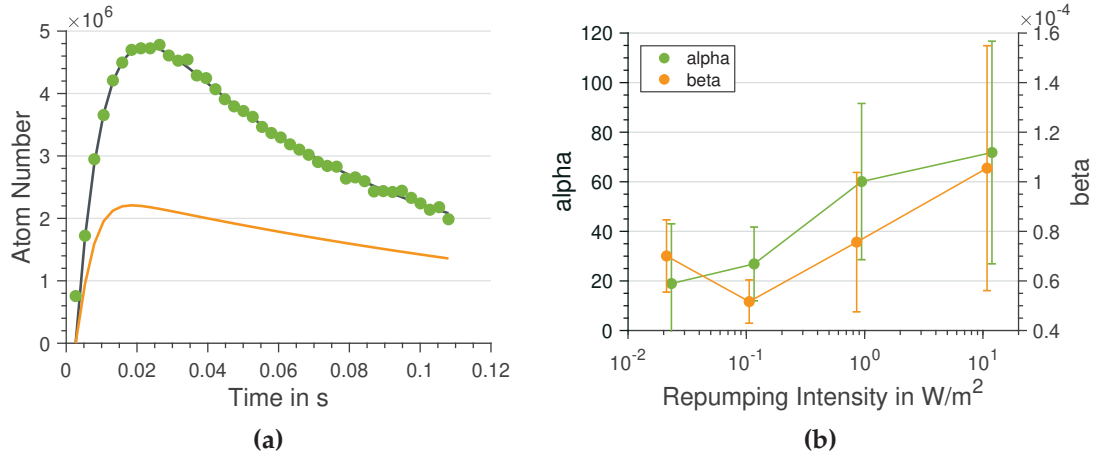


Figure 3.12

(a) Number of trapped atoms over time for a dipole trap loaded from a compressed MOT. Green dots are measured data including a fit to Equation (3.25) in gray with the parameters: $R_0 = 1.05 \times 10^9 \frac{\text{atoms}}{\text{s}}$, $\gamma_{\text{CMOT}} = 122.2 \frac{1}{\text{s}}$, $\alpha = 4.24 \frac{1}{\text{s atom}}$ and $\beta = 2.1 \times 10^{-6} \frac{1}{\text{s atom}}$. The orange curve shows results from a different measurement approach described in the text. (b) Measured values for density dependent and independent loss parameters α and β for different repumping laser powers. A reduced intensity results in more atoms in a dark state reducing β . The unexplainable reduction in α is an indicator for an improper measurement technique.

drop tower, it is favorable to reach the coldest possible temperature via optical methods before starting the evaporation.

From a theoretical point of view, the dipole trap loading process from a CMOT is close to the situation described in standard MOT loading. The difference lies in varying parameters which lead to time dependent loss coefficients. Figure 3.12 shows the recorded atom number loaded into the trap over time. The dataset is additionally fitted with Equation (3.25). The very good agreement is somewhat surprising for static parameters, describing a rather dynamic situation. For this reason an attempt was made to confirm the determined values of $R_0 = 1.05 \times 10^9 \frac{\text{atoms}}{\text{s}}$, $\gamma_{\text{CMOT}} = 122.2 \frac{1}{\text{s}}$, $\alpha = 4.24 \frac{1}{\text{atom s}}$ and $\beta = 2.1 \times 10^{-6} \frac{1}{\text{atom s}}$ with independent measurement techniques proposed by Kuppens *et al.* (Kuppens et al. 2000) but, as described now, without success. Since the parameters could be gained anyway, this is just a side note for future experimentalists.

The initial loading rate R_0 can directly be extracted as the initial slope (first three data points) of the measured curve in Figure 3.12, resulting in $4.1 \times 10^8 \frac{\text{atoms}}{\text{s}}$, a value smaller than the fitted one by over a factor of two.

The measured compressed MOT decay rate γ_{CMOT} deviates from the fitted value by over a factor of ten (not shown here). Linear and quadratic loss rates, α and β respectively, were determined by a lifetime measurement under the actual loading conditions. To understand the behavior of the values for varying CMOT parameters, measurements were conducted for different values

of the repumping intensity. As displayed in Figure 3.12(b), it revealed a decrease in both, α and β . While this behavior is expected for density dependent losses, the linear loss rate, mainly governed by collisions with background gas, should be independent of internal atomic states. Inserting the independently gathered parameter into Equation (3.25), results in a rather bad representation for the measured dataset. The resulting curve is plotted as orange line in Figure 3.12(a). While the loss rate measurement obviously failed, the massive underestimation of our loading rate emphasizes a strong correlation between the parameters, making it impossible to precisely determine them individually in our system.

In conclusion, Equation (3.25) excellently describes the dipole trap loading curve from a CMOT, if all parameters are fitted at once. Since the trapping multimode laser drives the same transitions as the repumping laser, the atoms' state distribution is somehow undefined and prohibits an individual parameter determination as suggested by Kuppens *et al.*

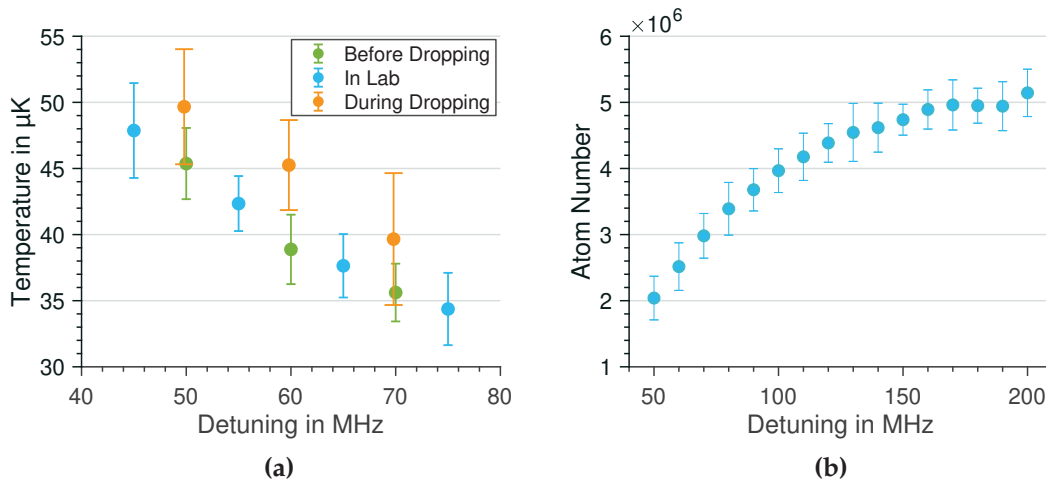


Figure 3.13

(a) CMOT performance measured in the lab, just before and during the drop. A slightly worse performance in microgravity is related to less stable laser frequency performance and has no fundamental underlying physical effect. (b) Number of atoms loaded into the dipole trap using the CMOT technique for different cooling laser detunings. The higher density and lower temperatures form a CMOT constantly increase the number of loaded atoms. In optimal conditions 5×10^6 atoms can be loaded into the trap.

The CMOT performance has also been investigated in microgravity. To minimize systematic performance fluctuations, measurements were performed in the lab, just before the transfer to the drop tower, as well as seconds before the dropping, hanging in the drop tower, and during the dropping. As can be seen in Figure 3.13(a), the laboratory situation gives equal results to the one before the dropping but the temperatures in microgravity are slightly increased. This is most likely attributed to a worse performance of laser frequency shifts. This assumption is deduced from increased fluctuations on the monitored laser driving currents.

3. Dipole Trap Loading

Following these theoretical considerations, confirmed by the given measurements, an effective dipole trap loading in our setup requires the highest cooling light detuning possible and just a small amount of repumping light, while keeping the magnetic gradient at a static value for 22 ms. As displayed in Figure 3.13(b) following this recipe $\approx 5 \times 10^6$ atoms can be loaded into the dipole trap. A temperature for the trapped atoms can not be determined, because of the fast natural evaporation, a cooling mechanism (Chapter 4), from the trap. This could be circumvented by short delay times between loading and measurements, but in this regime the strong fluorescence signal from non trapped atoms covers all signals from trapped atoms.

3.3.5. Loading from an Optical Molasses

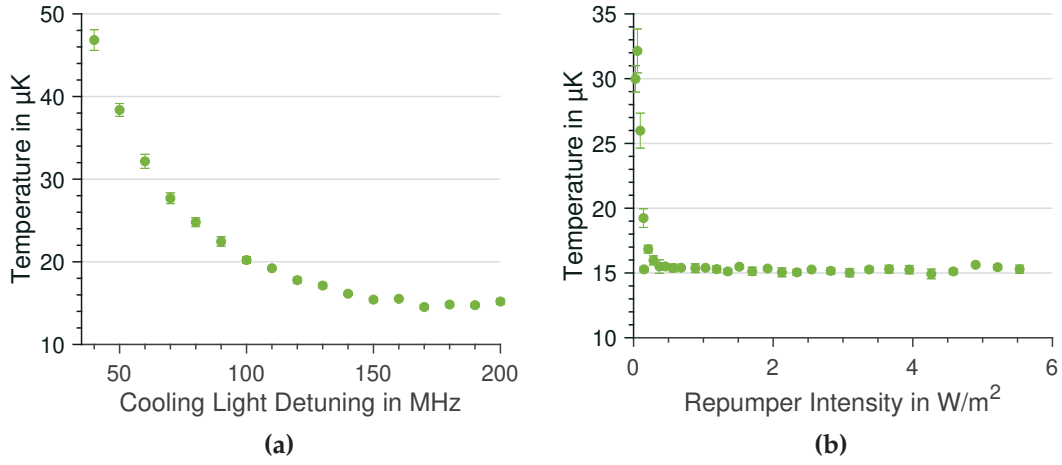
Molasses cooling (Steven Chu, Hollberg, et al. 1985) is a different cooling scheme that can follow after a MOT phase. For this technique the magnetic trapping fields are switched off. By doing so, the spatial dependence of radiation pressure on the atoms is lost. Atoms are no longer confined in a certain area but immediately expand. The advantage of a molasses, over the compressed MOT, is an efficient sub-Doppler cooling mechanism all-over the atomic cloud, that was unexpectedly discovered (Lett et al. 1988). It is based on variations in the polarization of the cooling laser beams, leading to Sisyphus cooling. The term refers to an ancient Greek legend and describes atoms that continuously travel up a potential hill, followed by an optical depumping to a lower potential state (Cohen-Tannoudji et al. 1990; Metcalf et al. 1999).

In rubidium, temperatures as low as $\approx 2 \mu\text{K}$ were observed, cold enough to perform atom interferometry (Louchet-Chauvet et al. 2011). In combination with potassium, molasses cooled rubidium was the basis for the, up to now, most precise test of the weak equivalence principle with different atomic species (Schlippert 2014).

An effective molasses cooling depends on precisely balanced radiation pressure from all six cooling beams and a true magnetic field-free environment. Detuning the cooling laser frequency to the red results in a similar, but more effective temperature decrease compared to the CMOT as can be seen in Figure 3.14(a). An additional reduction of the repumping laser power did not lead to a further temperature decrease. It could only be confirmed that a small amount of repumping laser is always necessary, as shown in Figure 3.14(b).

The final temperature of $15 \mu\text{K}$ is limited most likely by beam imbalances. In this setup, light is transferred from the uppermost platform of the capsule, to the vacuum chamber via a fixed ratio fiber splitter. Even though the splitting ratio is supposed to be equal for any exit port, measurements revealed strong deviations from an equal distribution (Kulas 2016). Variations between ports can reach up to 8 % and are not stable in time, most likely due to temperature variations in the laboratory environment. Changes were not constantly monitored but observed over the course of years.

A theoretical description for the loading process of a dipole trap from an optical molasses is given in the references (Pruvost et al. 1999; Wolschrijn et al. 2002). The biggest difference to a compressed magneto-optical trap is the lack of spatial confinement as described earlier. For

**Figure 3.14**

Temperature dependencies of (a) cooling light detuning and (b) repumping intensity in a molasses. (a) The highest possible detuning in our setup (≈ 200 MHz) leads to a temperature of $15 \mu\text{K}$, $10 \mu\text{K}$ lower than the best results for a CMOT. (b) The temperature dependency on repumping intensity differs from a CMOT. No increase towards higher power was observed making it a stable solution, especially suitable for microgravity operation.

this reason, atoms will only pass the trapping area once, making it feasible to ignore loading by scattering effects. Pruvost *et al.* expect all atoms to be caught in the trap that are initially in the trap volume and have a total energy smaller than the trap depth. Considering all atom positions and momentums to be Gaussian distributed leads to

$$\frac{N_T}{N_0} = \iint_{\frac{p^2}{2m} + U(r) \leq U_0} \frac{1}{2\pi m k_B T_i} e^{-\frac{p^2}{2m k_B T_i}} \times \frac{2}{\pi \sigma_i^2} e^{-\frac{2r^2}{\sigma_i^2}} 2\pi r dr 2\pi p dp \quad (3.31)$$

where N_T describes the number of trapped particles and N_0 the number of atoms in the molasses. p is the atom's momentum, m its mass and σ_i the width of the spatial Gaussian atomic distribution. Since this equation originates from the loading of an optical guide it only describes a two dimensional problem. A simple possibility to mimic the third dimension is to multiply a linearly growing correction factor. This is only valid for low trapping powers, since it does not take the actual cloud size into account.

Loading from a molasses is found to be more efficient than loading from a CMOT. In Figure 3.15(a) a maximum loaded atom number of $\approx 8.5 \times 10^6$, compared to $\approx 4.8 \times 10^6$ in a CMOT, is observed. The curve's drop above 230 MHz has no scientific reason but is introduced by technical limitations on frequency shifting in our particular system.

In Figure 3.15(b) the dependency between the number of loaded atoms and dipole trap laser power is plotted. The gray line is a fit to Equation (3.31) including a linearly growing correction factor. A strong correlation between trapping power and the number of loaded atoms becomes

3. Dipole Trap Loading

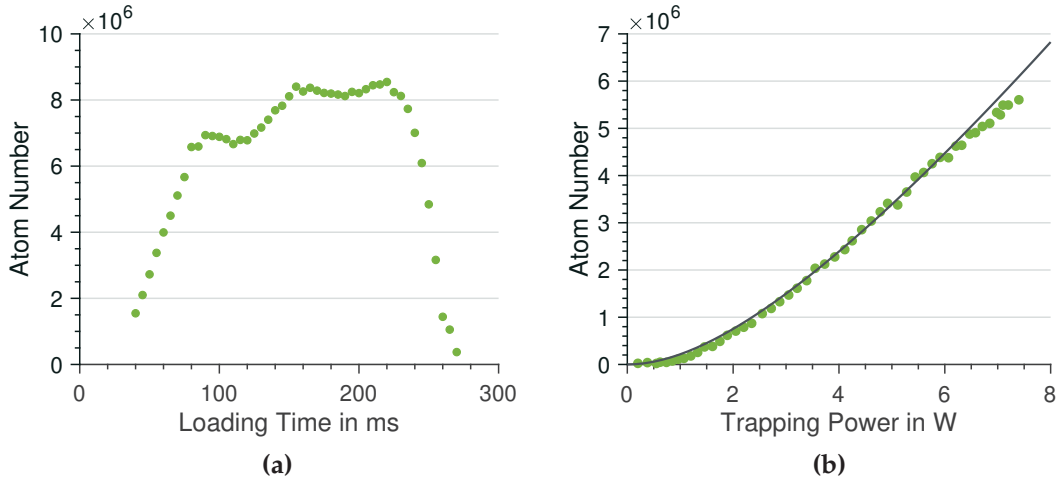


Figure 3.15

Molasses dipole trap loading results. (a) Number of loaded atoms over cooling light detuning. A maximum of more than 8×10^6 atoms can be transferred to the dipole trap, a distinct improvement over CMOT results. (b) Number of loaded atoms in dependence of dipole trap laser power. The recorded data (green dots) verifies Equation (3.31) with the included correction term (gray line). For laser power above 6 W the slight discrepancy from theory might be a hint for a saturation effect onset. Both measurements are not consistent, since they were performed with slightly different MOT parameters.

obvious. Nevertheless, at a certain power this curve saturates, because all available atoms are trapped (Ahmadi et al. 2005). It is unclear whether the slight deviation for high trapping powers indicates this behavior. Further investigations are impossible due to the limited available laser power. Ahmadi *et al.* found saturation at $\eta = 4$ which would correspond to a trapping power of $P_0 \approx 6$ W. Equation (3.31) and our measurements on evaporation (Chapter 4) suggest saturation at $P_0 \approx 9$ W ($\eta = 6$). For this reason an increased trapping laser power would only slightly improve the number of initially loaded atoms.

For ODTs formed by multimode lasers, as applied in the PRIMUS experiment, the number of loaded atoms possibly even decreases with high laser powers (Landini, S. Roy, Roati, et al. 2012). This is related to an additional loss mechanism, caused by hyperfine state changing collisions (Lauber et al. 2011; Weiner et al. 1999; W. Hung et al. 2015). For the available range of laser power in our experiment, no additional loss mechanisms could be observed in the dipole trap loading curve.⁷

Theoretically, the optical forces in the molasses cooling technique have no defined spatial dependency, but are velocity selective. In reality, minor spatial dependencies result from beam intensity imbalances, caused by improper beam intensities or local defects, like dust or lens imperfections on optical elements. Therefore, while switching from a MOT to a molasses, the atoms start to move slowly and their movement is effected by gravity.⁸ Since the overlap between a dipole trap and an atomic ensemble is a key factor for an efficient loading, the parameters

⁷The described loss effect could anyway be identified in dipole trap lifetime measurement in Section 4.5

⁸The atomic ensemble disappears from the cooling region on the order of seconds (Arthur Ashkin 2006)

optimized on ground are not necessarily the ideal ones for drop tower operation.

In Figure 3.16 one can see a comparison between operation with and without gravity for different molasses holding times. The total amount of loaded atoms does not significantly differ, but there seems to be a shift towards longer times for optimal loading. This perfectly agrees with the argument of a non falling atom cloud, being in overlap with the trap for a longer time period, while a falling cloud would shift away from the trap. However, these data were recorded in a single drop and to provide a definite conclusion would require to take further data. Even though this information might be of great interest for future space missions, it is unlikely to drastically improve our experiment's performance. Further investigations of this topic are discussed in the outlook section of this thesis.

3.3.6. Loading from an Optical Lattice

Loading a dipole trap from an optical lattice is not an alternative to the techniques introduced above, but must be understood as an additional intermediate step before starting the evaporation. Strictly speaking, loading the lattice itself is already a procedure of loading an optical potential. Although this experimentally complex method will not be implemented in the current or near future setup of the PRIMUS project, its benefits open up a desirable alternative in the future and are therefore mentioned here already.

Recently a remarkable achievement was published by Hu *et al.* They trapped atoms in an optical lattice and laser cooled them to quantum degeneracy within only 300 ms (Hu *et al.* 2017). Out of the large number of scientific publications describing the creation of BECs, this work is the only one without employing evaporative cooling at all.⁹ Nevertheless, the generated ensemble is rather hot with a few μK and contains only about 1000 atoms. Therefore it is not suitable as a source for atom interferometry in microgravity, but impressively demonstrates the possibilities of this technique.

Optical cooling in lattices can be implemented either by polarization gradient cooling (PGC) (Winoto *et al.* 1999) or by Raman sideband cooling (Heinzen *et al.* 1990; Hamann *et al.* 1998). PGC in an optical lattice is similar to performing it in free space, but since atoms stay in a certain

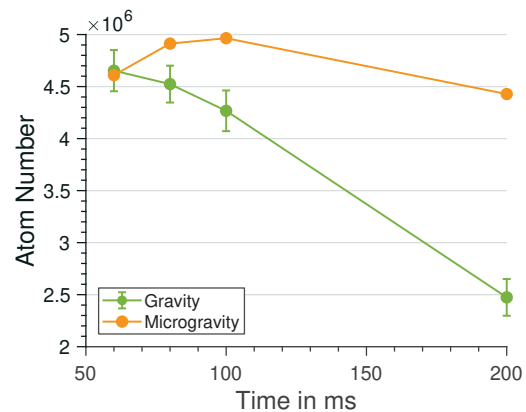


Figure 3.16

Comparison between the number of atoms loaded into a dipole trap on ground and in microgravity. Because the molasses cooled atoms do not fall under gravity loading times can be extended with a seemingly slightly increased number of loaded atoms.

⁹BECs can also be created by a reversible process with local compression in a larger reservoir of cold atoms. Here the transition itself is not driven by evaporation but it is applied to come close to the degenerate regime (Stamper-Kurn *et al.* 1998).

3. Dipole Trap Loading

position, the cooling parameters can be optimized independently from any trapping character. The result is an ensemble with an even higher fraction of atoms in the dark state than it is the case for our molasses cooling. The second advantage is the compression of atoms on lattice sites which increases their temperature to a point where laser cooling becomes effective again. After this procedure the lattice can be ramped down adiabatically, leaving a very cold, fast produced, atomic cloud. By this technique, temperatures in cesium could be lowered by more than one order of magnitude, from $10\ \mu\text{K}$ to $650\ \text{nK}$ (Winoto et al. 1999) and even further to $350\ \text{nK}$ (DePue et al. 1999). In rubidium-87, Kinoshita *et al.* reached a phase space density of $1/550$ at a temperature of $1.2\ \mu\text{K}$. With this suitable conditions to start evaporation and some other tricks, BECs can be produced within 3.3 s.

Raman sideband cooling is a process based on vibrational state degeneracy for different magnetic substate levels. While the vibrational energy for all m_F states is generally the same, they can be shifted by applying an external magnetic field. The idea is to bring different vibrational states into degeneracy. Now atoms can change to different vibrational states via Raman transitions without energy changes. The higher states can then be pumped back optically to a lower state, resulting in a cooling effect. The process was first demonstrated in cesium (Kerman et al. 2000; Han et al. 2000; Treutlein et al. 2001) but could also be applied to potassium (Gröbner et al. 2017) for example. As mentioned above, a BEC creation without applying evaporation was demonstrated in rubidium. For larger atomic ensembles, results with a temperature of $1.2\ \mu\text{K}$ and a PSD of $1/500$ (Wei et al. 2017), are similar to PGC results.

Optical lattices are generated by overlapping single frequency laser beams from at least two directions, in most cases retro reflected. At this point a single frequency laser with the demanded output power at a wavelength of $2\ \mu\text{m}$ is just not available, but switching to $1064\ \text{nm}$ in the future might be an appropriate alternative. Another problem is the limited optical access of our vacuum chamber. Dedicated optical ports for such a lattice are not available. Of course viewports could be shared for multiple functions but this would introduce mechanical instabilities into the system. Such a step has to be well-thought-out.

3.4. Determination of Trap Frequencies

Three measurement techniques are known to estimate dipole trap frequencies without any a priori knowledge: direct observation, via changes in the ensembles temperature or particle losses.

In the **direct observation** method, atoms are displaced from the center of the trap, leading to an oscillation with the trap frequency. This can, for example, be done by lowering the dipole laser power resulting in a shifted balance between dipole and gravitational force. In most cases, it is also possible to shift atoms via magnetic fields.

Trap frequency measurements by **temperature changes** are based on the concept of a driven oscillator. When the dipole trap power is modulated at twice the trap frequency, or at its overtones, atoms are resonantly driven, leading to an increased temperature in the system.

Scanning through several driving frequencies results in at least one peak in temperature, as can be seen in Figure 3.17(a).

The third possibility, measuring via **particle losses**, can also be implemented by a power modulation, similar to the temperature changing method (Friebel et al. 1998), where an increased temperature leads to an increased atom loss as well. Another particle loss technique is called the release-recapture method (Engler et al. 2000). It starts with a sudden dipole laser shut off, letting the atoms fall ballistically. This is followed by a sudden switch on that recaptures most atoms, now in an out of equilibrium position in the trap which forces them on an oscillation trajectory. Repeating the same sequence, with a variable delay time in between, connects the number of atoms finally captured to the phase of in trap oscillations.

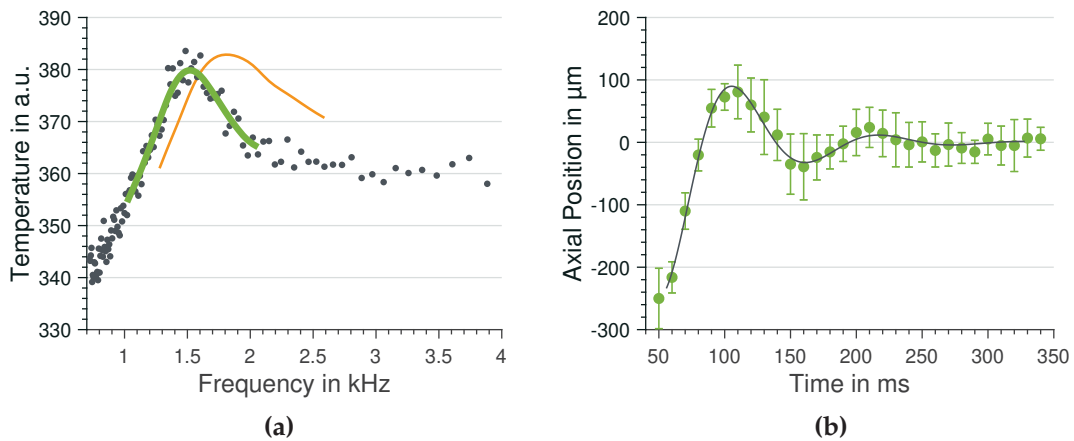


Figure 3.17

Dipole trap frequency measurements. (a) By modulating the laser power, atoms are heated at twice the radial trap frequency, plotted for different laser powers in green (4.1 W) and orange (6.5 W). Data points are underlying data for the fitted green curve. For higher trapping powers a shift toward to larger frequencies and a broadening are observable. Exact temperatures can not be stated, because the used detection system is not calibrated. (b) Axial trap frequencies could well be observed by a direct oscillation of an atomic cloud, initially loaded at the trap edge. The solid line is fit to a regular damped harmonic oscillator.

Direct trap frequency measurements in radial direction based on dipole power variations were not successful, because oscillations in this direction were not observable. Furthermore, a relation between the center of mass position after a certain time of free evolution and velocities in the trap at different holding times could not be observed.

Direct axial trap frequency measurements were implemented by loading the dipole trap out of equilibrium. Placing the center of a small MOT at the edge of the dipole trap resulted in a well observable particle oscillation in the beam direction of the trap, as can be seen in Figure 3.17(b). Fitting the recorded data to the equation of a regular damped harmonic oscillator reveals a trap frequency of $\omega_z = 2\pi \times 8.95$ Hz.

3. Dipole Trap Loading

Temp. high power	45.1 μm
Temp. low power	43.9 μm
direct axial	44.9 μm

Table 3.2

Results for the dipole trap beam waist in the PRIMUS experiment calculated from measured trap frequencies.

Radial trap frequencies could well be determined by the temperature increasing method, as shown in Figure 3.17(a). The dots represent a measurement with 4.1 W of laser power while the green curve is a smoothing fit to the data. In orange, the same fit for a laser power of 6.5 W is plotted while underlying data is left out for clarity. Both data sets feature one relatively broad maximum. One can see a broadening towards increased laser powers caused by higher temperatures in the trap. For a power of 6.5 W one gets a radial trapping frequency of $\omega_r = 2\pi \times 906.5$ Hz and $\omega_r = 2\pi \times 760.5$ Hz for the reduced power. With trap lifetimes in the order of seconds it is impossible to determine axial trap frequencies with this technique, which are lying in the order of a few Hz.

Using Equation (3.19) and (3.9) the determination of trap frequencies delivers knowledge about the laser beam's radius and trap depth.

The calculated beam waists are displayed in Table 3.2 and agree well with each other. Inserting $w_0 = 45$ μm into Equation (3.17) gives a trap depth of $U_0 \approx 186$ μK for a laser power of 7 W. Both characterizing numbers are of importance for the evaporation described in Chapter 4.

4. Evaporation in a Dipole Trap

4.1. Evaporative Cooling

Evaporative cooling is the only possibility to reach ultra cold temperatures in the nK regime and below. It is based upon the removal of high energetic atoms, the same effect our body uses to cool down by sweating.

An atomic ensemble in thermal equilibrium will always form some kind of Maxwell-Boltzmann distribution as depicted in Figure 4.1. Energy between atoms is transferred via collisions, which leads to this characteristic curve. It describes few very slow atoms, the majority of them in a medium kinetic energy range and a few very energetic ones with no upper boundary. Strictly

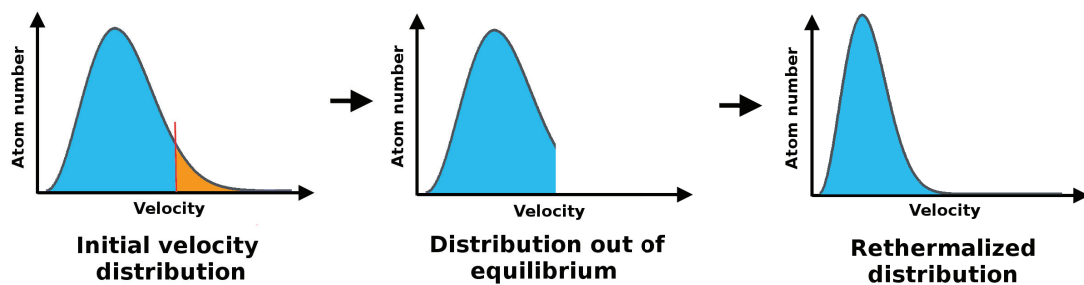


Figure 4.1

Temporal evolution of evaporative cooling. An initial Maxwell-Boltzmann distribution is truncated at a certain level, leaving an out of equilibrium distribution. By elastic collisions between atoms, the initial shape is recreated but due to the loss of kinetic energy it gets squeezed and the most probable velocity is shifted towards lower values.

speaking, temperatures are only defined in this equilibrium state and can be expressed in terms of atomic velocities. The most probable speed of a Maxwell-Boltzmann distribution is linked to temperature by $v_p = \sqrt{2k_B T/m}$ not to be confused with the average speed that is $\bar{v} = \sqrt{8k_B T/(\pi m)}$.

After the removal of atoms, the system comes back to equilibrium by particle collisions. If preferably high energetic particles were removed, the new equilibrium will be at a colder temperature, the effect of evaporative cooling.

In an optical dipole trap evaporation can occur naturally or forced. In natural evaporation the confining potential is left unchanged and "hot" atoms are able to leave the trap. The amount of evaporated atoms is large when temperature and trap depth are about the same size and

4. Evaporation in a Dipole Trap

decreases with time. The evaporation leads to lower temperatures, leads to a lower probability to scatter atoms in states that are kinetically high enough to leave the trap. In this way evaporation slows down exponentially. Nevertheless, there is always a certain probability to produce atoms carrying the required energy and there is no equilibrium state. In fact, it is in principle possible to gather the complete kinetic energy of the system in a single atom, leaving the ensemble at zero temperature behind.

Evaporation can be kept running at a certain rate by artificially lowering the confining potential, called forced evaporative cooling. It is reasonable to describe the trap depth U_0 in relation to the trapped atoms temperature T , giving

$$\eta = \frac{U_0}{k_B T} \quad (4.1)$$

where k_B is the Boltzmann constant. Effective evaporation is considered to appear with a constant value of η , where a high value results in a slow evaporation with little particle loss and a low number gives a fast but less effective evaporation.

Effectivity defined as

$$\gamma_{\text{eff}} = -\frac{\ln(\text{PSD}_f/\text{PSD}_i)}{\ln(N_f/N_i)} \quad (4.2)$$

is an appropriate value to compare different trap geometries and evaporation strategies. Here N describes the atom number where the indices f and i stand for final and initial respectively. The phase space density (PSD) is defined as

$$\text{PSD} = N \cdot \left(\frac{\hbar \bar{\omega}}{k_B T} \right)^3 \quad (4.3)$$

with $\bar{\omega}$ the mean trap frequency and describes effectively the number of atoms occupying the trap's ground state.

High efficiencies as one can see from Equation 4.2 rely on low atom loss numbers.

4.1.1. Collisions and Losses

In real systems, atoms are not only evaporated but could also be lost by collisions with background gases, hyperfine state changing collisions or density dependent losses, quantified in the ratio between "good" and "bad" collisions.

Good collisions are elastic ones, leading to rethermalization of the ensemble after atoms got evaporated. The faster an atomic cloud regains equilibrium, or comes close to it, the faster an effective evaporation can occur. The rate of evaporated atoms Γ_{Ev} is connected to the rate of elastic collisions (Ketterle and Druten 1996)

$$\Gamma_{El} = n \sigma \bar{v}_{rel} = 8\sqrt{2} \frac{N m a_s^2 \bar{\omega}^3}{k_B \pi T} \quad (4.4)$$

by

$$\Gamma_{Ev} = \Gamma_{El}\eta e^{-\eta}. \quad (4.5)$$

Here, n is the atomic density, $\bar{v}_{rel} = \sqrt{2} \cdot \bar{v} = 4\sqrt{k_B T / (m\pi)}$ describes the atoms relative mean velocity and $\sigma = 8\pi a_s^2$ the elastic collisional cross section where the s-wave scattering length a_s equals $98a_0$ (Egorov et al. 2013) for rubidium-87 making use of the Bohr radius a_0 .

Density independent loss rates and heating

Density independent effects are based on single (trapped) atom behavior and therefore are independent of density. The most dominate ones are undesired collisions between trapped atoms and free particles from residual background pressure that result in an immediate atom loss. Since the trap is operated in the Knudsen regime¹, atoms are supposed to escape without any further interaction with trapped atoms. A heating mechanism can be expected from the possibility of glancing collisions where only a small fraction of kinetic energy is transferred to the trapped atom (Cornell et al. 1999). Since residual gas mixtures slightly differ in every experimental setup and precise pressure measurements on the dipole trap's location are hardly available, this collision rate is best determined experimentally by a simple lifetime measurement. Another heating rate originates from absorbed dipole trap photons. Absorption and the following isotropic emission of a photon result in an energy transfer of $2E_{rec}$, twice the recoil energy (Grimm et al. 1999), defined as $E_{rec} = p_{photon} / (2m)$. Heating power can be written as

$$P = 2E_{rec}\Gamma_{sc} \quad (4.6)$$

with the photon scattering rate Γ_{sc} defined in Equation 3.12². The employed dipole trapping wavelength of approximately two micrometer is furthest possible away from any optical transition, without the need for special optics. Furthermore, the available laser powers in our compact setup are a lot smaller compared to other laboratory based experiments. For this reason it is save to say that this effect will not limit our performance.

Heating can also be introduced by technical noise like laser intensity or position fluctuations. Regarding a harmonic trap as a simple harmonic oscillator, intensity noise can be described as changes in the spring constant and lead to exponential heating (Savard et al. 1997; M. E. Gehm et al. 1998), the heating rate depends on the ensembles temperature. In contrast position fluctuations, caused by laser pointing instabilities result in a constant heating rate, so without any temperature dependence. Both effects can also be distinguished by their dependency on trap frequencies. While intensity noise scales with $\propto \bar{\omega}^2$, it scales with $\propto \bar{\omega}^4$ for pointing fluctuations.

¹The mean free path is larger than the size of the trap

²While the heating rate in red detuned dipole traps is independent of the ensembles temperature it scales linearly with it in blue detuned dipole traps (Schulz 2002)

4. Evaporation in a Dipole Trap

Density dependent lossrates

Hyperfine state changing collisions (also known as dipolar relaxation) can appear when rubidium atoms in the upper ground state $|F=2\rangle$ are present in the ensemble (Weiner et al. 1999). Within a collision these can change to the lower ground state, while the energetic difference is converted into kinetic energy. This is generally enough to expel both collisional partners from the trap³. A simple method to overcome this problem is to transfer all atoms into the lowest ground state during the dipole trap loading stage, by simply shutting off the repumping light a few ms before the cooling light. On one hand, atoms can theoretically be lifted into the upper ground state by dipole trap photon absorption, but this effect scales with $1/\Delta^4$ (Cline et al. 1994) making it negligible for our trapping frequency. On the other it can be dramatically enhanced by multimode lasers (Lauber et al. 2011). Mode spacings in the range of hyperfine splittings induce two-photon Raman transitions, lifting atoms in higher internal states. If this effect becomes dominant, a cloud of atoms that is initially trapped in the lowest ground state, will suffer from high loss rates. In this regime, improved lifetimes can be observed by the preparation of atoms in a single stretched Zeeman sublevel, e.g. $|F=2, m_F=2\rangle$. In such a state, hyperfine changing collisions are suppressed due to the conservation of the total angular momentum (W. Hung et al. 2015).

Three-body recombination, or dimerization, describes the interaction of three atoms, where two of them form a molecule. Both, molecule and single atom, gain a kinetic energy on the order of Kelvin, resulting in a subsequent loss of three atoms (Härter et al. 2013). The process relies on atomic properties and atomic density in the trap. Even though it was just lately understood in depth (Wolf et al. 2017), important for this experiment is only the rate of atom loss defined as

$$\Gamma_{3B} = \frac{L_{3B} n_0^2}{3\sqrt{3}}. \quad (4.7)$$

Here n_0^2 describes the peak density of the atomic ensemble while L_{3B} is the rate coefficient for three-body recombination events. For rubidium in the $|F=1\rangle$ ground state it was determined to be $4.3 \pm 1.8 \times 10^{-29} \text{ cm}^6/\text{s}$ (Burt et al. 1997), for non condensed atoms. For condensed atoms this value drops due to coherent behavior in the condensate, which suppresses collisions. In case of an atom preparation in the $|F=2, m_F=2\rangle$ state it drops to $1.8 \pm 0.5 \times 10^{-29} \text{ cm}^6/\text{s}$ (Söding et al. 1999) for condensed atoms and has not been published for thermal atoms. As an estimation one could start with the theoretical approach of Kagan *et al.* giving a factor of six between condensed and thermal atoms calculated for ideal gases (Kagan et al. 1985). This results in an L_{3B} coefficient for non condensed rubidium in the stretched $|F=2, m_F=2\rangle$ state of $\approx 1.1 \times 10^{-28} \text{ cm}^6/\text{s}$.

Loss rates alone can't provide information about the effectiveness of an evaporation process. Therefore, they must be linked to the rethermalisation time. In a system with high elastic collision rates, loss mechanisms are more likely to be tolerated, as the overall process proceeds faster. The afore mentioned ratio between "good" and "bad" collisions translates to the ratio of

³For rubidium the transferred energy is equal to a temperature of 300 mK.

elastic to inelastic ones

$$R(T, n) = \frac{\Gamma_{El}}{\Gamma_{Inel}} = \frac{\Gamma_{El}}{\Gamma_{1B} + \Gamma_{2B} + \Gamma_{3B}} \quad (4.8)$$

$R(T, n)$ can also be understood as the number of collisions an atom undergoes in the trap before it is lost. A guideline for sufficient evaporation to reach quantum degeneracy is a value of 500, calculated for a starting PSD of 10^{-6} (Ketterle and Druten 1996). A more precise minimal number can be calculated by (Maic Zaiser 2010)

$$R_{min} = \frac{\sqrt{2}e^\eta}{(\alpha_{ev} - 1)\eta}, \quad \text{with} \quad \alpha_{ev} = \frac{\dot{T}/T}{\dot{N}/N} \quad (4.9)$$

4.1.2. Lifetime Measurements

Concluding the above mentioned atom loss mechanisms into the three categories of one-, two-, and three-body losses, the atom number evolution can be described by

$$\frac{dN}{dt} = -\alpha N - \beta N^2 - \gamma N^3 \quad (4.10)$$

with the one-, two- and three-body loss coefficients α , β and γ respectively. Disregarding the three-body losses from this formula, justified by much smaller loss coefficients compared to both others, one can derive

$$N(t) = \frac{N_0\alpha}{(\alpha + N_0\beta)e^{\alpha t} - N_0\beta}. \quad (4.11)$$

For a lifetime measurement, as depicted in Figure 4.2(a), the dipole trap is loaded with the standard molasses procedure and held at a certain optical power while recording the number of trapped atoms.

For holding times above two seconds the atom number evolution can well be described by a single exponential function $A \cdot e^{-\frac{t}{\tau_{1B}}}$, indicating a pure density independent loss mechanism. While the lifetime of a trapped ensemble in some cases is defined as the time where the fraction of remaining atoms reaches $1/e$ of the initial value (Nes 2008; Song et al. 2018), in most cases the term refers to the exponent of an exponential decay τ_{1B} (Grimm et al. 1999), an easily comparable quantity. The measurement in Figure 4.2 reveals a lifetime of 4.3 ± 0.2 s. This value is rather low since most experiments observe lifetimes of a few tens of seconds. Up to 300 s where demonstrated for fermionic Lithium at a vacuum pressure of 1.3×10^{-11} mbar (O'Hara, Granada, et al. 1999b).

In the current setup, the pressure is monitored by the ion getter pump of our pumping section described in Chapter 2. The displayed value of $>1 \times 10^{-11}$ mbar and measured lifetimes are in conflict with other values found in the literature. To exclude other one-body loss mechanisms as leading contribution our vacuum was intendedly worsened, while taking lifetime measurements. The result can be seen in Figure 4.2(b), revealing an undeniable pressure dependency for our lifetime. While the exact values can be found in Table 4.1 it should be mentioned that this value

4. Evaporation in a Dipole Trap

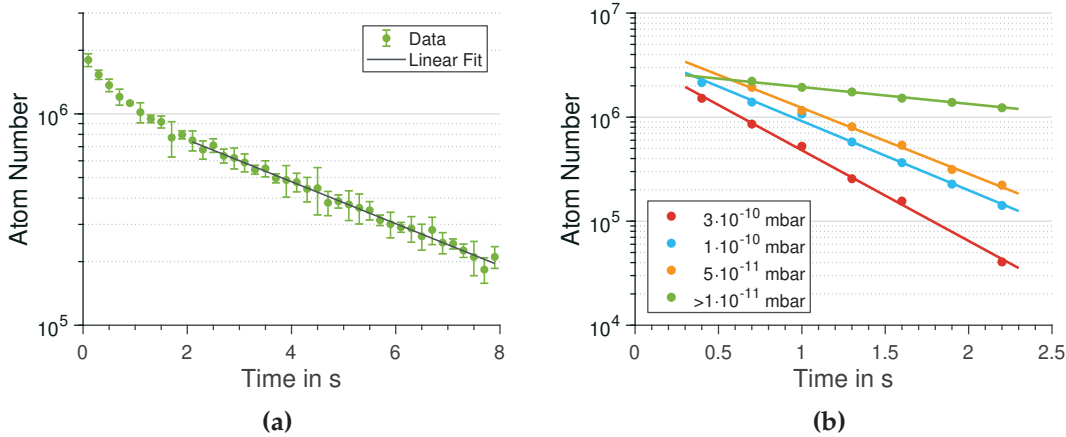


Figure 4.2

Dipole trap lifetime measurement. (a) For times larger than two seconds a pure exponential decay is observable, indicating density independent one-body loss mechanisms. (b) Lifetime measurements for different background pressures in the vacuum chamber. Lifetimes are strongly pressure dependent. Thus background gas collisions are identified as the leading atom loss contribution.

changed over the years. After the first assembly, the vacuum system had to be opened four times which results in varying lifetime value. The highest measured values have always been around 5 s, for every reassembly.

Pressure	Lifetime
3×10^{-10} mbar	0.50 ± 0.03 s
1×10^{-10} mbar	0.65 ± 0.05 s
5×10^{-11} mbar	0.68 ± 0.03 s
$>1 \times 10^{-11}$ mbar	2.68 ± 0.18 s

Table 4.1

Determined one-body loss lifetimes for different vacuum qualities. The last value is lower than the one from Figure 4.2(a) since the system did not fully recover.

Within the first second of holding time, atom losses are dominated by a different mechanism, indicated by the deviation from a straight line in the semi logarithmic plot of Figure 4.2(a). Fitting Equation 4.11 does not give satisfying results as it is shown in Figure 4.3. Fitting with free parameters N_0 , α and β (blue line) result in a precise description for the curves beginning but does not agree for long holding times. Anyway the fitted β value of a few times 10^{-7} agrees with other experiments (Nes 2008). Predetermining the lifetime and fitting the data with only two free parameters (red line) results in an improper representation in the short time regime. For this reason, atom losses for short holding times can not only be attributed to two-body losses.

Further investigating the loss behavior for short holding times reveal a dramatic temperature

decrease within the first second that continues over the whole measurable time. Dipole trap measurement are restricted to times >30 ms caused by the large amount of non transferred molasses atoms overlaying the trapped ones. For this reason, the data in Figure 4.4 was recorded by holding the dipole trap at approximately 8 W for 40 ms followed by an abrupt decrease to 6.5 W. This procedure leaves a situation where the ratio η between trap depth and ensemble temperature is relatively high, close to the situation of a recently loaded dipole trap.

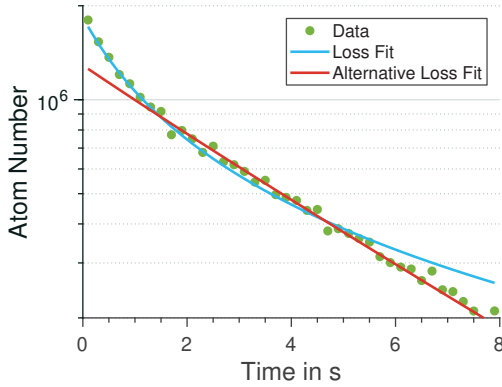


Figure 4.3

Lifetime measurement fitted to equation 4.11. It is not possible to get good agreement for the whole measurement. While the blue line with three free parameters agrees well with short time behavior it deviates from long time evolution. Using only two free parameters gives oppositional results as depicted by the red line.

power reduction. If density dependent loss is not prominent directly after the loading of a dipole trap in can enter in two further positions. Natural evaporation does not only decrease the ensembles temperature but can also increase its density if other loss mechanisms do not counteract this evolution. For this reason there is a possible third region in lifetime measurements in between the natural evaporation dominated and the density independent loss dominated region (Bourouis 2007). Most probably due to the low value of τ_{1B} it could not clearly be identified in this measurements.

Keeping in mind the overall target of the project to perform atom interferometry, a cold and dense sample of atoms is needed as its source. Therefore, density dependent loss mechanisms will play a major role towards the end of evaporation and can not be neglected for the whole procedure, even though they do not contribute in the beginning.

A high η value leads to increased natural evaporation, described by an exponential function. The overall atom loss behavior can be written as the sum of two exponentials

$$N(t) = C_1 e^{-\frac{t}{\tau_{nev}}} + C_2 e^{-\frac{t}{\tau_{1B}}} \quad (4.12)$$

defining two different lifetimes for natural evaporation and one-body losses, the inverses of their respective loss coefficients. This model agrees well with all recorded lifetime measurements in this experiment and was for example applied in Figure 4.4(b) that is log-log-plotted for visibility of conformity in both regimes.

As a test for power dependent loss mechanisms the same measurement was performed at a lower laser power of 3 W. In this case τ_{nev} drops from 0.61 ± 0.12 s to 0.41 ± 0.09 s attributed to a higher η value for the increased

4. Evaporation in a Dipole Trap

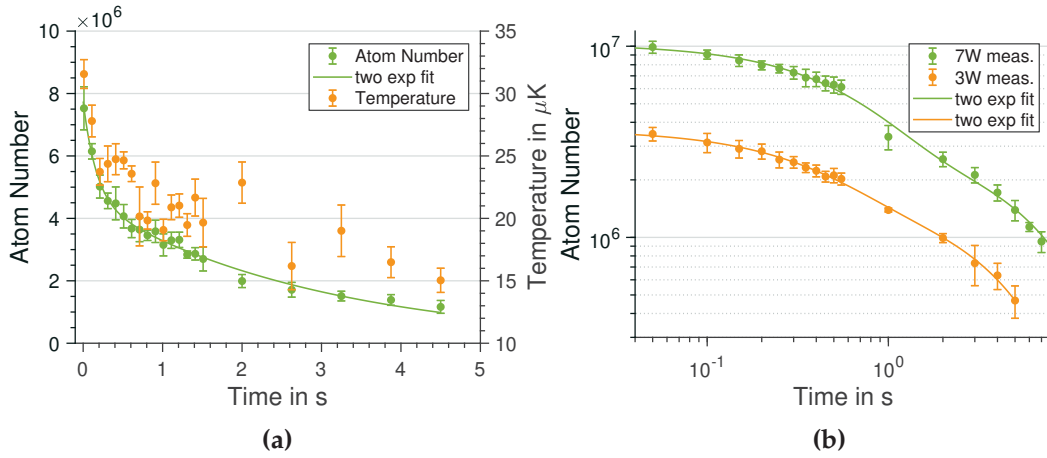


Figure 4.4

(a) Number of trapped atoms and their temperature in a lifetime measurement showing a link between both indicating the loss mechanism to be natural evaporation. While temperature decreases fastest in the beginning of the measurement it continues though all of it. (b) Log-log-plot for the atom number evolution for two different holding FORT powers. The precise description of both regimes with double exponential fit becomes clear while no significant dependencies on laser power are present.

4.2. Simulation techniques overview

Several methods to model the process of evaporative cooling in cold atomic systems were developed. In this section the most important ones will be described and their applicability, according to the needs of this thesis, namely a precise prediction of temperature and atom number dependencies for several trap geometries and very fast evaporation, will be discussed. Most of the presented theories originate from the year 1996, one year after the first realization of a BEC where evaporative cooling was mandatory but not entirely understood.

4.2.1. Doyle's method

The method developed by John M. Doyle (Doyle 1991) is based on the principles of conservation of atom number and energy. A single temperature is assumed to describe the atomic ensemble. Its basis is the observation of: how many particles leave the trap and how much energy every single one carries away. Furthermore included are losses due to collisions, adiabatic work acting on the atoms and dipolar decay collisions. The last one plays no role in alkali metal experiments as it is described in this thesis and can be neglected. Not included is the process of atom spilling. Spilled atoms are not expelled from the trap because of collisions, but a lowering of the trapping potential. Therefore, a spilled atom always removes exactly the minimal possible energy to leave the trap. This process has a cooling effect on the ensemble, but it is less effective than evaporation. The importance of this spilling increases with short evaporation times as they are used in this experiment.

According to these remarks, the equation reads:

$$\frac{d}{dt}(N\bar{E}) = \dot{N}_{ev}\bar{E}_{ev} + N\bar{E}\dot{\alpha}_{ch} \quad (4.13)$$

where N is the atom number, E describes energy, the index ev indicates evaporated atoms or energy and α_{ch} is the relative change in atom cloud energy due to changes in the trap volume:

$$V_{\text{eff}} = N/n_0 \quad (4.14)$$

with n_0 the clouds peak density. This volume has to be calculated. An easy approach is based on scaling laws introduced in Section 4.2.5. The number of atoms leaving the trap is determined by a numerical calculation of collisions inside the trap volume. For magnetic and deep enough ($\eta > 4$) traps, Doyle found an equation giving the fraction of collisions leading to an atom escaping the trap to the ones where the atom stays. For shallow traps DeCarvalho et al. extended this method, but their solution only applies to a linear spherical trap, different from a dipole trap (DeCarvalho et al. 2004).

This method is computationally easy and fast but needs a lot of effort for every new trap geometry. Therefore it is not suitable for the PRIMUS experiment.

4.2.2. Discrete evaporation steps

The method of discrete evaporation steps is a pure analytical one. After every evaporation step, it assumes the atoms to rethermalize which keeps them in the state of thermal equilibrium at all times (K. B. Davis, Mewes, and Ketterle 1995). An evaporation step is described by cutting off the high temperature tail of the sample's Boltzmann distribution. This leads to mathematically exact solutions and played an important role for the understanding of evaporative cooling in the past but does not fit the conditions for drop tower operation with its short evaporation times. Giving a precise forecast for the behavior of cooled atomic ensembles under given conditions is not this theory's strength.

4.2.3. Trajectory simulation

A method based on atomic trajectories was introduced by M. Holland et al. (Holland et al. 1996). Its approach is very similar to the later introduced DSMC (direct simulation Monte Carlo) method (see Section 4.2.6). The evaporative behavior of the overall atomic system is broken down into trajectories of single atoms. Time and energy are being discretized where time steps have to be smaller than the atoms' mean free time.

The procedure goes as follows: A single atom with discrete energy is picked from the sample and a Monte Carlo like method determines the amount of collisions in that time. In every single collision the atoms' energy is changed according to the Monte Carlo logic and finally discretized again. Doing so with a large number of atoms leads to a realistic determination of evaporative cooling.

4. Evaporation in a Dipole Trap

To my knowledge, there are no new results published with this simulation technique. A high computational effort with less direct information than the DSMC method makes it unfavorable.

4.2.4. Truncated Boltzmann distribution

Mathematical descriptions of evaporative cooling are often based on a truncation of the Boltzmann distribution. This obvious approach was already applied in 1991 (Doyle 1991), the proof of its validation was published five years later in 1996 (Luiten et al. 1996). The significant difference in this theory, compared to the introduced method of discrete evaporation steps (Section 4.2.2), is the absence of rethermalization in every evaporation step.

An important foundation in the description is that the distribution of atoms in phase space only relies on their energy. Furthermore, it is assumed that all atoms with kinetic energies higher than the trap depth are leaving the trap without further collisions with other atoms. The theory is limited to temperatures well above the lowest trap level energies because of its pure classical nature.

According to these assumptions an equation for the atoms' phase space distribution is deduced and the truncated Boltzmann distribution is inserted. The resulting equation is solved numerically. For the change in atom number one gets:

$$\dot{N}_{ev} = n_0^2 \sigma \bar{v} e^{-\eta_t} V_{ev} \quad (4.15)$$

with n_0 a reference density which in thermal equilibrium matches the peak atomic density and σ the atoms' cross section. $\eta_t = \epsilon_t/kT$ describes the trap depth, $\bar{v} = \sqrt{(8kT/\pi m)}$ the average atomic velocity and V_{ev} the effective trap volume in which collisions occur

$$V_{ev} = \frac{\lambda_{dB}^3}{k_B T} \int_0^{\epsilon_t} d\epsilon \rho(\epsilon) [(\epsilon_t - \epsilon - k_B T) e^{-\epsilon/k_B T} + k_B T e^{-\eta_t}]. \quad (4.16)$$

Here λ_{dB} is the de Broglie wavelength, ϵ the particles energy and ϵ_t the cut off energy of the Boltzmann distribution. The ensemble energy changes according to:

$$\dot{E}_{ev} = \dot{N}_e \left(\epsilon_t + \frac{W_{ev}}{V_{ev}} k_B T \right) \quad (4.17)$$

where $W_{ev} = V_{ev} - X_{ev}$ with

$$X_{ev} = \frac{\lambda_{dB}^3}{k_B T} \int_0^{\epsilon_t} d\epsilon \rho(\epsilon) [k_B T e^{-\epsilon/k_B T} - (\epsilon_t - \epsilon + k_B T) + e^{-\eta_t}] \quad (4.18)$$

describing the volume in which atoms are no longer trapped.

These unhandy equations describe the general case for all possible trap configurations. Applying them to a specific case results in a drastic simplification. Based on these approaches evaporation in a three dimensional harmonic trap, a situation close to the one in a dipole trap, can be described by the following equations (Olson et al. 2013):

$$\dot{N} = \dot{N}_{ev} + \dot{N}_\theta + \dot{N}_{1B} + \dot{N}_{3B} \quad (4.19)$$

$$= -(\Gamma_{Ev} + \Gamma_{1B} + \Gamma_{3B})N - N_{spilled} \quad (4.20)$$

$$\dot{E} = \dot{E}_{ev} + \dot{E}_\theta + \dot{E}_{1B} + \dot{E}_{3B} \quad (4.21)$$

$$= -N\Gamma_{Ev}(\eta + \kappa)k_B T + 3Nk_B T \frac{\dot{\omega}}{\omega} - E_{spilled} - \Gamma_{1B}E - \Gamma_{3B}\frac{2}{3}E \quad (4.22)$$

Γ_{Ev} , Γ_{1B} and Γ_{3B} describes the collision rates for collisions leading to evaporation of atoms, density independent and three body collisions respectively. The process of losing atoms due to changes in the trap geometry, indicated by \dot{N}_θ is called spilling. It can not simply be reduced to a single rate but has to take temperature, atom number and actual trap changes into account.

The first term on the right hand side of Equation 4.22 describes loss of energy due to evaporated atoms, while $(\eta + \kappa)k_B T$ is the average energy carried away by a single atom. The second term describes work, acting on the atoms by changing the trap's shape. The third term includes the energy carried away by spilled atoms. The last terms' delineate energy loss is caused by density independent and three body losses respectively.

On one hand, expressing the evaporation based on a truncated Boltzmann distribution is computationally relatively simple, on the other hand, this method is limited to harmonic traps and can only be applied for high trap depth ($\eta > 4$). Within this thesis it will be used for optimization calculations and basic understanding of evaporative effects. The simulation is written in a Matlab program that will be called *Trunc Sim* in the following.

4.2.5. Scaling laws

Investigating dependencies between important dipole trap characteristics, one can find scaling laws, describing the ensembles' evolution for a time dependent trapping potential (O'Hara, M. Gehm, et al. 2001). In this theory atom losses due to background gas collisions are neglected and only energy changes caused by evaporated atoms and trap shape changes are taken into account. Every evaporated atom carries an energy $E_{Ev \text{ Atom}} = U_0 + \alpha_+ k_B T$ where α_+ is a value between zero and one, described for harmonically approximable potentials as

$$\alpha_+ = \frac{\eta - 5}{\eta - 4}. \quad (4.23)$$

Another basis for these scaling laws is an evaporation with constant η . This requirement is experimentally not always easy to fulfill and excludes fast evaporation schemes from the calculation. In this theory the initial trap depth $U_0(0)$ atom number $N(t)$, phase space density

4. Evaporation in a Dipole Trap

$PSD(t)$ and elastic collision rate $\Gamma_{El}(t)$ evolve as

$$\frac{N(t)}{N(0)} = \left(\frac{U_0(t)}{U_0(0)} \right)^{3/[2(\eta'-3)]}, \quad (4.24)$$

$$\frac{PSD(t)}{PSD(0)} = \left(\frac{U_0(0)}{U_0(t)} \right)^{3(\eta'-4)/[2(\eta'-3)]} \quad (4.25)$$

and

$$\frac{\Gamma_{El}(t)}{\Gamma_{El}(0)} = \left(\frac{U_0(t)}{U_0(0)} \right)^{\eta'/[2(\eta'-3)]} \quad (4.26)$$

respectively, using $\eta' = \eta + (\eta - 5)/(\eta - 4)$. A constant η restraints the trapping potential depth to follow

$$\frac{U_0(t)}{U_0(0)} = \left(1 + \frac{t}{\tau} \right)^{-2(\eta'-3)/\eta'}, \quad \text{with} \quad \frac{1}{\tau} = \frac{2}{3}\eta'(\eta - 4) \exp(-\eta)\Gamma_{El}(0). \quad (4.27)$$

Scaling laws are the most simple method explained in this chapter. They will be used to find discrepancies between measured data and simple theoretical explanations giving hints for more complex mechanisms in the actual experiment.

4.2.6. Discrete Simulation Monte Carlo (DSMC)

The Discrete Simulation Monte Carlo (DSMC) technique, was first applied to cold atomic samples by H. Wu in 1996 (Wu and Foot 1996). Originally this approach was developed by G. A. Bird (Bird 1994) and is commonly used in the fluid dynamics community. It has a wide range of application going from space science to avalanche simulations.

The requirement of a high Knudsen number, meaning the particles' mean free path has to be long compared to a length scale of the investigated system, is valid for dilute gases as they are used in this experiment.

The method's basic idea is to separate atomic movement from collisions. In every time step the atomic movement is calculated first, followed by a second step which tackles collisions between atoms. Every atom gets a position (r_x, r_y, r_z) and a velocity (v_x, v_y, v_z) assigned that are evolved in time. While the DSMC method is computationally intensive, proportional to the calculated atom number, it comes with a high flexibility in potential geometries, making it interesting for this thesis. In contrast to methods based on analytical approaches, even the simulation of anharmonic traps is not a problem. Furthermore, non ergodic problems can be tackled, meaning systems where atomic positions in phase space do not only depend on their energy. Situations like this occur, when the evaporation is low dimensional. In this case the evaporation of an atom further depends on the direction of its velocity.

A strictly classical approach like this limits meaningful simulations to temperatures high, compared to quantum degeneracy. By altering the probability for bosons to be scattered in

particular states, bosons prefer states already occupied by other bosons, the DSMC method could also be extended to the quantum regime (Wu, Arimondo, et al. 1997).

The DSMC method turned out to be the most versatile of all introduced approaches. For this reason it will be used in this thesis to compare different trap geometries and investigate differences between evaporation with and without the effect of gravity. A precise description of the developed code can be found in the next section.

4.3. Implementation of the DSMC Method

The DSMC code is written in Python 3.6 (Python Software Foundation 2018) and makes use of the NumPy (NumPy 2018; Travis 2006) package providing matrix structures and calculations. As mentioned above, the basic concept is to separate atomic movement from collisions. In this manner every time step includes a movement and a collision phase.

Movement:

Atoms are starting with an initial velocity and position. Velocity changes result from potential gradients and collisions, with only the first one contributing in this step. Positions are then determined, based on velocity and time passed per step.

While there are lots of possibilities, in this thesis atomic movement is described by a second-order symplectic integrator, leading to a long time stability in energy conservation and phase space volume (Donnelly et al. 2005).

Every evolution step is calculated in three sub-steps:

$$\tilde{r}_i = r_i(t) + \frac{1}{2}\Delta t v_i(t) \quad (4.28)$$

$$v_i(t + \Delta t) = v_i(t) - \frac{1}{m}\Delta t \nabla V(\tilde{r}_i) \quad (4.29)$$

$$r_i(t + \Delta t) = \tilde{r}_i + \frac{1}{2}\Delta t v_i(t + \Delta t) \quad (4.30)$$

Here the new particle velocity is determined at the position where the atom covered half the distance it would have, with the velocity from the last iteration. The second half of movement is governed by the new velocity. Time steps Δt have to be chosen in a way that they are small compared to the particles mean free path and their covered distance must be small compared to the changes in potential. The driving potential can be chosen arbitrarily but will in most cases be based on a dipole potential as described in Section 3.2. With all atomic positions determined, they are, in a next step, ordered into a three dimensional grid, with numbered cells in preparation for the collision stage. Atoms moving off the predefined grid are considered to be evaporated and their data is stored into a binary text file for further investigation.

Collision:

Collisions are only calculated in areas of low potential where the highest atomic density is assumed to be. To lower the computational effort a cut off parameter can be introduced. It

4. Evaporation in a Dipole Trap

determines up to which fraction of potential depth collisions will be considered. Furthermore at least two atoms have to be in a cell to trigger a collision.

N particles allow for $N \cdot (N - 1)$ possible encounters. Checking all of them requires a huge computational effort. To overcome this problem, G. Bird developed the *No Time Counter* (NTC) procedure (Bird 2007) based on a collisional probability. It is equal to the ratio of the volume covered by an atoms' collisional cross section multiplied by its velocity, to the volume of the cell. In fact the maximum collisional probability is determined by finding the maximum relative speed between a pair of atoms in every particular cell.

$$P_{Max} = \frac{M\sigma v_{rmax}\Delta t}{V_c} \quad (4.31)$$

Here σ is the atoms collisional cross section, v_{rmax} is the maximum relative velocity and V_c the volume of a cell. M is a multiplier arising from the idea of super atoms in the code, where every particle represents several atoms. If the particle number drops below a predefined value, superatoms are split with opposite velocities, resulting in a relatively constant particle number in the calculation. Superatoms were introduced into the code since the computational effort rises linearly with particle number. Choosing an appropriate amount of superatoms results in dependable, but accelerated, simulations.

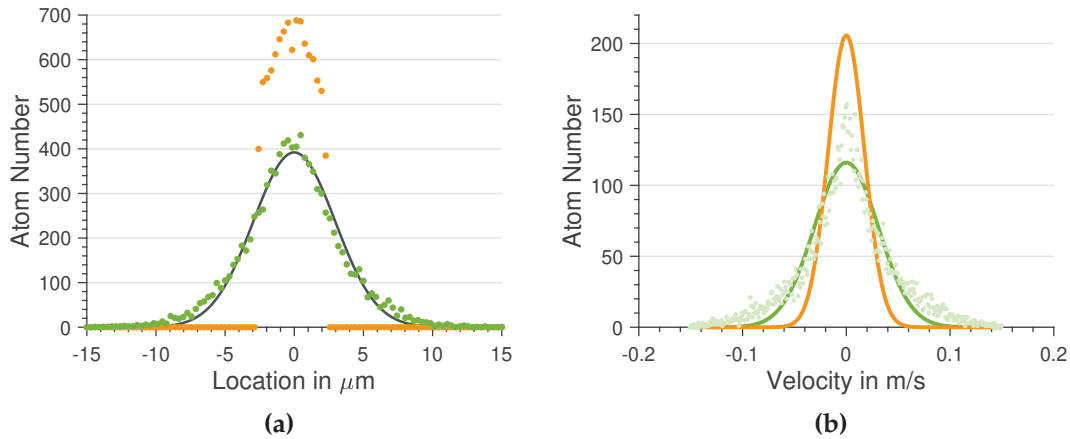
The number of pairs colliding inside a cell in one time step is calculated by multiplying Eq (4.31) with $N(N - 1)/2$. Relatively low velocities for cold atoms, small time steps and volume cells lead to collisional probabilities lower than 1, thus no collisions occur at all. For this reason the value of the chosen pair is stored for every cell and added up in every new iteration. When it reaches one, a pair of atoms is randomly picked and a collision happens if the ratio its velocity to the maximum value in the particular cell is higher than a random number between zero and one.

$$\frac{v_{rij}}{v_{rmax}} > Rand \quad (4.32)$$

In case of an encounter the collisions are considered to be elastic. New velocities are determined, based on a Marsaglia algorithm (Marsaglia et al. 1964), also known as the polar method. Random directions and velocities for both atoms are calculated with respect to their initial total energy.

Initial atom distribution:

The initial starting conditions are calculated in a separate Python program. Setting the desired superatom number, an initial dipole trap and the ensemble's temperature, it calculates an equivalent discrete Boltzmann distribution. The amount of atoms per quantized energy is the basis for the next step, modeling the spatial distribution of the atoms. Every single atom is randomly placed in the area under investigation and the potential energy in this spot is determined. If the potential energy is lower than the atoms' kinetic energy, it is placed there with a velocity carrying the residual kinetic energy in an arbitrary direction. If the kinetic energy is lower, another randomly picked spot in space runs through the same procedure until an appropriate position for every atom is found. Having done so, lots of kinetic energy has been transferred to potential one. This problem is overcome by dividing the desired temperature

**Figure 4.5**

(a) Shown is the atom distribution determined as starting conditions. The positioning values in the orange plot were chosen too small which results in a narrow distribution with cut wings. Plotted in green is a distribution with well chosen parameters. The fitted curve is a Gaussian with a coefficient of determination of 98 %. (b) Velocity distribution calculated as initial conditions for the calculation. The orange curve is a fit to the, not shown, velocity distribution after placing atoms into the potential resulting in a lower temperature than desired. Green data results from a correction.

by the current one and multiplying every atom's velocity with the square root of this factor. The result is an atom distribution, carrying the right amount of energy while being close to equilibrium which is saved in a text file. How close the determined distribution comes to an equilibrium is strongly influenced by the position searching parameters. Setting them high, searching in a large area, results in long calculation times due to a high position decline. A low value gives rise to an imbalanced distribution as one can see in Figure 4.5

The entire code:

Before the start of any simulation the initial parameters have to be determined. This includes e.g. the number of cells, the desired time step length and amount, the area under investigation and the number of atoms, respectively superatoms. After loading the initial atom distribution and setting the evolution of the dipole trap laser power, the iterative process starts with the first movement step followed by a collision step. Afterwards the density independent atom loss is calculated. Based on a constant loss rate, a certain number of atoms is randomly picked and excluded from the simulation. Knowing the overall particle loss in this time step the superatom multiplier is reduced if necessary. Every i^{th} time step, where i is a natural predefined number, atom positions are plotted and the relevant data for the evaporation is stored in a binary text file.

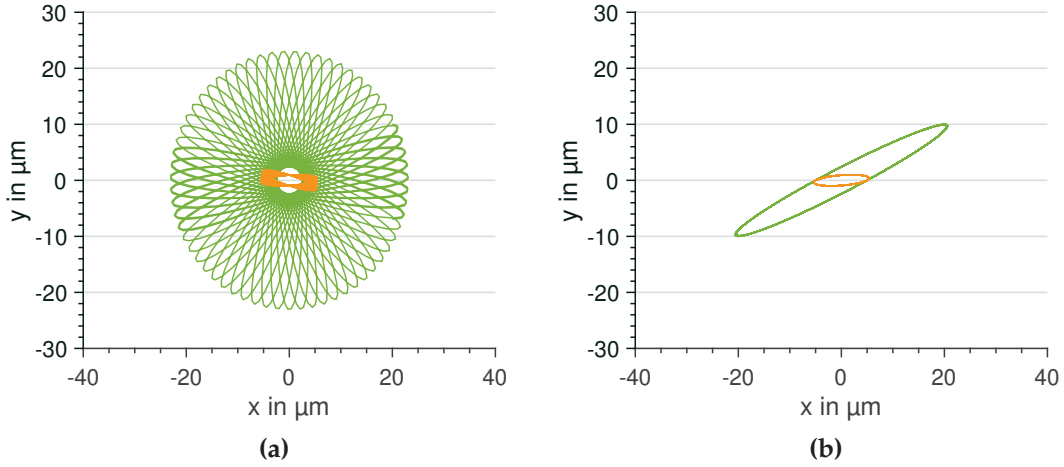
4.4. Dimension of Evaporation

Gravitation effects the atomic ensembles in a dipole trap in three ways. First of all, the clouds center of mass is shifted, compared to a cloud in an undisturbed potential. The shift, called gravitational sag, does not influence the evaporation process directly but might become important in the case of sympathetic cooling. For sympathetic cooling, one species of atoms is cooled by bringing it in physical contact with another, colder, atomic species. It is applied when cooling techniques are easily implementable for only one species of a mixture. Cooling rubidium for example is less demanding than cooling potassium (Landini, S. Roy, Carcagní, et al. 2011). For optical cooling techniques, this is true because of a larger splitting of hyperfine states, makes the transitions in rubidium easier addressable. Furthermore, the evaporative cooling process of potassium-39 suffers from a Ramsauer-Townsend reduction of the collision rate (Landini, S. Roy, Roati, et al. 2012), making it ineffective. Since the gravitational sag depends on the atomic mass and its polarizability, it is different for every atomic species. This reduces the spatial overlap of trapped clouds, making sympathetic cooling ineffective or even impossible. For this reason sympathetic cooling in microgravity is expected to be more efficient than on ground.

The second effect is a lowered effective trap depth. Overlaying the dipole trap potential with a gradient in one direction lowers the potential barrier in this direction as visualized in Figure 3.6. Trap depth is an important quantity in the evaporation process defining which atoms leave the trap.

The third effect is referred to as the dimension of evaporation. In a tilted potential the effective trap depths aren't equal for every direction. Atoms carrying high enough energies to evaporate along gravity are not able to do so in a perpendicular direction. The rare collision events producing highly kinetic atoms additionally have to produce them in the right direction to trigger evaporation. This reduced rate of evaporation effectively lowers the efficiency of evaporation since the loss mechanisms are identical in both configurations (Ketterle and Druten 1996; Surkov et al. 1996). If the evaporation requirement is based on the total kinetic energy of an atom, the situation is called three-dimensional evaporation (3DE). If it depends on the kinetic energy in one direction it is referred to as one-dimensional evaporation (1DE).

A clear distinction between both cases is only possible if the potentials in different directions are completely separable, which is the case for a perfectly harmonic potential. A dipole trap potential is only approximated as harmonic in the center of the trap but atoms close to evaporation experience a strong anharmonicity at the trap's edges. The resulting behavior is shown in Figure 4.6(a). While an atom with low kinetic energy just slowly changes direction (orange curve), a fast atom can easily exchange kinetic energy between different directions. Since this conversion takes some time, there is a certain probability for the atom to experience another collision where it gets slowed down again. Thus the dimension of evaporation D_{Ev} in a tilted trap is determined by the ratio of mixing rate to the rate of elastic collisions. Obviously there are not only the cases of definite one-, two-, or three-dimensional evaporation but all

**Figure 4.6**

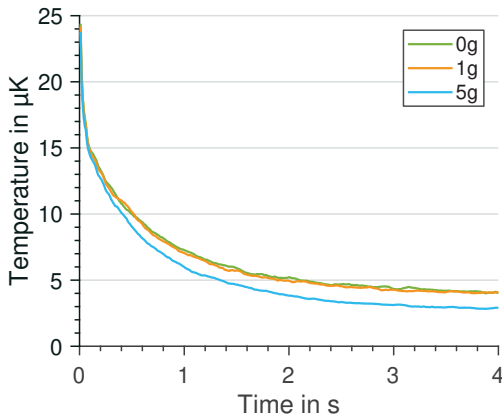
Atomic motion in the x - y plane of a dipole trap (a) and a harmonic potential (b). (a) High energetic atoms transfer kinetic energy from one direction to another due to the anharmonicity of the potential (green line). This effect is reduced toward the center of the trap where the potential can well be described by a harmonic one. (b) In a perfectly harmonic potential the direction of kinetic energy is restored.

values in between can appear as well, depending on the potential mixing character of a trap. The mixing rate depends on the potential gradient and can not easily be averaged to a single scalar quantity. Experimentally accessible is the dimension of evaporation via the average energy carried away by an evaporated atom $\bar{E}_{\text{ev,atom}} = (\eta + \kappa)k_B T$ (Ketterle and Druten 1996), which can be read as the kinetic energy to compensate the potential energy of the trap ($\eta k_B T$) plus an additional kinetic energy ($\kappa k_B T$). κ depends on the truncation parameter and the dimension of evaporation. It can be determined by the effectivity of evaporation γ_{eff} (Equation (4.2)) with the relation

$$\gamma_{\text{eff}} = \frac{\eta + \kappa}{3} - 1 \quad (4.33)$$

for an harmonic trap if atom losses are negligible, which is not the case in our setup. Furthermore, spilling events are not considered in Equation (4.33) and would falsify the determination.

To investigate the differences in evaporation with and without gravity, for our specific experimental setup, a DSMC calculation is

**Figure 4.7**

DSMC simulation evaporation from an optical potential with different gravitational accelerations.

4. Evaporation in a Dipole Trap

executed. Its results can be found in Figure 4.7⁴. The calculated temperature evolution for an evaporation procedure that has similarly been applied to the experiment in a dropping (Section 4.6), shows an insignificant deviation between a laboratory and a microgravity environment. In this particular simulation one-body losses were ignored.

These findings agree well with other experiments. Three-dimensional evaporation could also be observed in magnetically tilted dipole traps, where evaporation in one direction is strongly enhanced (C. L. Hung et al. 2008). We can conclude that the anharmonicity in an optical dipole trap forbids a distinct reduction of the dimension of evaporation.

The determined evaporation efficiencies of $\gamma_{\text{eff},0g} = 3.3$ and $\gamma_{\text{eff},1g} = 3.2$ are rather low for a calculation without one- and two-body loss processes⁵, giving evidence for a high number of spilled atoms. The reduced temperature for an increased gravitational force is attributed to the resulting lower trap depth.

Particularly in the context of high effort in doing experiments with cold atoms in microgravity on atom chips, it should be mentioned that these thoughts are also true for radio frequency evaporation in magnetic traps. Atoms in magnetic traps are not symmetrically distributed around the trap center but displaced by gravity. Therefore, the resonance conditions are preferably fulfilled in one direction (Pinkse et al. 1998). Since these traps are highly anharmonic as well, a comparable behavior to the dipole traps can be expected. To my knowledge, a reduction of the efficiency of evaporation in microgravity was not observed yet.

4.5. Evaporation in a Single Beam Dipole Trap

To investigate evaporation in the PRIMUS system the approach of constant temperature to trap depth ratio (η) was chosen, regarded as optimal for effective evaporation (Olson et al. 2013)⁶. The sequence is discretized in time steps of initially 100 ms which are increased for lower trapping powers, leading to slower evaporation dynamics. Every partition starts with a temperature determination, followed by a calculation of the associated trap depth to fulfill the constant η constraint. A linear dipole laser power ramp is applied, where a non changing temperature would lead to the desired trap depth to temperature ratio. In fact temperature changes while ramping, leading to a slightly increased value throughout the whole sequence. Successful evaporation was reported on a value of η equals ten, but the lifetime measurements from Section 4.1.2 demand fast evaporation. A targeted η of six was chosen because it is the lowest value where theoretical assumptions on trap harmonicity are still valid. In reality it stayed surprisingly constant at $\eta \approx 6.6$ over several time steps.

Results from this measurement are displayed in Figure 4.8, where they are also compared to

⁴The trap depth in this chapter are stated in terms of temperature. This value actually has to be multiplied by k_B to match the right unit. Since this is obvious it is left out for an improved readability.

⁵In several experiment an efficiency of ≈ 3 is routinely achieved.

⁶A constant η is not the best evaporation practice in the presence of dipolar heating effects for example (Pinkse et al. 1998).

4.5. Evaporation in a Single Beam Dipole Trap

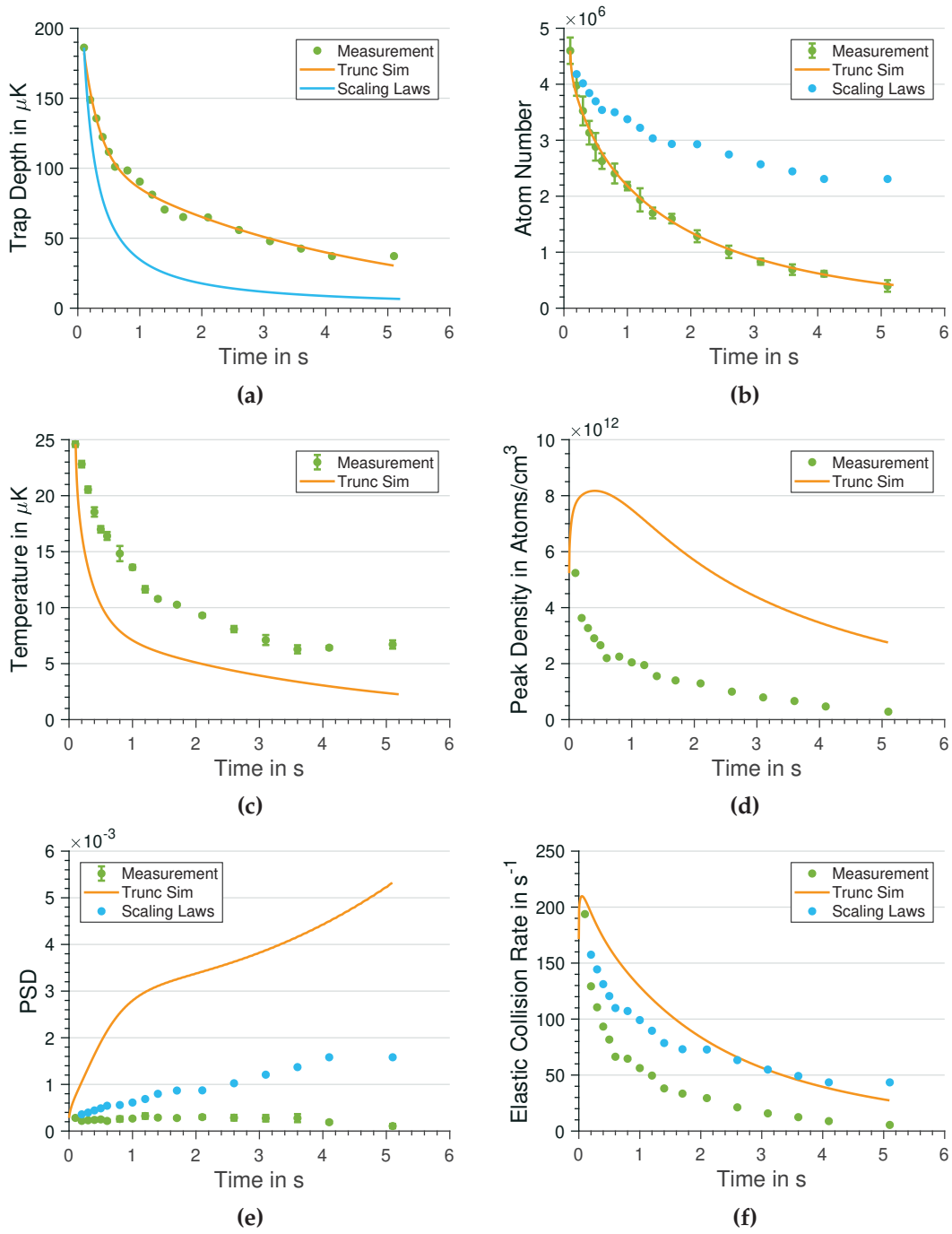


Figure 4.8

Results from an evaporation measurement with nearly constant ratio η from trap depth to temperature. Plotted are the measured data, simulations based on a truncated Boltzmann distribution approach and results from scaling laws. Displayed are (a) the dipole trap depth, (b) atom number, (c) temperature, (d) peak density, (e) phase space density and (f) elastic collision rate of the cooled ensemble over time. A detailed explanation can be found in the text.

4. Evaporation in a Dipole Trap

simulation results from the truncated Boltzmann (*Trunc Sim*, see Section 4.2.4) and the scaling approach (Section 4.2.5) theories.

This paragraph will go through some characteristic quantities, starting with the dipole trap depth, displayed in Figure 4.8(a). The recorded data (green dots) can be fitted with the sum of two exponentials (orange line). Since the system is operated at constant η , natural evaporation does not occur and a single exponential is expected to describe the evolution, which is only true for times shorter than 2 s. As we will see, an additional heating mechanism causes this discrepancy. Since the fitted curve serves as the basis for the simulation based on truncated Boltzmann distributions, it is modeled as precise as possible regardless of the underlying physics.

In the scaling law approach the evolution of trap depth is an output parameter (blue line). It can clearly be seen, that this theory is too simple to describe our real system. Anyway, it presumes constant trap depth to temperature ratio and gives a much faster trap depth decrease. This means, it expects the sample to cool a lot faster, indicating a heating mechanisms not covered by the simulation, further discussed in the paragraph about temperature evolution.

Gravitational effects on the evaporation process can be neglected in this dataset since the final trap depth value of $U_0=37 \mu\text{K}$ is too high to allow for a significantly altered potential.

The recorded evolution of atom number can be found in Figure 4.8(b). The atom number decreases during the evaporation sequence by roughly an order of magnitude. The curve can well be approximated by the *Trunc Sim* code, if one- and two-body losses are included. While the rate of density independent losses is set to be $\Gamma_{1B} = 0.2$, equivalent to a lifetime of $\tau=5 \text{ s}$ as identified in Section 4.1.2, L_{2B} was determined to $7 \times 10^{-14} \frac{\text{cm}^3}{\text{s}}$ for best agreement. This value lies well in the expected range between $4.7 \times 10^{-14} \frac{\text{cm}^3}{\text{s}}$ and $5.8 \times 10^{-13} \frac{\text{cm}^3}{\text{s}}$ (Burke et al. 1997) for spin exchange collisions, indicating ground state changing dipole trap atom interactions, caused by the multimode nature of the utilized laser. The sufficient modeling with these loss mechanisms furthermore means that three-body losses do not appear in our dipole trap setup, at least for the densities of this dataset. They might still come into play on our road to quantum degeneracy with increasing density.

Scaling law results were obtained by using the measured trap depth. Nevertheless, a strong deviation from the data does not surprise, keeping in mind the absence of loss mechanisms in the theory.

The ensemble's temperature decreases by a factor of 4 over 5 s, as it is plotted in Figure 4.8(c). Interesting is the discrepancy between simulation and recorded data. The overestimation of cooling efficiency can be compensated for by a reduction of the simulated trapping beam waist to approximately $35 \mu\text{m}$. Even though a slightly reduced beam waist can not be excluded by the measurements on beam propagation (Section 3.2) or trap frequencies (Section 3.4), it comes with two drawbacks. First, it becomes impossible to reproduce the evolution of atom number and second, it results in a higher initial atomic peak density than reported for any other experiment

before.

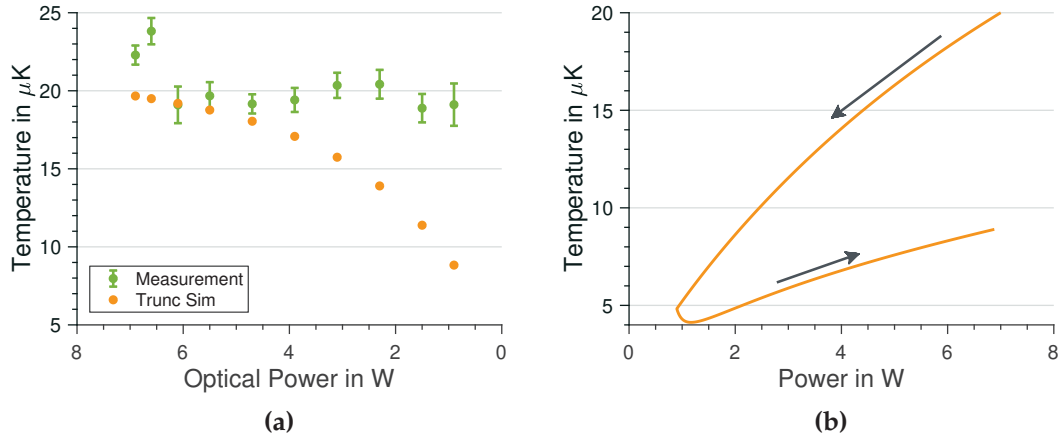


Figure 4.9

Evidence for a heating process in the dipole trap. The atomic sample is cooled by a sudden trap depth reduction followed by an adiabatic ramp to the initial value. (a) The measured final temperature is independent of trap depth reduction (green dots), where simulations without an additional heating predict a different behavior (orange dots). (b) The temporal evolution of a single simulated data point from (a). One can see the sudden cooling effect (upper branch) of a lowered trap depth which is not equalized by the following trap confinement (lower branch).

More likely is the presence of a heating mechanism which is not considered in theory, namely laser intensity fluctuations, pointing problems or collisionally introduced heating. The subtle temperature increase for an evaporation time of 5 seconds might be a hint for this as well. While the cooling efficiency of the evaporation process slows down with time, a possible heating does not, and becomes dominant for long evolution times.

To test for any of these, the trap was ramped down to different values within 10 ms, creating ensembles at different temperatures, followed by ramping the laser power back to its initial value of 7 W. The second ramp was performed within 500 ms, enough time for an adiabatic compression. Surprisingly the final temperature was somehow independent of the initial temperature decrease, indicating a heating mechanism (Figure 4.9). To validate the expected behavior, an additional simulation using *Trunc Sim* was performed, revealing a decrease in temperature with further lowered trap depth, indicated by orange dots in Figure 4.9.

Repeating this measurement for different final power values gave a distinct relation between temperature and final power. Since this only describes the status of quasi equilibrium where the effect of heating and cooling cancel each other out, no hints about the mechanisms themselves can be extracted. In fact, the exact heating mechanism could not be identified yet and is part of the current project working status. Planned investigation steps can be found in the outlook and include a reconstruction of the vacuum chamber and the implementation of a new stationary laser.

4. Evaporation in a Dipole Trap

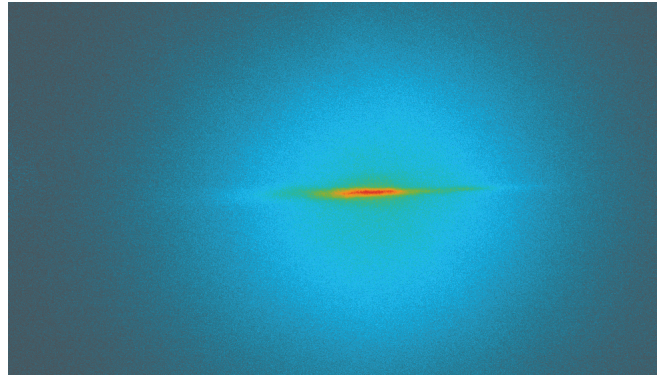


Figure 4.10

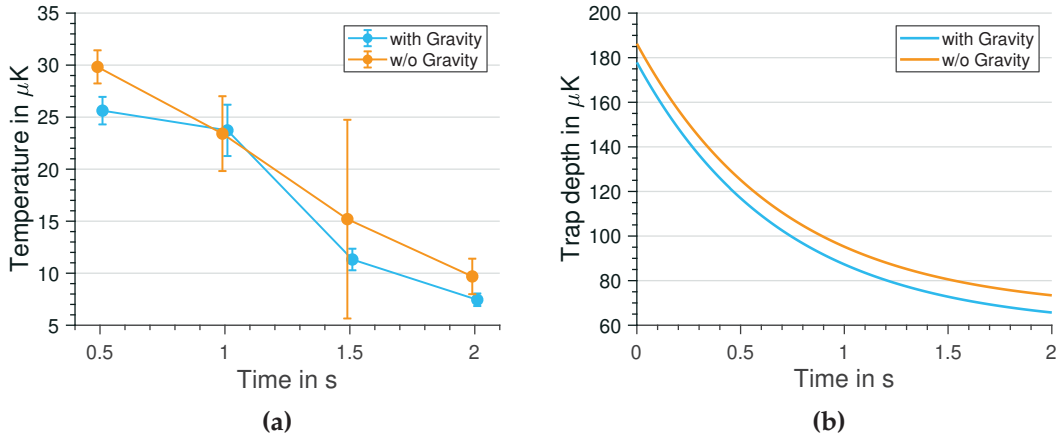
False color representation of a dipole trap in microgravity overlaid with non trapped atoms from the optical molasses. The picture was recorded 200 ms after loading. In this moment the cloud in the background is dense enough to allow for dipole trap measurements.

Focusing on the peak atomic density in the recorded dataset, as plotted in Figure 4.8(d), shows a constant decrease. In an efficient evaporation this value is expected to increase since colder atoms gather at the trap center. In the applied evaporation sequence the atoms are faster expelled from the trap, than collected at its minimum.

In Figure 4.8(e) the evolution of phase space density is plotted. The main goal for evaporation is to increase this value but as can be seen from the measured data (green dots), it does not. This can be attributed to two problems, too many atoms are lost without being evaporated and the contrary acting heating mechanism. In fact the PSD is kept at a constant level throughout the measurement and decreases slightly towards the end. Scaling law simulations predict a moderate growth in PSD due to the overestimation in atom number, *Trunc Sim* expects a 26-fold increase, governed by the temperature underestimation.

The decrease in elastic collision rate caused by lower trap frequencies, is fundamental in lowered dipole traps and can be confirmed by both simulations and measurement. Evaporation is based on elastic collisions and therefore slows down with a decreasing elastic collision rate. Both simulations predict higher rates than measured. While loss mechanisms and unwanted heating are technical problems, the decrease in elastic collision rate is a conceptual one and will be tackled later in Section 4.7.

With all the knowledge about the systems performance on ground, the experiment moves to microgravity. The main issue here is to prove its feasibility and search for possible deviations from ground operation.

**Figure 4.11**

Evaporation in microgravity. (a) Temperature evolution during the evaporational sequence for measurements in the laboratory and in microgravity. (b) Calculated trap depth for the optical power underlying the evaporational sequence. It is hard to see but difference shrinks with lower trap depth towards longer times.

4.6. Single Beam Evaporation in Microgravity

On the 9th of November in 2016 a dipole trap could be realized for the first time in microgravity. It was loaded with approximately fifty thousand atoms in PRIMUS drop number 17. While, as shown in Figure 3.16, the loading procedure does not significantly differ with or without gravity, it does effect atom detection. As one can see in Figure 4.10, the large number of atoms in a molasses cover up dipole trapped atoms. While, under gravity, untrapped atoms vanish in less than 30 ms, they stay in position in microgravity. Even though both signal add up⁷ and should be separable in post processing, measurements shorter than 200 ms did not produce reliable results. This does not affect evaporation recording but could restrict a deeper insight to the loading process.

Having in mind the ineffective evaporation of the system a focus was set on differences between ground and laboratory measurements.

For this sequence the dipole trap was loaded with a CMOT procedure⁸ and the optical trapping power followed the dependency $P(t) = (P_0 - P_{\text{Offset}}) \exp(-t/\tau) + P_{\text{Offset}}$. Here $P(t)$ describes the laser power evolution, P_0 the initial laser power, P_{Offset} an offset providing enough power to trap atoms at lowest power levels on ground and τ defines the ramp's slope. To investigate the evaporation process the sequence was stopped after 0.5 s, 1 s, 1.5 s and 2 s respectively, followed by a free evolution time of up to 10 ms for temperature determination.

According to Figure 4.11(a), the atomic clouds in our setup are generally approximately 3 μK

⁷Except for possible saturation effects.

⁸This procedure loads less and warmer atoms than the molasses technique but lower detunings made it more stable at that time.

4. *Evaporation in a Dipole Trap*

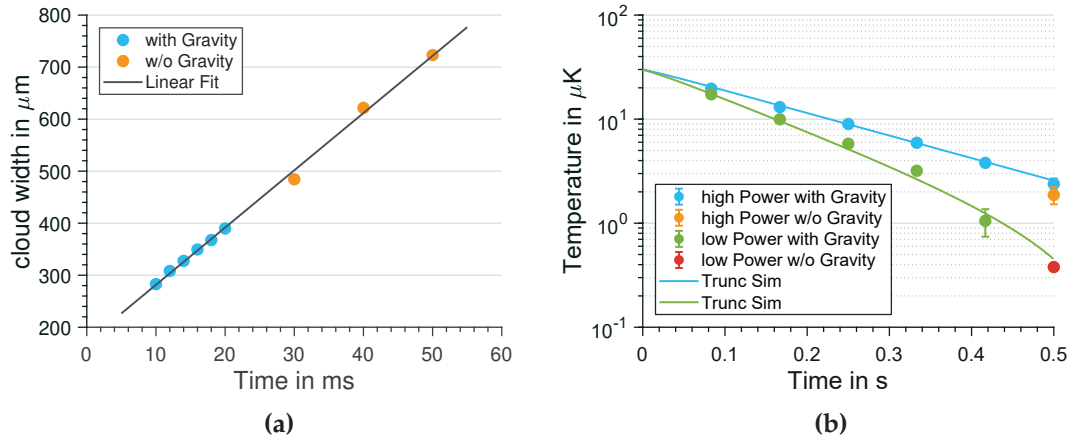
warmer in microgravity compared to ground measurements. This behavior is expected to happen due to the reduced effective trap depth of a tilted potential. Figure 4.11(b) shows the evolution of effective trap depth for the measured configuration. Starting with a difference of $8.4 \mu\text{K}$ it slightly shrinks to $7.1 \mu\text{K}$ within the sequence. Nevertheless, the simulations with the DSMC method can not reproduce such a large difference in temperatures (Figure 4.7). Therefore, the recorded difference is assumed to be a combination of the lowered trap depth and initially warmer atoms. The latter is caused by a reduced CMOT performance in microgravity (Figure 3.13).

The error bars for microgravity data in Figure 4.11(a) represent the statistical error over three (five for 0.5 s) data points. Due to the limited drop tower repetition rate these 14 data points were recorded over the course of three and a half weeks introducing significant performance fluctuations between measurements. A precise comparison between the operation with and without gravity is not possible, but within the uncertainties no difference could be observed. In particular this means, evaporation from an optical dipole trap could definitely be demonstrated for the first time.

An outstanding advantage of trapping cold atoms in microgravity is the applicability of extremely shallow traps. While atoms in a laboratory situation have to be held against gravity, this is unnecessary in microgravity. Owing to the high particle loss rates in this experimental device, a fast power decreasing route was chosen in which the initial power of 7 W was lowered to 270 mW and 70 mW within only 500 ms, referred to as high and low power respectively in this section. On time scales of half a second, evaporation contributes marginally to the cooling mechanism and spilling takes the leading part. Spilling describes atoms in a constant state becoming untrappable by trap depth changes. In contrast to evaporated atoms, where the atomic state changes, the effect purely depends on trap evolution. Spilling can only occur to particles with a kinetic energy close to the trapping barrier. For this reason "hot" atoms get selectively removed from the trap leaving a colder ensemble in the trap, after rethermalization. In contrast to evaporation, such a fast procedure is also referred to as "filtering", since warmer atoms are filtered out of the cloud. The cooling effect of spilling is less efficient than evaporation because atoms can't remove more energy than determined by the trapping barrier.

To validate whether ground and microgravity results can be merged in one dataset, a time of flight measurement was taken with short evolution times on ground and longer ones in the dropping. While under gravity, the falling and expanding cloud reaches the edge of our camera's field of view after 23 ms, in weightlessness these times were extended to 50 ms. The combined dataset, visible in Figure 4.12 (a), can well be approximated by a straight line, as expected from a single dataset.

Having this in mind, only the last data points of the evaporation sequence with the lowest trap depth were recorded in a dropping and the results are plotted in Figure 4.12(b). Comparing both power ramps, lower trapping powers clearly lead to colder atoms, where the orange dot

**Figure 4.12**

Temperature measurements for a fast evaporation in microgravity. (a) Extended time of flight measurements in microgravity (orange dots) agree well with laboratory ones (blue dots). The atomic cloud expands linearly in time, indicated by the solid line. Longer evolution times result in more accurate measurements. (b) Evaporation data for two different optical power ramps. While most data was recorded on ground only the weakest traps were measured under microgravity, resulting in slightly lowered temperatures. An explanation can be found in the text.

represents the microgravity measurements from Figure 4.12 (a), separated from ground data. The final trap in the high power evaporation revealed a temperature of $1.86 \pm 0.35 \mu\text{K}$ in weightlessness and $2.38 \pm 0.31 \mu\text{K}$ on ground. Thus, the dropping results are a bit colder than laboratory ones. Even though both measurements agree within the statistical error budget, we find the same situation for both evaporation ramps. In fact deeper traps without gravity would predict this situation to be inverted. This could be a hint for a more efficient evaporation due to a higher dimension, but it is more likely connected to higher atom numbers in microgravity data (see Figure 4.13(a)). More atoms are causing a higher collision rate, which shortens the rethermalization time and leads to lower final temperatures.

Simulations in Figure 4.12 (b) should be understood as a guide to the eye more than a realistic description of the situation. The underlying theory holds for deep traps where $\eta \geq 6$. In the introduced measurements this requirement is not fulfilled. Remarkably beam waists of a bit more than $30 \mu\text{m}$, relatively close to the actual one, gave best fitting temperature results.

The associated atom numbers reveal the expected behavior of: less particles for lower trapping powers. A rapid power reduction sacrifices huge amounts of atoms to a fast temperature decrease. Most prominent in Figure 4.13(a) are the increased atom numbers for microgravity measurements indicated by the red and orange dot. A difference in trap depth can be excluded as possible reason. Since a higher number in weightlessness fits the explanation, more atoms for less power does not. The most likely explanation for this result is a shift in the position of the trapping laser beam. This has been observed before, caused by the transition from one to

4. Evaporation in a Dipole Trap

zero g. Remarkably this effect was observed for several days but was not fixed to keep setup changes within the drop campaign as small as possible.

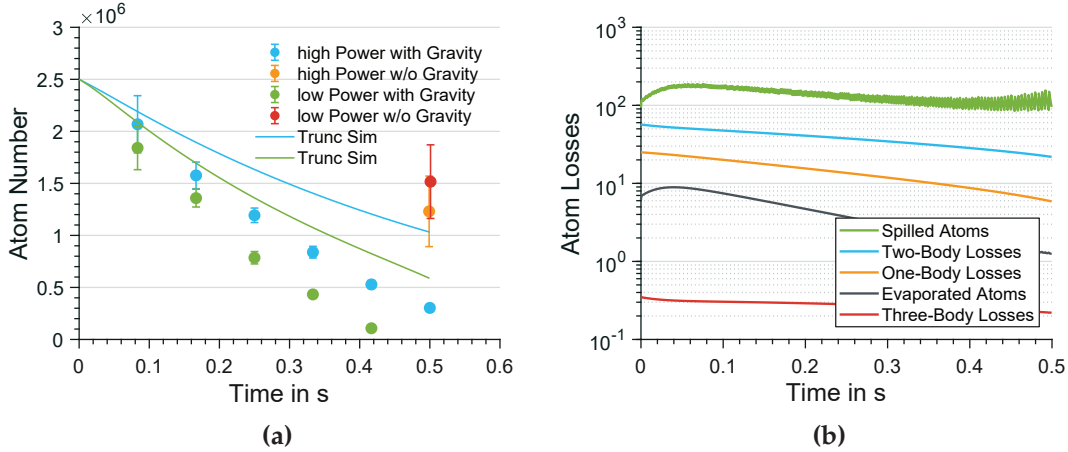


Figure 4.13

Atom numbers in fast evaporation ramps under microgravity. (a) Due to a rapid decrease of trapping laser power, atoms get lost quickly. Numbers in weightlessness are strongly increased indicating a non ideal dipole trap configuration in the laboratory. Losses are generally higher than predicted by the simulations. (b) Contribution to the atom losses, extracted from simulation. Most atoms get spilled out of the trap, followed by two-body losses. While the former is linked to the rapid power decrease, the latter is a good sign, indicating a high density throughout the whole sequence. One-body losses contribute more than evaporation, while the contribution of three-body losses can be neglected.

Simulations were not capable of reproducing the measured particle evolution. Using the above determined loss coefficients results in an overestimation of atom number as it is displayed in Figure 4.13(a). The curves exponential shape permits density dependent loss mechanisms as leading contribution in the sequence, reducing the inaccurate modeling to density independent effects. To test for an unperceived background pressure raise, the simulated lifetime was reduced to a value only 10 % of its determined one, still overestimating the atom number evolution. Excluding all other processes the amount of spilled atoms is certainly largely underestimated by the simulation. Different atom loss contributions are plotted in Figure 4.13(b). The underestimated amount of spilled atoms plays the major role in the cooling process already, followed by two-body and one-body losses. Evaporation plays just a minor role in the experimental sequence and three-body losses can be neglected. The initially growing number of evaporated atoms is attributed to a decreasing η , but the effect is reversed as low trap frequencies slow down rethermalization time.

The fast evaporation gave the coldest possible atomic ensembles for the given setup. The shallowest realized trap only had a residual depth of 800 nK leading to a final temperature of 287.7 ± 3.7 nK. The results for three evaporation ramps can be found in Table 4.2, describing the system's state at the end of evaporation.

Final Power	270 mW	70 mW	30 mW
Atom Number	$1.23 \pm 0.34 \times 10^6$	$1.52 \pm 0.35 \times 10^6$	$1.22 \pm 0.27 \times 10^6$
Temperature	$1.86 \pm 0.35 \mu\text{K}$	$378.7 \pm 30.5 \text{ nK}$	$287.7 \pm 3.7 \text{ nK}$
Phase Space Density	$1.3 \pm 1.1 \times 10^{-3}$	$2.6 \pm 1.2 \times 10^{-2}$	$1.3 \pm 0.3 \times 10^{-2}$
Mean Trap Frequency $/2\pi$	$39.7 \frac{1}{\text{Hz}}$	$20.2 \frac{1}{\text{Hz}}$	$13.2 \frac{1}{\text{Hz}}$
Peak Density	5.07×10^{11}	9.05×10^{11}	3.09×10^{11}
Trap Depth	$7.18 \mu\text{K}$	$1.86 \mu\text{K}$	$0.80 \mu\text{K}$
Elastic Collision Rate	5.17	4.15	1.23

Table 4.2

Results from the fast evaporation in microgravity. All values are recorded at the end of their respective evaporation curve.

The highest phase space density of $2.6 \pm 1.2 \times 10^{-2}$ was not observed in the lowest trap. This is attributed to a higher atom number for evaporation ending at 70 mW. Differences between the two last traps are hard to highlight since the system acts on the edge of what is possible. Our thermal power detector can not deliver reliable results in the drop, since it requires more than a minute to perform a stable measurement. Even the power determination on ground is difficult at these low levels. Anyway the last dataset belongs to a lower final trapping power than the second one, confirmed by the resulting temperature. Considering the optimal loading condition found in this thesis ($N_0 = 1 \cdot 10^7$) results in an initial phase space density of $PSD \approx 1.5 \cdot 10^{-4}$. By evaporation in microgravity it could be raised by at least two orders of magnitude, describing the minimal value due to estimated imperfect loading in drop campaigns. The resulting effectivity of evaporation defined in Equation (4.2) is at least $\gamma_{\text{eff}} = 2.7$, comparable to other experiments. While only a fraction of atoms were evaporated and most atoms spilled away this is a remarkable result.

4.7. Improved Evaporation Concepts

A single beam dipole trap is the simplest dipole trapping concept, but not the one with the most efficient evaporation process. A low trap frequency in one direction permits fast rethermalization and the power reduction aggravates the problem further. This section will describe more sophisticated trapping concepts, most of them tested in laboratory environments, their applicability for this project and future missions.

4.7.1. Crossed Dipole Trap

Crossing a second beam under an angle overcomes the problem of a weak trapping axes in a single beam (Adams et al. 1995). Both potentials add up, forming a narrow potential well with high trapping frequencies in all directions. For equivalent powered beams, the superposition

4. Evaporation in a Dipole Trap

results in a total trap depth of twice the single ray configuration. Only the intersecting region plays a significant role for the evaporation process. A crossing angle of 90° leads to a nearly isotropic potential, while smaller angles provide larger trapping volumes and can be loaded with more atoms. A simulated potential for two beams crossing at an angle of 45° is shown in Figure 4.14. Evaporation dynamics were investigated with the Truc Sim program. Since the situation

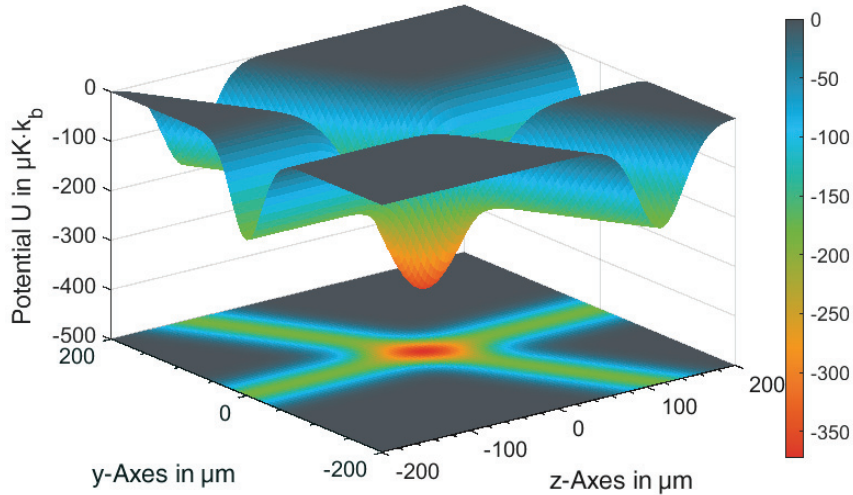
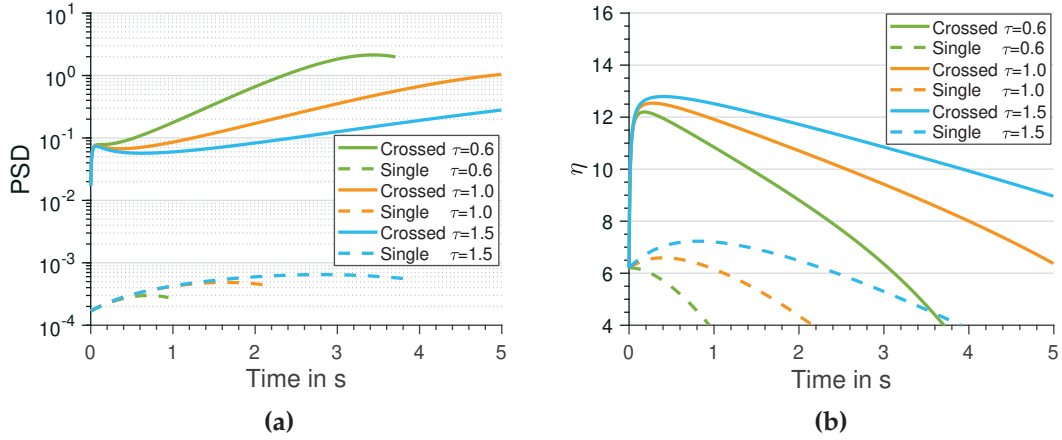


Figure 4.14

Simulated trapping potential for two crossed beams of 7 W each at an angle of 45° . One can see an almost isotropic well in the intersecting region. The trap is less isotropic than for a 90° setup, but is clearly improved over single beam configuration. The trap depth is doubled compared to a single beam trap.

can not exactly be described in this theory, results have to be taken with caution. Anyway, proper estimations can be derived within the theory of truncated Boltzmann distributions. The problem is that atoms with lower energies than the total trap depth are not allowed to leave the ensemble in the simulation. However, in reality they are able to move into one of the "wings", formed by each individual beam. This does not expel them from the process but leads to effectively lowered trap frequencies, especially for low values of η (trap depth in comparison to temperature). Assuming the same initial conditions for both configurations result in a drastically increased PSD for the crossed configuration due to higher trap frequencies. In reality the evolution of atom number in the intersecting region is more complicated than in a single beam configuration. In the beginning of the evaporation process, this area is filled up with atoms from the wings. For this reason the overall number of participating particles might be higher than in the single beam configuration, even though the number of atoms in the crossing region may always be lower. The phase space density evolutions in both beam configurations are plotted in Figure 4.15(a), for different power ramps. Following $P = P_0 \exp(-t/\tau)$, lower values of τ correspond to faster power reductions. For the single beam configuration, the highest PSD values are achieved with slower power reductions, vice versa for a crossed configuration. This

**Figure 4.15**

(a) Simulated evolution of the phase space density for crossed beam and single beam configuration. Different power reduction ramps are tested, where a smaller τ values belong to faster power reductions. In single beam traps slower evaporation ramps are more efficient, in crossed configuration this behavior is reversed due to faster rethermalization. (b) The corresponding η values for the situations of (a). Crossed beam evaporation starts with higher values and decrease shallower. Beneath the value of four the simulation is undefined and was stopped.

is attributed to the desired effect of a reduced rethermalization time. In the one beam case, evaporating atoms can not be "produced" fast enough, thus slowing down the cooling process. At some point the temperature meets one quarter of the trap depth, forcing the simulation to stop⁹, as illustrated in Figure 4.15(b). In both situation the termination criterion is met with a rapid power reduction first. In contrast to single beam evaporation, in crossed configuration it produces the highest PSD values. This is attributed to high loss numbers in the tightly confined ensemble due to density dependent effects. In fact, for this simulations two-body related losses are neglected but the ensemble becomes dense enough to give rise to high three-body loss rates. Including two-body losses to the simulation emphasizes the problem of spin exchange collisions caused by the multimode nature of the trapping laser. The resulting high two-body loss rates permit the formation of a dense cloud. In Figure 4.16(a) the PSD for both configurations is simulated, with and without two-body losses. While a single beam configuration just slightly benefits from suppressed loss mechanisms, it becomes crucial for a crossed beam situation. Owing to the high density of the sample, even three-body losses cause more expelled atoms than evaporation. Unfortunately this mechanism can not be suppressed but has to be balanced with lower densities, for example by a wider trap. The presented simulations in this section belong to a beam waist of $45 \mu\text{m}$ for both beams. While trap frequencies are completely determined by the beam waist (and wavelength) in a single beam trapping scheme, here the mean trap frequency can be changed by a variation of the crossing angle as displayed in Figure 4.16(b). All graphs are based on the same evaporation sequence with a rather fast power reduction.

⁹The numerical implementation for this theory has a singularity at $\eta = 4$ (see Section 4.2.4)

4. Evaporation in a Dipole Trap

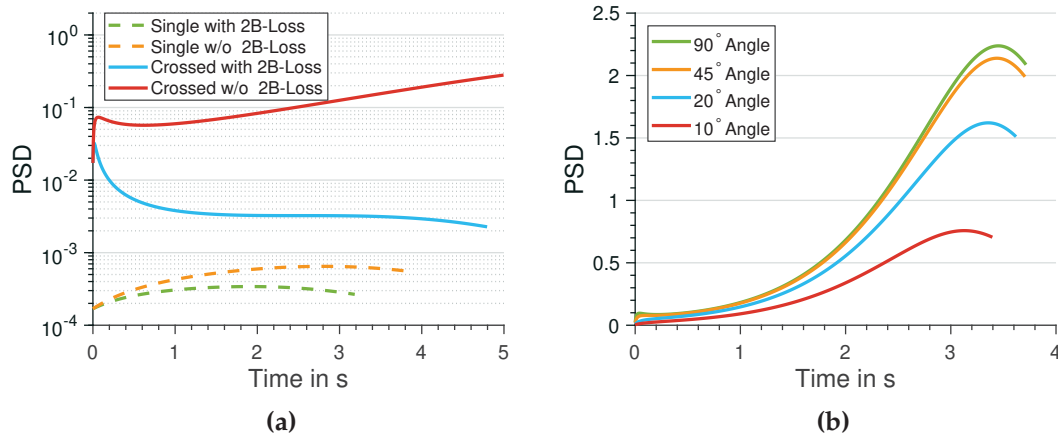


Figure 4.16

(a) Phase space density comparison between single and crossed beam configuration with and without two-body losses. While the loss effect is small in single beam traps it becomes the dominant source for losses in a tight trap. Suppression of spin change collisions is mandatory to create dense atomic samples. (b) Phase space density dependency on the angle between crossing beams. Highest values can be reached in a perpendicular setup, but shallower angles give comparable results. Values below 45° result in reduced performance due to the lower mean trap frequency.

While smaller angles result in slower evaporation due to the lower mean trap frequency, this effect reduces drastically until an angle of approximately 45° is reached. Wider angles do not significantly improve the resulting PSD. This plot also gives hint, that with the achieved starting conditions the formation of a BEC is within reach, occurring at a PSD in the order of one.

Forming a crossed dipole trap with a single laser source may result in interference effects within the intersecting region, giving rise to heating mechanisms and density inhomogeneities. This can either be avoided by shifting their respective frequency to a, compared to the trap frequencies, large value (Liao et al. 2017), or by orthogonal linear polarizations in the two beams. For this reason a crossing angle of 90° is outstanding since it can guarantee orthogonal polarization.

4.7.2. Moving Lenses

A movable lens is inserted into the optical path to be able to influence the volume of the confining potential. The most common setup is shown in Figure 4.17, including a crossed dipole trap configuration (Kinoshita et al. 2005). First, the incoming beam is focused while a second lens is placed at $2f$ distance. Moving the second lens changes a collimated beam to a slightly divergent one. The modified beam passes an AOTF (acousto-optic tunable filter), diffracting the incoming beam like an AOM but furthermore rotating the polarization of the first order by 90° . Before the beams are intersected they pass separate focusing lenses. Depending on the movable lens position, the crossing point coincides with the focus or is slightly misaligned. Since the potential minimum will always be in the intersecting region, this results effectively in different

trapping beam diameters. Atoms can be loaded in a large volume trap and as higher elastic collision rates are needed the trap is compressed.

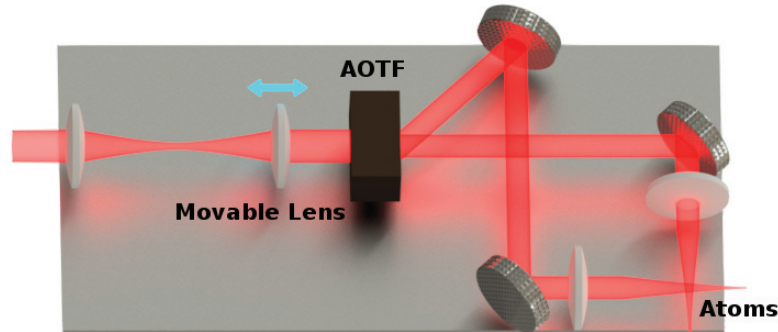


Figure 4.17

Schematic setup of the movable lens configuration introduced in reference (Kinoshita et al. 2005). An adjustable lens determines whether two beams coincide on or off focus, resulting in different trapping beam diameters. A second orthogonal polarized beam is generated by an AOTF.

Experiments were performed with rubidium-87, trapped at a wavelength of 1064 nm¹⁰. While BECs can be produced in 3.3 s the evaporation alone only takes 1 s, starting at a PSD of 1.8×10^{-3} . The initial beam width of 300 μm is decreased to 50 μm , resulting in a 200 fold trapping volume reduction.

The idea could also be implemented in a single beam configuration. Adding a second movable lens, the beam could always be kept collimated but at different diameters. This would lead to a variable beam waist, where the range of available sizes is reduced in comparison with the crossed configuration.

4.7.3. Lattice Enhanced Cooling

Standing Wave

A standing wave can be generated by a retro reflection of the trapping beam, while allowing interference. The result is a single beam shaped potential, which is modulated with $\cos^2\left(\frac{2\pi z}{\lambda}\right)$, but features a trap depth of four times the single beam trap. The corresponding potential for our setup is plotted in Figure 4.18. A stack of pancake like structures appears that are distanced $\lambda/2$ from each other. Note the unequal axes ranges for an improved visibility.

An extremely high trap frequency of 1.2 MHz along the beam direction is calculated. By implementing an angle between the interfering beams, atoms get less confined in axial direction and the trapping volumes increase. In fact hardly any evaporation in an optical lattice is reported. The tight confinement results in relatively high temperatures, making optical cooling techniques feasible again.

¹⁰The reference only mentions the use of a YAG laser but 1064 nm is by far the most common wavelength for this type of laser.

4. Evaporation in a Dipole Trap

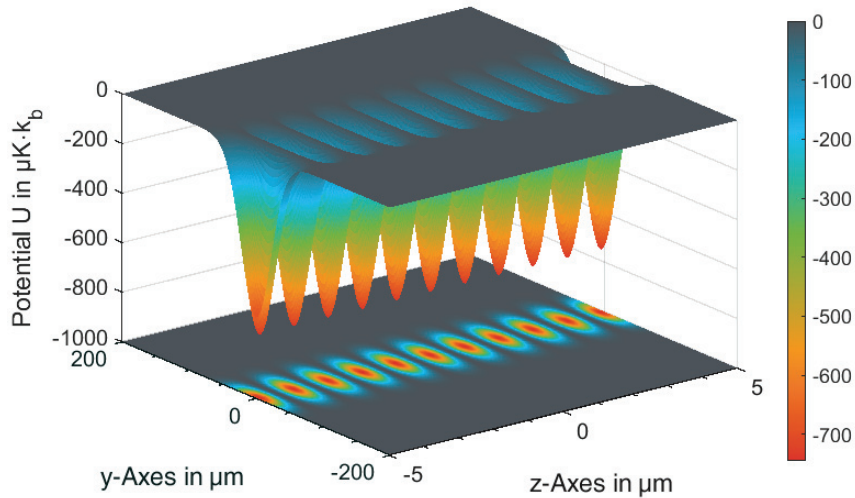


Figure 4.18

Simulated potential of a standing wave with an optical power of 7 W in a retro reflected configuration. Atoms are trapped in several different traps, four times deeper than in single beam configuration with the same power. Plotted is only a small area near the focus of both beams. The overall shape does not deviate from a Gaussian beam configuration, but spatial modulation leads to the pancake like trapping structures. Notice the inequality in axis ranges.

An interesting approach would start from a single optical beam with slowly increasing lattice trap depth. Unfortunately the potential only rests spatially when both beams are equally powered, making any ramping impossible. The desired situation would need a single dipole trap, superimposed with an independent standing wave trap.

Today these one dimensional optical lattices are used for example to create of Tonks–Girardeau gases (Paredes et al. 2004) or single atom trapping (C. Zhang et al. 2006). Furthermore standing waves can play a crucial role in improving atom interferometry precision by providing large momentum transfers.

3D Lattice

In three dimensional lattices, atoms are even further confined. They are used as solid state analogue simulator for example. The number of trapped atoms on a single site is limited and if phase transition occurs it is not straight forward to combine the different ensembles. Cooling in an optical lattice is primarily done optically, leading to BEC formation without evaporation as already described in Section 3.3.6.

4.7.4. Painted Potentials

Lateral movement of the dipole laser beam was described as a source of heating and enhanced loss rates. In fact, this is only true for oscillations that are lower or equal to the trap frequencies.

If the laser oscillates faster than the trap frequency, atoms are not able to follow the movement and become trapped in a time averaged potential, which can be shaped variably (Henderson et al. 2009). This means, the trap can be expanded in the loading phase, which leads to high initial atom numbers (Ahmadi et al. 2005). When the evaporation starts and the optical power is decreased, the mean trap frequency can be kept at a constant level due to a compression of the trap volume. While an exponential power decrease was found to be optimal for time-averaged

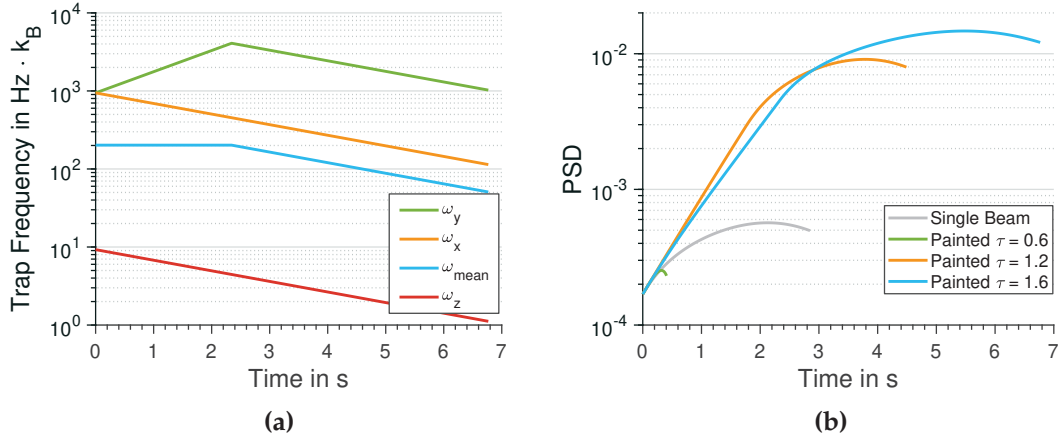


Figure 4.19

Trunc Sim results for a painted potential configuration. In (a) trapping frequency evolution for all axis and the mean is visible. Until approximately 3 s an increase in y-direction can compensate for decreases in both other directions, marked by the constant value for the mean (blue line). (b) Resulting phase space densities for different exponential power reductions. Within 5 s a value of more than 10⁻² can be reached. Fast evaporation in this configuration is ineffective.

potential evaporation, the chosen function for trap frequencies played just a minor role. An impressive application of this technique led to the production of Yb Bose-Einstein condensates in less than 2 s (R. Roy et al. 2016). To consider the advantage of an improved atom number in the beginning of the sequence one has to calculate the number of trapped atoms in relationship to the beam waist. A detailed investigation of this problem can be found in (Ahmadi et al. 2005). Here the simplified approach to Equation 3.31 from (Pruvost et al. 1999) is considered. It is valid for large trap depth and implies a behavior like

$$N_{\omega_{\text{mod}}}^T = \frac{\omega_{\text{mod}}^2}{\omega_0^2} N_{\omega_0}^T \quad (4.34)$$

with the effective beam waist of the modulated beam ω_{mod} and the number of trapped atoms without time-averaging $N_{\omega_0}^T$.

The same initial parameters were used for all the simulations in this section. These are a maximum trapping power of 7 W, focused to a beam waist of 45 μm , which holds $5 \cdot 10^6$ atoms at a temperature of 30 μK , resulting in $\eta \approx 6.2$.

4. Evaporation in a Dipole Trap

Increasing the effective beam waist to $55 \mu\text{m}$ would lead to $7.5 \cdot 10^6$ trapped atoms at the beginning of evaporation. Since the optical power remains the same, and the power is spread over a wider area, the trap becomes shallower. For these numbers, the ratio of trap depth to temperature drops to $\eta = 4.1$ already. This shallow trap is incapable of efficient atom loading, and it is an impossible starting point for an evaporation simulation with *Trunc Sim*. Obviously, an efficient increase in initially loaded atoms numbers by means of painted potentials, requires higher optical trapping powers.

For the simulation of an increased efficiency of evaporation in a painted potential, a beam waist of $5 \mu\text{m}$ was assumed. This value is valid, since a diffraction limited operation of the assembled lens would have a minimal beam radius of $4.7 \mu\text{m}$.

The resulting trap frequencies are displayed in Figure 4.19(a). In the modulated y-direction ω_y increases to compensate for decreasing trap frequencies in x- and z-direction until the minimal beam waist is reached. Up to this point, one can see a constant mean frequency, that drops afterwards. Phase space density improvements were observed to be relatively slow (Figure 4.19) but could reach the 10^{-2} level.

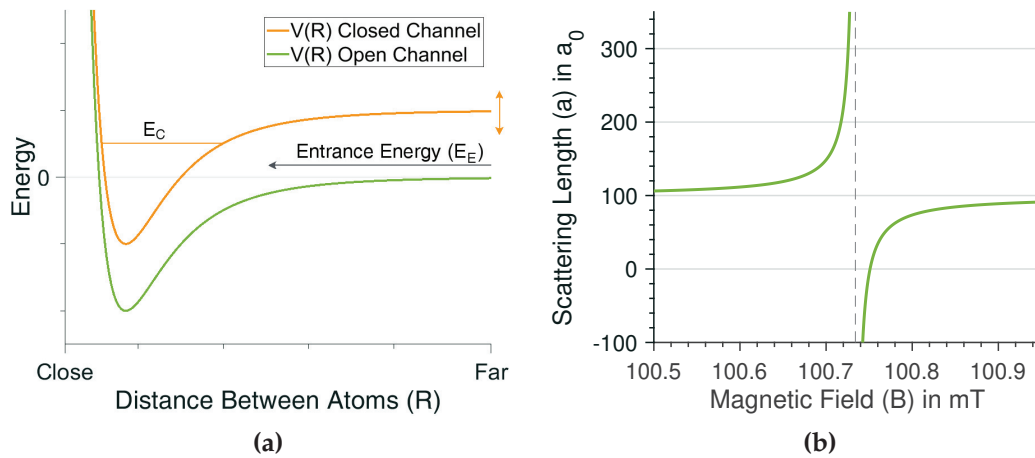
For further applications, other trapping geometries, like double well potentials (Harsono 2006) can be generated. They will providing interesting physics and have never been realized in microgravity before.

4.7.5. Feshbach Enhanced Rethermalization

Feshbach resonances provide the possibility to tune inter atomic scattering length (Feshbach 1958; Chin et al. 2010). They are described by scattering theory, considering two molecular potentials, called open and closed channel (see Figure 4.20(a)). The latter is energetically well above the kinetic energy of both collisional partners for long distances, called entrance energy (E_E) but provides short range bound states with the energy E_C . For the ultra cold regime the entrance energy is nearly zero. Coupling between both channels can be manipulated by shifting these potentials (orange arrow), for example by applying a homogeneous magnetic field. The closer E_E and E_C are the stronger is the coupling between both. In Figure 4.20(b) the scattering length dependence on magnetic field strength is plotted exemplarily. Atomic interaction can be randomly tuned from attractive to repulsive and vice versa in the vicinity of a Feshbach resonance which is generally described by the scattering length

$$a(B) = a_{Bg} \left(1 - \frac{\Delta_F}{B - B_0} \right). \quad (4.35)$$

Here Δ_F is the resonance width, B_0 equals the resonance position and a_{Bg} describes the background scattering length far away from resonance. All three characteristics depend on the atomic element and internal state choice. For rubidium-87 in $F=1$ there are no known resonances between partners in the $m_F=-1$, but four of them in the $m_F=1$ state for magnetic field strength between 0.05 mT and 126 mT (Marte et al. 2002).

**Figure 4.20**

(a) Feshbach resonances are formed when an molecular state is present in the vicinity of open channel threshold energies. The coupling between both states depends on their level of degeneracy which can be tuned by a homogeneous magnetic field. Variations in the field strength result in different behavior of inter atomic scattering length. In (b) this dependency is plotted exemplarily for a broad resonance in rubidium-87. The scattering length is given in units of the Bohr radius a_0 .

The idea of Feshbach enhanced cooling is to compensate the trap frequency decrease due to a lowered optical potential, by enhancing the elastic collision rate to keep the evaporation process running (Gross et al. 2008). Maintaining a constant elastic collision rate demands precise control over the scattering length. So on one hand we need a suitably broad resonance, on the other it should be located at the lowest possible magnetic field to minimize power consumption, thermal heating, residual magnetization and Eddy currents.

The paper by Marte *et al.* provides two interesting candidates for our experiment. The lower one is centered around 68.5 mT and is 1.7 μ T broad. The initial elastic cross section in the PRIMUS experiment is 330 a_0 , for typical parameters in a single beam configuration. Keeping this value constant throughout the sequence would lead to a final current in our MOT coils of approximately 16.5 A. This differs only 176 μ A from the value corresponding to the resonance center. Furthermore the position of coils was chosen to be closest possible to the atoms, to generate strong magnetic fields with low currents. This optimization led to a distance to radius ratio of 0.85, not the ideal Helmholtz configuration of 1 (Ganske 2012). The resulting deviation from a spatially constant magnetic field can be seen in Figure 4.21(a). A field variation of 7 μ T at one millimeter pushes the trap edges over the resonance for the given values, resulting in a negative scattering length and high atomic loss rates. For an effective Feshbach enhanced evaporation another resonance, centered at 100.73 mT with a width of 170 mT, has to be chosen. The situation of a constant elastic collision rate was simulated with *Trunc Sim* and results are plotted in Figure 4.21(b). The non enhanced trap (gray line) has been shown before and is plotted as reference to the new data. A high collision rate between atoms leads to short

4. Evaporation in a Dipole Trap

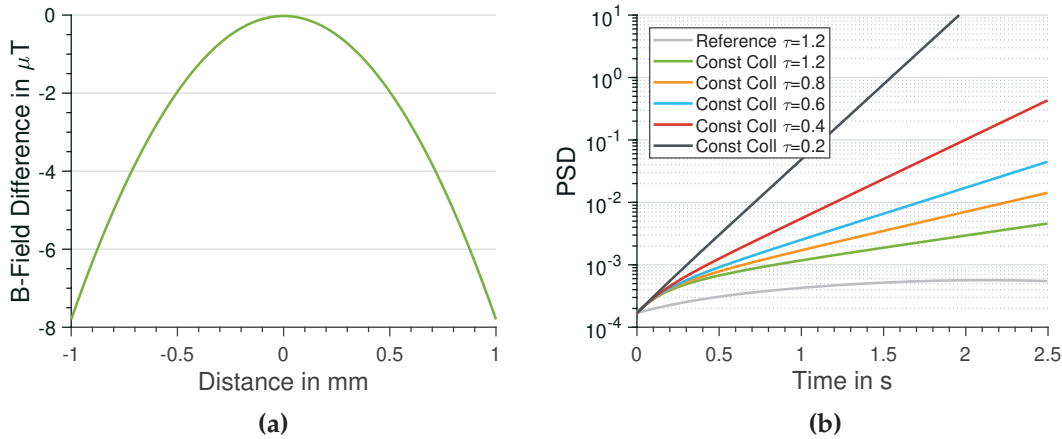


Figure 4.21

(a) Magnetic field deviation from a perfect homogeneous field in the used experimental setup. Applying a field of 68.5 mT leads to a quadratically shaped deviation with a curvature of $7.8 \frac{\mu\text{T}}{\text{mm}^2}$. (b) Simulated evaporation results for different exponential dipole power ramps with constant elastic cross section. Compared the situation without an applied Feshbach resonance, evaporation can be forced significantly faster and quantum degeneracy is reached in approximately 1.5 s

rethermalization times and provides the opportunity for fast evaporation. Choosing $\tau = 0.2$ and starting the simulation with realistic experimental conditions, quantum degeneracy can be reached within only 1.5 s. Even the slow evaporative sequence strongly benefits from Feshbach enhanced evaporation. Changing parameters for density dependent losses were not included in the simulation but will effect the result (Marchant et al. 2012), so the stunning findings have to prove validity in a real experiment.

Common practice is the slightly different approach to apply Feshbach resonances for controlling sympathetic cooling, where an actively cooled atomic species passively cools another one (Roati et al. 2007).

Another approach of evaporative cooling making use of Feshbach resonances is based on relative velocity between particles (Mathey et al. 2009; Nuske et al. 2015). In the vicinity of a resonance, untrapped molecules are formed, or both partner gain enough kinetic energy to leave the trap.

4.7.6. Hybrid Trap

The term hybrid trap describes all combinations of optical and magnetic potentials. It can even be found when the potentials are applied successively. A famous example is the optically plugged quadrupole magnetic trap (K. B. Davis, Mewes, Andrews, et al. 1995) where a blue detuned potential pushes atoms out of the magnetic tap center, avoiding Majorana spin flip induced losses.

Here we focus on two different implementations. A dipole trap that becomes magnetically

confined in the axial direction and a tilted trap where a magnetic gradient lowers the effective trap depth.

Magnetic Confinement

Single beam optical dipole traps are known for a weak atomic confinement in the axial direction. The initially low trap frequency can be increased by an overlap with a magnetic gradient. This does not only improve the initial value but can be kept constant throughout the evaporative sequence.

For the simulation displayed in Figure 4.22 all atoms are considered to be in the $|F=1, m_F=-1\rangle$ state and the centers of both traps are displaced by $100 \mu\text{m}$. The displacement is mandatory to prevent high loss rates due to Majorana spin flip losses and is typically in the order of a few dipole trap beam waists. Radial trap frequencies, dominated by the optical potential, are calculated similar to the single beam configuration. In the axial direction optical and magnetic traps are considered as (Colzi et al. 2018)¹¹

$$\omega_{ax}^{Hybrid} = \sqrt{\frac{4\mu B'}{mz_0} + \frac{4U_0}{mw_0^2}}. \quad (4.36)$$

The first term under the root is the squared magnetic trap frequency, while the second one is the same for the dipole potential. B' is the magnetic field gradient in weak direction, the magnetic moment $\mu = -m_F g_F \mu_B$ is described by magnetic quantum number,

Landé g-factor and the Bohr magneton. z_0 denotes the explained offset between trap center and the optical trap minimum. The magnetic field gradient is assumed to be $0.7 \frac{\text{mT}}{\text{cm}}$, which is the field our MOT coils produce in their weak direction.

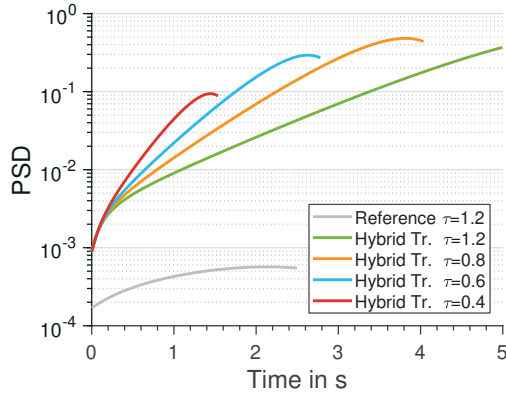


Figure 4.22
Simulated evaporation results for the magnetic confinement technique. Relatively low trap frequencies demand a slow evaporation sequence for best results.

As one can see from Figure 4.22 slow evaporations give best results for the magnetic confinement technique. Even though the axial trap frequency is increased from 9.3 Hz to 48.6 Hz the new value is still rather low, compared to trap frequencies in the radial direction or for purely magnetic traps. Furthermore the radial confinement still drastically reduces throughout the whole sequence. The

¹¹In this reference the four accidentally dropped into the denominator but should be in the numerator as it is for example in (Mishra et al. 2015).

4. Evaporation in a Dipole Trap

transition to quantum degeneracy could not be observed in the given simulations. This goal could be reached with a steeper magnetic gradient or lower density independent losses.

Experimentally, a similar procedure produced BECs every 20 s with a magnetic field gradient of $1 \frac{\text{mT}}{\text{cm}}$ in the ATLAS experiment (M. Zaiser et al. 2011). Even though large parts of this experiment are similar to our setup, these results could not be reproduced due to a worse vacuum quality.

Tilted Trap

Using a magnetic gradient field to effectively tilt the optical potential allows for a reduction in trap depth with only slight changes in trap frequency (C.-L. Hung 2011). Considering the gradient field to be produced by our MOT coils, a gradient of approximately $4 \frac{\text{mT}}{\text{cm}}$ can not be exceeded. For a trapping laser power of 7W this belongs to a reduction in trap depth for atoms in the $m_F = -1$ state from $186 \mu\text{K}$ to $175 \mu\text{K}$. This change is hardly recognized by the trapped atoms and according to Figure 4.23(a), the effect is similar to a gravitational drag. This means, reversing the magnetic field leads to a force that balances gravity and giving rise to long evolution times in a laboratory environment (Jenkin et al. 2011). The gradient of $73 \frac{\text{mT}}{\text{cm}}$ to overcome the dipole trapping force is not realistic in our experimental setup. For the

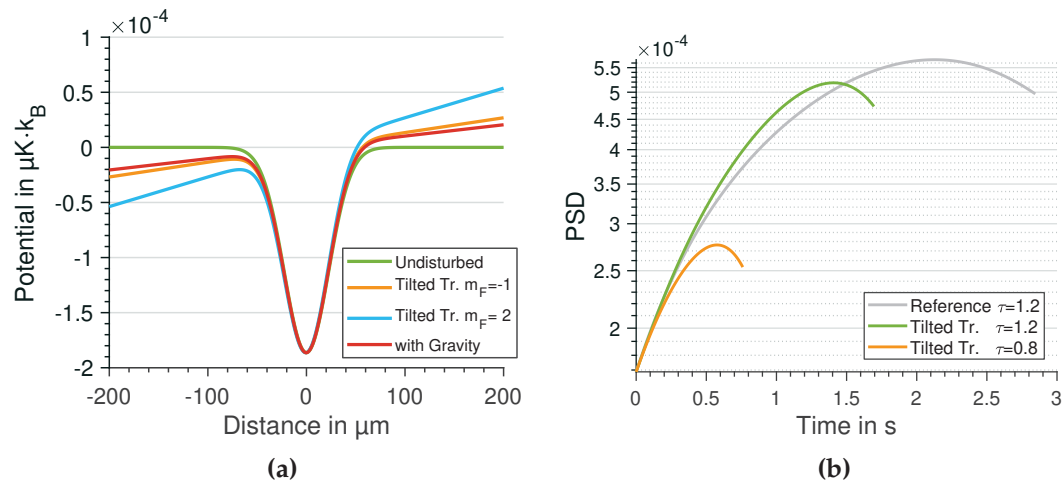


Figure 4.23

Simulation results for the tilted trap configuration. (a) Comparison of different potential in direction of gravity or magnetic gradient respectively. The effect of magnetic tilting is comparable to the effect of gravity. (b) PSD evolution for different evaporation sequences compared to a single beam configuration. In the given setup the technique does not improve the evaporation at all.

simulation, no ramp was applied to the magnetic gradient due to the small effect on evaporation. It is kept maximized throughout the sequence, giving the results in Figure 4.23(b). In fact the performance was even worse than the reference from a single beam configuration. Even though the PRIMUS experiment does not benefit from tilted potentials, this technique could be a key technology in combinations between atom chips and dipole traps. In these setups the

temperature of dipole trap loaded atoms is massively decreased, including lower trap depth, and the available gradients are high, due to the proximity between wires and atoms.

4.7.7. Conclusion to Improved Evaporation Concepts

Several strategies for an efficient evaporation from a dipole trap were introduced in the last section. Here this information is used to choose the best solution for the PRIMUS experiment. The overall idea, as mentioned before, is a simple and robust experimental setup. For this reason movable parts were excluded from the experiment whenever possible. Following this strategy, movable lenses are undesired due to potential mechanical problems. Lattice enhanced cooling techniques are not famous for evaporation, but direct laser cooling to quantum degeneracy. For long interrogation times in the drop tower, phase transition is not as important as a low kinetic energy. For this reason and the need for highest possible atom numbers, lattices are not the right choice to produce a source for atom interferometry in microgravity.

The magnetically tilted trap turned out to be an interesting candidate in atom chip configurations but comes with no improvement in the current setup. In contrast, the magnetically confined trap delivered phase space densities close to the BEC transition. In order to reap its full benefits, an improved vacuum quality is needed. Evaporation times of more than 5 s most certainly disqualify this technique for drop tower operation. Anyway, coils for the magnetic field are already installed and the system is robust against slight misalignments making it a reliable fallback option.

Feshbach enhanced evaporation performed the most effective by far but the experimental complexity strongly depends on the element choice. Rubidium-87 is definitely on the difficult side of the spectrum, making this procedure not the first choice for this experiment. If possible, tests with potassium can confirm the extraordinary simulation results and future devices can be optimized for this method, leading to extremely fast evaporation.

The crossed beam configuration impresses with an initially improved phase space density followed by a good performance in evaporation. Because it is an all-optical technique, the advantages of these remain, making it the first choice for improved evaporation in microgravity. Since the initial laser power is relatively low, a recycling of the beam is more useful than a beam splitting. An implementation of a bow tie configuration will be found in the next chapter.

Painted Potentials turned out to be a powerful tool for initially deep traps. It performed well until the minimal effective beam waist is reached and evaporation equals the standard single beam configuration. A useful solution to this problem would be the combination between a crossed dipole trap and a painted potential. Not only does this double the effective trap depth but the modulation acts on two different trap frequencies, compared to only one in a single beam configuration. Both effects will boost the feasibility of painted potentials in our setup. An

4. Evaporation in a Dipole Trap

implementation is beyond the scope of this thesis, but will certainly be done in the future.

4.8. Realization of a Crossed Dipole Trap

A crossed dipole trap was realized in the PRIMUS experiment by using a bow-tie configuration. A drawing of the modified setup can be seen in Figure 4.24. The single beam dipole trap laser is re-collimated by a second lens and reflected by a silver coated mirror through a $\lambda/2$ waveplate. The 90° polarization rotated wave is directed towards the center of the vacuum chamber and focused again, resulting in a crossed dipole trap with an angle of 45° between initial and reflected beam. Having no right angled trap, we found it crucial for trap lifetimes to control the beam polarization. If recycled dipole trap beams are not orthogonal polarized, interference effects between them lead to a heating processes, causing atom losses¹². Inserting a third Glan-Laser prism right behind the polarization rotation, significantly extending the trap's lifetime. In this configuration it became comparable to single beam operation. Single and

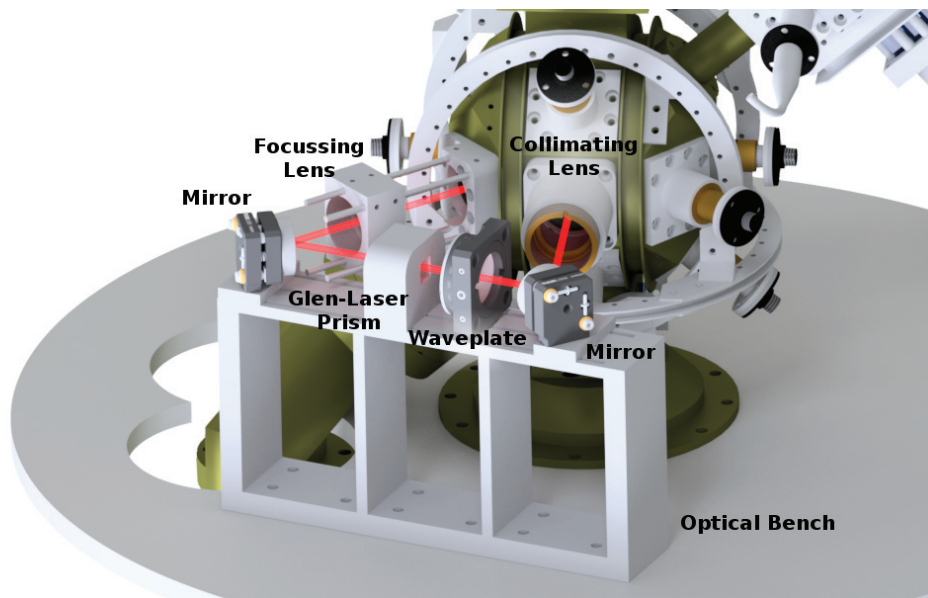


Figure 4.24

Experimental setup modifications for a crossed dipole trap. After focusing the beam for a single beam trap it gets collimated again. The polarization is rotated orthogonal to the incoming beam and an additional Glan-Laser prism filters the desired polarization, also canceling possible incoming polarization variations. The reflected beam is focused again and crosses the first beam at an angle of 45° .

crossed beam configuration were compared by repeating the constant η sequence, introduced in Section 4.5, for the latter. Due to the tighter confinement, an optimized evaporation ramp would require a faster power reduction. The results of this measurement are plotted in Figure 4.25.

¹²The problem can also be solved by frequency shifting one or both beams by passing an AOM.

In crossed configuration, the temperature is a little bit higher throughout most of the sequence (Figure 4.25(a)). This can well be attributed to the tighter confinement of the atoms. Since the cooling effect in the single beam stops at approximately $6\ \mu\text{K}$, the new setup can match this value at the end of the sequence. Interestingly, the final achievable temperature equals, even though the optical power in the crossed configuration is twice as high as in the single beam. This excludes an optically induced heating as the reason for the lower temperature limit.

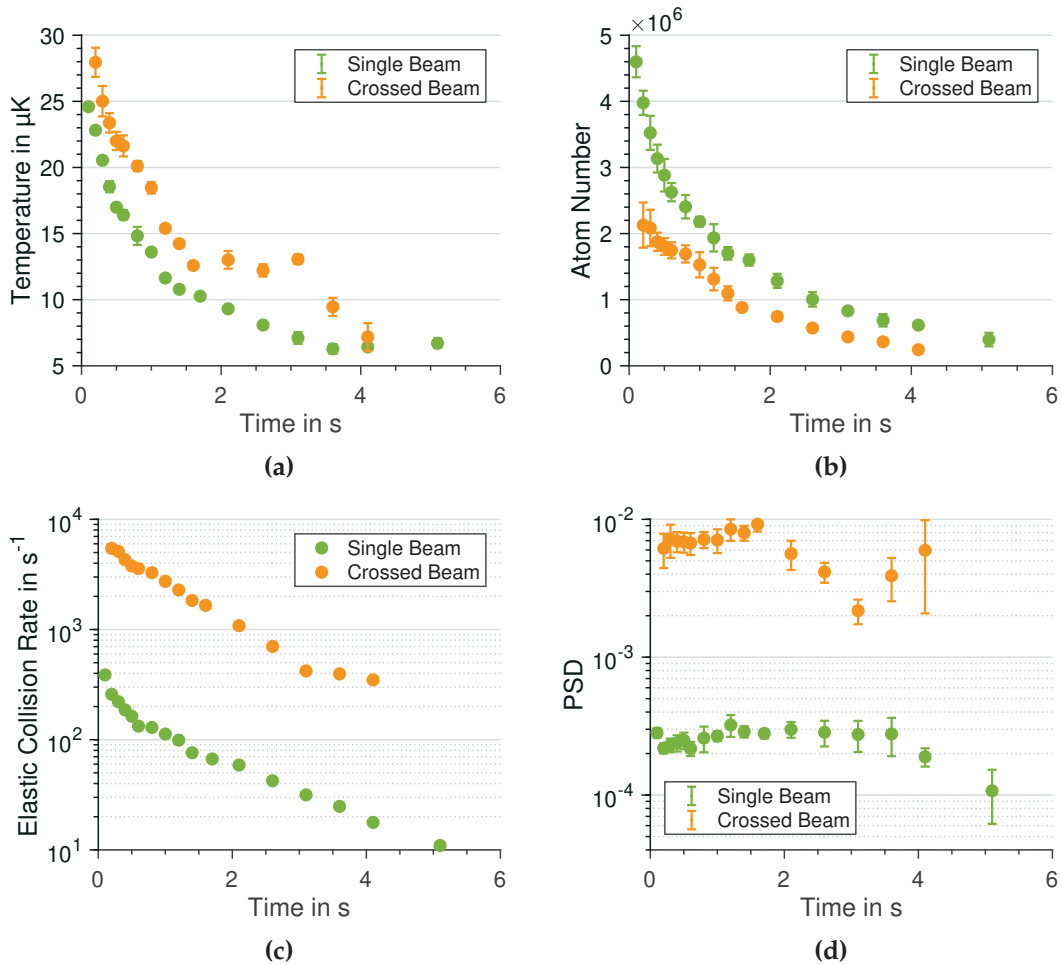


Figure 4.25

Comparison between evaporation in a single beam and a crossed beam configuration. Optical power ramps are equivalent in both cases. (a) The temperature in crossed configuration is slightly increased due to the higher atomic confinement. (b) Atom number evolution does not follow a simple exponential curve due to exchange between the intersecting region and its wings. A lower atom number in crossed configuration is associated with technical problems. (c) Calculated elastic collision rates are increased by an order of magnitude in the crossed region, compared to single beam operation. (d) The Phase space density is massively increased. These ideal starting conditions for a fast production of quantum degenerated clouds result from a significantly higher initial mean trapping frequency.

4. Evaporation in a Dipole Trap

The evolution of atom numbers can be seen in 4.25(b). For evaporation times, longer than 1 s, the atom numbers follow the same exponential trend as for the single beam measurements, with an approximately constant offset. For shorter evaporation times, the recorded dynamics clearly differ.

Loading a crossed dipole trap with a molasses scheme does not only load atoms into the intersecting region but also into the so-called wings. Those are the trapping regions formed by both single beams individually. The resulting loading dynamics can be seen in Figure 4.26(b) where the ratio of trapped atoms in the crossing region, is compared to the overall amount of atoms, in a lifetime-like measurement with constant laser power. Within the first second of trapping, the ratio increases rapidly until it reaches a plateau for loading times that exceed one second. This is exactly the timescale identified, as dominated by natural evaporation. While cooling down, proportionally more atoms are evaporated from the wings, than they are from the center.

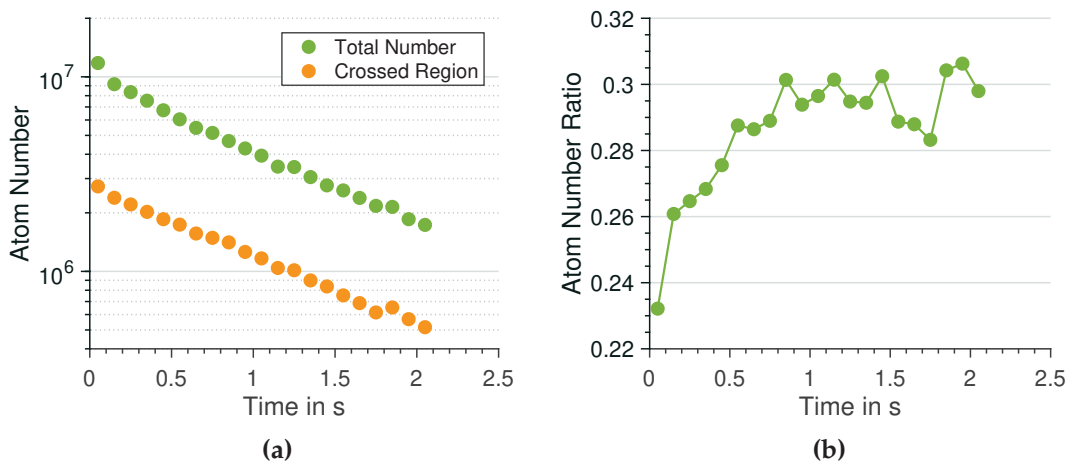


Figure 4.26

Investigation of trapped atom distribution in a crossed dipole trap. Roughly one fourth of the atoms are located in the intersecting region for a fully powered dipole trap. Holding the trap for one seconds reveals a slightly slower decay rate in the crossed region due to migration from the wings to the center driven by natural evaporation. The effect is easier observable in (b) where the ratio between both regions is plotted. The solid line serves as guide to the eye only.

In Figure 4.26(a) the crossed region atom number is separated from the overall one. While the total amount of atoms decays mostly exponentially, the crossed region slightly deviates from this behavior within the first second. This indicates atoms that are moving from the wings into the crossed region. The effect is remarkably small since wing trapped atoms can not simply move to the center and be trapped in the deeper potential of this region. The conservative potential requires additional collision events. However, the ratio of *crossed trapped* atoms to *wing trapped* atoms increases with an overall temperature decrease.

It is also worth mentioning that $1 \cdot 10^7$ atoms could be loaded in the crossed beam configuration in total. Thus the reduced atom numbers in the constant η measurements on Figure 4.25(b) were caused by performance fluctuations, not a scientific problem.

A huge advantage of a crossed dipole trap can be seen in Figure 4.25(c). The elastic collision rate increased by an order of magnitude compared to single beam operation and the lowest final value almost matches single beam starting conditions. Unfortunately these values are only true in the crossed region, meaning that for higher temperatures approximately two thirds of the atoms do not benefit from an increased rethermalization. Nevertheless, the problem of slowed rethermalization due to less atomic collisions observed in single beam operation is enhanced at the end of the evaporation. At this point, most atoms will be trapped in the intersecting region and benefit from the increased elastic collision rate.

While temperature and atom number are not significantly different, the phase space density is clearly improved as it can be observed in Figure 4.25(d). The thirty times increased initial value is even further growing in the next two seconds to almost 10^{-2} . As one can see from Equation (4.3) this calculated value strongly depends on trap frequency and atom number. Therefore, it is overestimated for two reasons. First, all atoms are assumed to be in the intersecting region, which is not true for high temperatures and the evolution needs further investigation. Second, all atoms are assumed to be in a single state. Atoms are prepared in the $|F=1\rangle$ manifold, containing three different states. If they are equally populated the calculated PSD value has to be divided by three.

By moving to the microgravity environment, pointing instabilities were recognized. In a single beam configuration, shifts of the beam position lead to different loading efficiencies. In a crossed configuration, they alter the process of evaporation. Observed deviations were easily large enough to form no crossed section at all, while smaller shifts, impossible to recognize, alter trap frequencies and trapping volume.

Two kinds of beam pointing problems were witnessed within the project. First, beam positions were shifted in the transition from gravity to microgravity. These could be diminished to less than $8 \mu\text{m}$, by additional set screws in the mirror holders of the system. Second is a shift during the capsule preparation on ground. The whole four stringer structure got slightly warped and is stressed when the hermetic hull and the upper cover are installed. Even though both problems could, with some effort, get fixed, otherwise we decided to try some active beam stabilization in the future. Similar problems can be expected in future experiments and we also want to test its feasibility for microgravity applications.

The realization of a crossed dipole trap in microgravity can be seen in Figure 4.27. Images from the main camera, in one plane with both beams, provide only reduced information about a possible intersection (Figure 4.27(a)). It is anyway indicated by a sharp peak in the center of the image. For more insight a second camera got installed on top of the chamber (Figure

4. Evaporation in a Dipole Trap

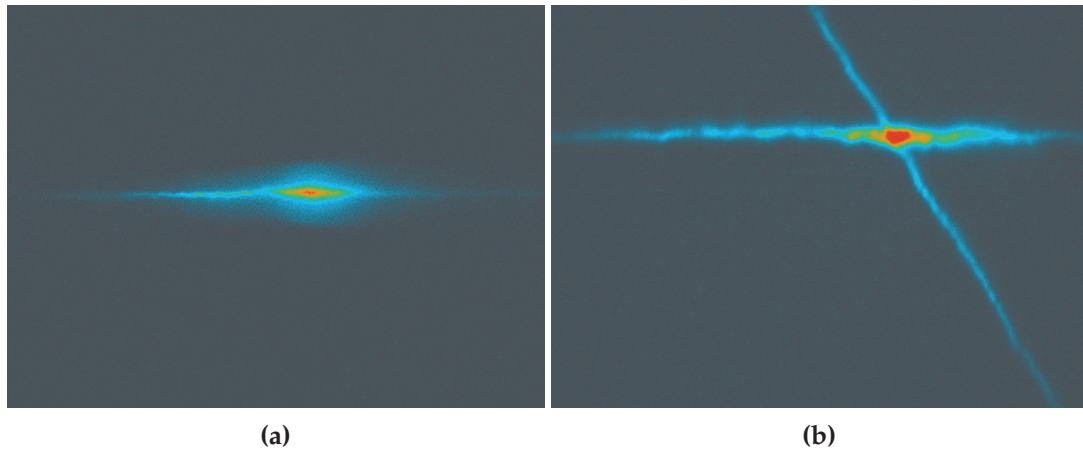


Figure 4.27

False color representation of a crossed dipole trap in microgravity. (a) Side view image taken with the PCO-camera described in Chapter 2 in plane with both beams. The crossing reveals in a hardly observable almost central density peak. (b) Top view from an additional camera installed on the upper vacuum chamber port. Beam intersection creates an area with strong fluorescence, indicating high atomic density.

4.27(b)). Alignment and resulting behavior can easily be observed from this position with the drawback of atoms falling out of focus for laboratory measurements. When both beams cross, the wings appear instantaneously darker and a sharp peak appears, best observable by pixel summation in one direction. It is not possible to determine the position where both beams cross centric. A beam pointing stabilization, coming with position dependent photo diodes, can not only be used active, but also as shift detector. This is crucial for consistent drop campaign measurements.

5. Conclusion

Atom interferometry is a precise quantum tool that will enhance a broad variety of measurements, ranging from large scale phenomena like gravitational wave detection to short scale Casimir-Polder forces and everything in between. Its sensitivity largely benefits from operation in microgravity, due to long free evolution times between laser pulses.

The PRIMUS project aims for a test of the Einstein weak equivalence principle by applying atom interferometry simultaneously to rubidium and potassium atoms. Atom interferometry in microgravity has been demonstrated before, but previous approaches were based on a preparation of cold atomic clouds in purely magnetic traps, called atom chips. Despite important breakthroughs in the application of cold atoms in microgravity, several drawbacks of this kind of traps became evident over the past years. A major concern is the anisotropic trap shape, which limits the capabilities of delta kick collimation, the most advanced technique to generate the coldest atomic clouds possible.

Within PRIMUS, these ensembles of cold atoms, the source for atom interferometry, will be generated in a purely optical dipole trap. Since the creation of an ultra cold (below 1 μK) atomic ensemble, in an optical potential, paves the way for several different experiments (see Chapter 6), this, on its own, is a milestone to the entire scientific *microgravity/cold atoms* community.

Therefore, the primary achievement of this thesis is the first realization of a dipole trap in microgravity. Initially 1×10^7 atoms of rubidium-87 could be trapped and evaporatively cooled to a temperature equivalent of a bit less than 300 nK. The dipole trap is formed by a single 7 W beam focused to a waist of 45 μm leading to trap frequencies of $2\pi \times 944$ Hz in radial and $2\pi \times 9.2$ Hz in axial direction.

The entire experimental setup is compact, robust and autonomous, requirements which must be met to operate in a microgravity environment like the drop tower in Bremen. It easily fits into a drop capsule with $\approx 0.6 \text{ m}^3$ (ZARM 2009) of payload volume. The system was designed to withstand impact forces of 50 g, while the recorded deceleration force did not exceed 36 g. The conditions in the drop tower generally limit the availability of commercially off the shelf solutions. Amongst others, some difficulties are the complete lack of alternating current and only limited supply for cooling water in the drop capsule. For these reasons several setup components are *individual* solutions. One example is the dipole trap laser itself, which is designed by the *Laser Zentrum Hannover e.V.* The laser is mechanically stable and operates without external cooling at full power for ≈ 5 min, which is made possible by using a phase changing material. The laser is thulium fiber based with an output wavelength of 1949 nm.

5. Conclusion

The dipole trap loading was found to be more efficient with a molasses scheme, compared to a temporarily dark MOT, by a factor of roughly two. Atoms could be laser cooled down to about $15 \mu\text{K}$. Compared to ground measurements the performance of laser cooling in microgravity was observed to be a bit less effective. This is caused by technical laser frequency stabilization problems. Dipole trap loading was anyway found to work well in the absence of gravity.

The major difference in evaporation with or without gravity was expected to arise from the different dimensionality of evaporation for both situations. Simulations on a DSMC code revealed an insignificance in the differential evaporation efficiency due to the anharmonicity of the trapping potential itself. Since the principal axis of the dipole trap potential have high mixing rates, the dimension of evaporation is close to the three-dimensional case with and without gravity. The expected effect of an effectively lowered optical potential in gravity could be demonstrated and beneficially applied. Shallow traps, as low as $0.8 \mu\text{K}$, impossible in a normal laboratory environment could be produced in microgravity. This scheme allowed for the preparation of an atomic ensemble with a temperature equivalent as low as $287.7 \pm 3.7 \text{ nK}$.

Several evaporation improving techniques were investigated and simulated with an implemented Matlab code based on a paper from Olsen *et al.* (Olson et al. 2013). Evaporation was found to be most efficient in the vicinity of a Feshbach resonance but to conserve the advantages of all-optical trapping, a crossed dipole trap geometry was identified as most promising for our experiment. The realization of a dense atomic cloud was only hindered by the multimode nature of the utilized laser. The different output frequencies drive atomic transitions, leading to increased density dependent loss mechanisms. This limited the number of trapped atoms in the crossed configuration to about 2×10^6 atoms, where the increased trap frequencies, especially in axial direction, boosted the initial phase space density by more than an order of magnitude. Furthermore crossed dipole traps revealed mechanical stability problems in the experimental setup that will need further care.

The major drawback of evaporation from an optical potential is the decrease of trap frequencies with reduced trap depth. This could be circumvented by applying the concept of *painted potentials*, where a fast spatial variation of the trapping beam results in a time-averaged potential. The combination between a crossed beam dipole trap and painted potentials promises to merge the benefits of a large initial trapping volume with high trap frequencies during the evaporation. This combination was found optimal for evaporating an atomic clouds from an optical potential in microgravity.

6. Outlook

The outlook is subdivided into three categories based on the time scales the mentioned tasks will be tackled. **Short term improvements** describe actions within the next year to rapidly increase the experiments performance based on the knowledge gained in this thesis. **Long term goals** will guide a possible evolution for the project within the next three years. The outlook closes with an overview of this thesis outcome apart from the PRIMUS project, called **the big picture**.

Short Term Improvements

In the lifetime measurements of the dipole trap (Chapter 4), a non sufficient vacuum quality became obvious. To improve this, the pumping section has been redesigned and will be connected to the bottom of the science chamber. Changing the position goes along with an increased connection diameter between the pumping section and the science chamber by a factor of two, resulting in an eight fold better pumping rate (Pfeiffer Vacuum GmbH 2013). Additionally, a titanium sublimation pump was added to the setup. Even though this kind of pump does not trap any new residual gas compound in our trapping scheme, it features an enormous surface, resulting in a high pumping efficiency. The newly designed vacuum chamber is pictured in Figure 6.1.

Apart from the vacuum quality, the formation of dense clouds of cold atoms is impeded by the multimode nature of the utilized trapping laser. To circumvent this problem, a sufficient preparation into the stretched state $|F = 2, m_F = 2\rangle$ will be implemented. This can be done either by an installed laser, initially planned for Raman transitions in the interferometer or by expanding the frequency range of the cooling laser.

The crossed beam dipole trap configuration suffers from an unreliable overlap between both beams, caused by mechanical stress in the entire structure of the capsule. Since this configuration is a key to efficient evaporation and a nearly isotropic potential, the laser will be actively pointing stabilized. The outcome of this is of great importance for space missions that have to run for several years without maintenance.

6. Outlook



Figure 6.1

CAD drawing of the planned pumping section rebuild. An additional titanium sublimation pump and vacuum sensor head will be installed. A larger cross section between dipole trap location and vacuum pumps will improve the lifetime of the trap.

Long Term Goals

A crossed dipole trap geometry provides fast rethermalization of an atomic ensemble, but the evaporation still suffers from a trap frequency reduction with lowered laser powers in this geometry. This problem can be circumvented by applying AOM driven *painted potentials*. Since the ATLAS experiment already implemented such advanced trapping potentials, it will soon be transferred to the PRIMUS drop tower atom interferometer. The combination of both methods will accelerate the evaporation process, resulting in a fractional higher microgravity time to perform interferometry, for example. On ground, faster evaporation is linked to higher repetition rates for experiments. Shorter cycles provide more statistics leading to more accurate measurements, not limited to our project. Furthermore, the variability in trap shaping is an ideal ground for optical delta kick collimation and will further reduce the cloud's expansion rate.

It will be challenging, to precisely determine the resulting ultra low temperatures. For this reason, the new vacuum design offers a second detection zone 195 mm beneath the current one, that will allow for free fall times of ≈ 200 ms. The limited availability of the drop tower, coming with a lack of statistics, turned out to be a bottleneck to some measurements. The new design will allow for a higher flexibility on ground. Unfortunately, since the atoms are leaving the magnetic shield while falling, this can not be utilized for high precision measurements.

Loading the dipole trap under microgravity has been done within this thesis, nevertheless, the process has not been investigated in depth. Since microgravity time is valuable and rare, the focus was set towards evaporation. Conceptually new drop towers are entering the market by now (Könemann et al. 2015; Overmeyer et al. 2017). They provide high repetition rates and do not rely on large vacuum systems. The GTB-Pro in Bremen (Gierse et al. 2017) will be the perfect platform to perform loading studies.

Even though this thesis did not present all the achievements made with potassium in the system, this branch of the experiment is as important. Since magneto-optical trapping was successful on ground, the next step has to be a demonstration in microgravity. This was hindered before by unstable temperature conditions on the laser platform. The situation was eased by remote accessible temperature controllers. The successful demonstration of a potassium MOT in microgravity will be followed by loading it into the dipole trap.

Atom interferometry will certainly be deferred to successful evaporation of potassium. Since interferometers with rubidium in microgravity have extensively been investigated in the last years (Müntinga et al. 2013), their basics can be considered as understood. For double species interferometry and interferometers based on fK temperatured atoms, allowing free evolution times on the order of seconds, the situation is totally different.

The Big Picture

Fundamental physics with ultra cold atoms in microgravity became a vibrant field of science over the last decade. The latest milestones set in this field are the first realization of a BEC in space (Becker et al. 2018) and the success to bring an ultracold atom facility aboard the international space station (Elliott et al. 2018). While the former is based on an atom chip and an additional dipole trap got dismissed due to complexity in the latter, the three next missions with ultracold atoms (BECCAL, MAUIS-2, MAIUS-3) will feature dipole traps in space (private communications). Their application will slightly differ from the realization in this thesis, not least because they are combined with compact magnetic traps.

These missions will anyway benefit from the findings in this thesis. The most important message is: dipole trapping in microgravity does not fundamentally differ from ground based operation and the contribution of effective trap depth is entirely understood. Of particular interest for future missions will be the application of optical delta kick collimation provided by *painted potentials*. The resulting expansion rates set an upper limit on the timescales of measurements, which is crucial for the estimation of accessible sensitivities.

Generally, the new tool of optical trapping in microgravity paves the way for a large number of new, or improved experiments. This is depicted in Figure 6.2, which is a modified schematic drawing of the PRIMUS milestones found in Figure 1.4. Possible alternative atom interferometry applications are listed in green, as well as several measurement options with AI, colored orange.

6. Outlook

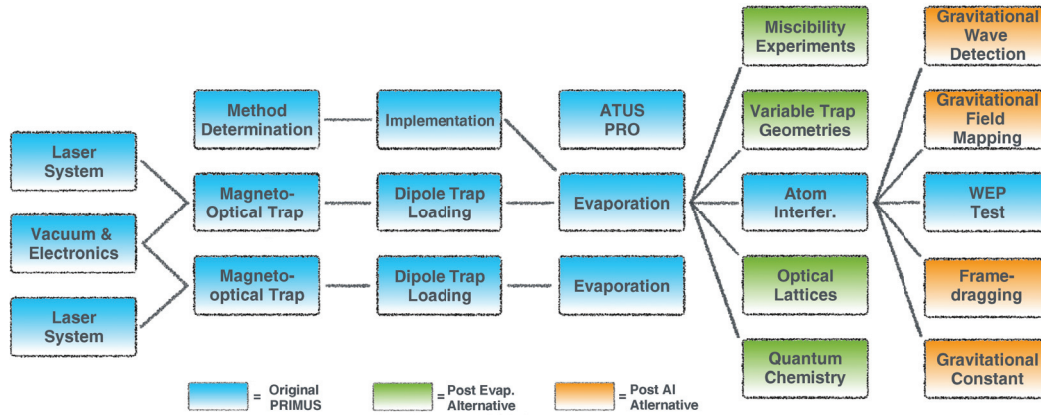


Figure 6.2

Modified schematic of Figure 1.4. Original PRIMUS milestones are represented by blue colored boxes (Rb and K). The table has been extended by possible experimental alternatives for an optically trapped ensemble in microgravity (green boxes). Furthermore the impact of an improved atom interferometer on gravity related experiments is shown (orange boxes).

The miscibility of BECs formed from different elements or isotopes, is based on their interspecies scattering length. By applying particular homogeneous magnetic fields these interactions can be almost arbitrarily tuned, using Feshbach resonances. These resonances can not be addressed in magnetic traps¹. Calculations predict shell-like structures where one BEC is surrounded by another one (Pu et al. 1998; Pattinson et al. 2013). Under the influence of gravity this has never been observed until now. The ability to optically trap ultracold atomic mixtures under microgravity allows for this kind of experiments.

Optical traps can flexibly be shaped without changing the experimental setup. While not addressed in this thesis, it is possible to apply optical potential where atoms are pushed away from high intensity areas. These so-called blue detuned traps offer the possibility to apply outer boundaries for atomic ensembles. One application is a box potential (Gaunt et al. 2013), simulating the textbook example in quantum theory. Investigating these without disturbing gravitational effects will lead to interesting physics.

One main application for optical traps on ground is the formation of optical lattices (Bloch 2005). These are used as solid state simulator (Gajda et al. 2015) or to drive Floquet-states (Eckardt 2017), for example. Experiments in microgravity would reveal the possibility of extremely shallow lattices providing high hopping rates between lattice sites.

The last chosen example is related to Feshbach resonances again. By tuning the interaction strength between collisional partners one can manipulate their bonding behavior and

¹Optically addressable Feshbach resonances have also been observed, but their practical application is limited (Nicholson et al. 2015).

form Feshbach molecules. They are of great importance in the field of quantum chemistry (Shoemaker et al. 1981; Ferlaino et al. 2009). Association and dissociation especially of weakly bound molecules are expected to be increased in a microgravity environment (D’Incao et al. 2017).

This impressive and still incomplete list of possible applications for dipole traps in microgravity reveals the importance of our experimental efforts. Furthermore, if optically delta kick collimation performs better than its magnetic counterpart, a whole new field of applications opens up.

Atom interferometry in weightlessness promises enhanced test sensitivities for several experiments. By delivering an improved, optically delta kick cooled, source for atom interferometers, the results of PRIMUS would affect all of them. In Figure 6.2 some gravity related examples are listed.

Space borne gravitational wave detection will enable the observation of frequency ranges that are inaccessible with earth bound devices. While the current, most promising, mission is based on optical interferometers (Amaro-Seoane et al. 2017), there are also suggestions on atom interferometer based satellite missions (Graham et al. 2017; Gao et al. 2018).

Mapping the gravitational field of the Earth reveals information e.g. about water and ice distribution on the planet. These important measurements are carried out by the Grace-FO mission, based on precise accelerometers. Next generation satellites will probably be equipped with atom interferometer based accelerators (Keeseey 2018). Optically prepared atoms could improve the sensitivity.

Cold atom sensors are not only able to sense accelerations, but can be precise rotation sensitive devices. In this manner, they could also be used to test the frame-dragging effect, also known as Lense-Thirring effect. It describes the very light spacetime dragging effect of rotating objects. Experimental evidence was collected in the Gravity Probe B mission, a more precise measurement could be based on cold atoms (Jentsch et al. 2004).

The last example in this chart represents an entire field of measurements. While precise tests of the gravitational constant with atom interferometry are possible in the laboratory (Prevedelli et al. 2014), the application of this technique in microgravity automatically increases the sensitivity. This is true for every single application of atom interferometry due to the increased long interrogation times.

Up to now, it is unclear whether the optical preparation of an atomic source for atom interferometry outperforms its magnetic counterpart. Anyway, the list of possible beneficiaries clarifies the urgency for this task. Furthermore it becomes obvious that this thesis is closed in itself, but just the beginning of a breath taking journey.

In the end I would like to emphasize once again, that all of our passionate endeavors for fundamental physical questions are producing robust and compact quantum sensors, the revolutionary future of measurement. I am looking forward to have a commercially available device in my household one day, based the heritage of me, my friends and my colleagues.

Bibliography

- Abend, S. et al. (2016). "Atom-chip fountain gravimeter". In: *Physical Review Letters* 117.20, pp. 1–7. DOI: 10.1103/PhysRevLett.117.203003 (cit. on p. 16).
- Adams, Charles S. et al. (1995). "Evaporative cooling in a crossed dipole trap". In: *Physical Review Letters* 74.18, pp. 3577–3580. DOI: 10.1103/PhysRevLett.74.3577 (cit. on p. 95).
- Aguilera, D. et al. (2014). "STE-QUEST - Test of the universality of free fall using cold atom interferometry". In: *Classical and Quantum Gravity* 31.15. DOI: 10.1088/0264-9381/31/15/159502 (cit. on p. 21).
- Ahmadi, P. et al. (2005). "Geometrical effects in the loading of an optical atom trap". In: *Physical Review A - Atomic, Molecular, and Optical Physics* 72.2, pp. 1–6. DOI: 10.1103/PhysRevA.72.023411 (cit. on pp. 55, 64, 101).
- Akatsuka, Tomoya et al. (2017). "Optically guided atom interferometer tuned to magic wavelength". In: *Applied Physics Express* 10.11, pp. 1–5. DOI: 10.7567/APEX.10.112501. arXiv: arXiv:1710.08706v1 (cit. on p. 18).
- Alt, Wolfgang (2004). "Optical control of single neutral atoms". PhD thesis, p. 132 (cit. on p. 53).
- Altschul, Brett et al. (2015). "Quantum tests of the Einstein Equivalence Principle with the STE-QUEST space mission". In: *Advances in Space Research* 55.1, pp. 501–524. DOI: 10.1016/j.asr.2014.07.014. arXiv: 1404.4307 (cit. on p. 21).
- Amaro-Seoane, Pau et al. (2017). *Laser Interferometer Space Antenna (LISA L3 mission proposal)*. arXiv: 1702.00786 (cit. on p. 119).
- Ammann, Hubert et al. (1997). "Delta kick cooling: A new method for cooling atoms". In: *Physical Review Letters* 78.11, pp. 2088–2091. DOI: 10.1103/PhysRevLett.78.2088 (cit. on pp. 18, 20).
- Andersen, Ulrik L et al. (2016). *30 years of squeezed light generation*. DOI: 10.1088/0031-8949/91/5/053001. arXiv: 1511.03250 (cit. on p. 15).
- Anderson, Mike H. et al. (1995). "Observation of Bose-Einstein condensation in a dilute atomic vapor". In: *Science* 269.JULY, pp. 198–201 (cit. on p. 15).

Bibliography

- Arnold, K. J. et al. (2011). "All-optical Bose-Einstein condensation in a 1.06 μm dipole trap". In: *Optics Communications* 284.13, pp. 3288–3291. doi: 10.1016/j.optcom.2011.03.008. arXiv: arXiv:1101.1140v2 (cit. on p. 53).
- Ashkin, A. (1970). "Acceleration and Trapping of Particles by Radiation Pressure". In: *Physical Review Letters* 24.4, pp. 156–159. doi: 10.1103/PhysRevLett.24.156 (cit. on p. 41).
- Ashkin, A. and J. Dziedzic (Mar. 1987). "Optical trapping and manipulation of viruses and bacteria". In: *Science* 235.4795, pp. 1517–1520. doi: 10.1126/science.3547653 (cit. on p. 41).
- Ashkin, Arthur (Dec. 2006). *Optical Trapping and Manipulation of Neutral Particles Using Lasers*. WORLD SCIENTIFIC. doi: 10.1142/4208 (cit. on p. 64).
- Barrett, Brynle, L. Antoni-Micollier, et al. (Aug. 2015). "Correlative methods for dual-species quantum tests of the weak equivalence principle". In: *New Journal of Physics* 17.8, p. 085010. doi: 10.1088/1367-2630/17/8/085010. arXiv: 1503.08423 (cit. on p. 16).
- Barrett, Brynle, Laura Antoni-Micollier, et al. (2016). "Dual Matter-Wave Inertial Sensors in Weightlessness". In: pp. 1–11. doi: 10.1038/ncomms13786. arXiv: 1609.03598 (cit. on p. 19).
- Barrett, Brynle, I. Chan, et al. (2011). "Atom-interferometric techniques for measuring uniform magnetic field gradients and gravitational acceleration". In: *Physical Review A - Atomic, Molecular, and Optical Physics* 84.6. doi: 10.1103/PhysRevA.84.063623. arXiv: 1104.4577 (cit. on p. 16).
- Barrett, M D et al. (2001). "All-optical formation of an atomic Bose-Einstein condensate." In: *Physical review letters* 87.1, p. 010404. doi: 10.1103/PhysRevLett.87.010404. arXiv: 0106027 [cond-mat] (cit. on p. 53).
- Becker, Dennis et al. (2018). "Space-borne Bose-Einstein condensation for precision interferometry". In: *Nature*, pp. 4–9. doi: 10.1016/j.tim.2013.07.003. arXiv: 1806.06679 (cit. on pp. 19, 117).
- Biedermann, G. W. et al. (2017). "Atom Interferometry in a Warm Vapor". In: *Physical Review Letters* 118.16, pp. 4–8. doi: 10.1103/PhysRevLett.118.163601. arXiv: 1610.02451 (cit. on p. 18).
- Bird, Graeme (1994). *Molecular Gas Dynamics and Direct Simulation of Gas Flows*, p. 458. doi: 10.1016/0042-207X(96)80021-2 (cit. on p. 80).
- Bird, Graeme (2007). "Sophisticated DSMC". In: *DSMC07 meeting*, pp. 1–49 (cit. on p. 82).

- Bize, S. et al. (2005). "Cold atom clocks and applications". In: *Journal of Physics B: Atomic, Molecular and Optical Physics* 38.9. DOI: 10.1088/0953-4075/38/9/002. arXiv: 0502117 [physics] (cit. on p. 15).
- Bjorklund, G. C. et al. (1983). "Frequency modulation (FM) spectroscopy". In: *Applied Physics B Photophysics and Laser Chemistry* 32.3, pp. 145–152. DOI: 10.1007/BF00688820 (cit. on p. 25).
- Blanke, Nena (2016). "Aufbau und Charakterisierung von Lasersystemen zur Kühlung und Manipulation von Kalium in einem Fallturmexperiment". PhD thesis (cit. on p. 25, 43).
- Bloch, Immanuel (2005). "Ultracold quantum gases in optical lattices". In: *Nature Physics* 1.1, pp. 23–30. DOI: 10.1038/nphys138 (cit. on p. 118).
- Bose, Satyendranath (1924). "Plancks Gesetz und Lichtquantenhypothese". In: *Zeitschrift für Physik* 26.1, pp. 178–181. DOI: 10.1007/BF01327326 (cit. on p. 15).
- Bourouis, Riad (2007). "Optical Realization of Bose-Einstein Condensation in a Single CO 2 Laser Beam". PhD thesis (cit. on p. 75).
- Bradley, C. C. et al. (1995). "Evidence of Bose-Einstein condensation in an atomic gas with attractive interactions". In: *Physical Review Letters* 75.9, pp. 1687–1690. DOI: 10.1103/PhysRevLett.75.1687. arXiv: 0507204 [quant-ph] (cit. on p. 15).
- Brantut, J. P. et al. (2008). "Light-shift tomography in an optical-dipole trap for neutral atoms". In: *Physical Review A - Atomic, Molecular, and Optical Physics* 78.3, pp. 78–81. DOI: 10.1103/PhysRevA.78.031401. arXiv: 0807.3672 (cit. on p. 55).
- Brink, D. M. et al. (2006). "Majorana spin-flip transitions in a magnetic trap". In: September, pp. 1–4. DOI: 10.1103/PhysRevA.74.035401. arXiv: 0610135 [quant-ph] (cit. on p. 52).
- Brooker, Geoffrey (2007). *Modern classical optics*. Oxford: Oxford Univ. Press (cit. on p. 48).
- Burke, James P et al. (1997). "Impact of the Rb87 singlet scattering length on suppressing inelastic collisions". In: *Phys. Rev. A* 55.4, R2511–R2514. DOI: 10.1103/PhysRevA.55.R2511 (cit. on p. 88).
- Burt, E. A. et al. (1997). "Coherence, correlations, and collisions: What one learns about bose-einstein condensates from their decay". In: *Physical Review Letters* 79.3, pp. 337–340. DOI: 10.1103/PhysRevLett.79.337 (cit. on p. 72).
- Canuel, B. et al. (2006). "Six-axis inertial sensor using cold-atom interferometry". In: *Physical Review Letters* 97.1, pp. 1–4. DOI: 10.1103/PhysRevLett.97.010402. arXiv: 0604061 [physics] (cit. on p. 16).

Bibliography

- Castin, Y et al. (1996). "Bose-Einstein Condensates in Time Dependent Traps". In: *Physical Review Letters* 77.27, pp. 1–5 (cit. on p. 20).
- Cennini, G. et al. (2003). "Bose-Einstein condensation in a CO₂-laser optical dipole trap". In: *Applied Physics B: Lasers and Optics* 77.8, pp. 773–779. DOI: 10.1007/s00340-003-1333-1 (cit. on p. 53).
- Chin, Cheng et al. (2010). "Feshbach resonances in ultracold gases". In: *Reviews of Modern Physics* 82.2, pp. 1225–1286. DOI: 10.1103/RevModPhys.82.1225. arXiv: 0812.1496 (cit. on p. 102).
- Chisholm, C S et al. (2018). "A three-dimensional steerable optical tweezer system for ultracold atoms". In: arXiv: arXiv:1805.10574v1 (cit. on p. 53).
- Chu, Steven, J E Bjorkholm, et al. (1986). "Experimental observation of optically trapped atoms". In: *Phys. Rev. Lett.* 57, p. 314 (cit. on pp. 41, 47).
- Chu, Steven, L. Hollberg, et al. (1985). "Three-Dimensional Viscous Confinement and Cooling of Atoms by Resonance Radiation Pressure". In: *Physical Review Letters* 55.1 (cit. on p. 62).
- Cladé, Pierre et al. (2009). "Large momentum beam splitter using Bloch oscillations". In: *Physical Review Letters* 102.24, pp. 1–4. DOI: 10.1103/PhysRevLett.102.240402. arXiv: arXiv:0903.3511v1 (cit. on p. 17).
- Clément, J. F. et al. (2009). "All-optical runaway evaporation to Bose-Einstein condensation". In: *Physical Review A - Atomic, Molecular, and Optical Physics* 79.6, pp. 1–4. DOI: 10.1103/PhysRevA.79.061406. arXiv: 0903.2745 (cit. on p. 53).
- Cline, R. A. et al. (1994). "Spin relaxation of optically trapped atoms by light scattering". In: *Optics Letters* 19.3, p. 207. DOI: 10.1364/OL.19.000207 (cit. on p. 72).
- Cohen-Tannoudji, Claude N. et al. (1990). "New Mechanisms for Laser Cooling". In: *Physics Today* 43.10, pp. 33–40. DOI: 10.1063/1.881239 (cit. on p. 62).
- Colzi, Giacomo et al. (2018). "Production of large Bose-Einstein condensates in a magnetic-shield-compatible hybrid trap". In: *Physical Review A* 97.5, pp. 1–7. DOI: 10.1103/PhysRevA.97.053625. arXiv: 1803.08814 (cit. on p. 105).
- Comparat, D. et al. (Apr. 2006). "Optimized production of large Bose-Einstein condensates". In: *Physical Review A* 73.4, p. 043410. DOI: 10.1103/PhysRevA.73.043410 (cit. on p. 52).
- Cooper, C. J. et al. (1994). "The temperature of atoms in a magneto-optical trap". In: *Epl* 28.6, pp. 397–402. DOI: 10.1209/0295-5075/28/6/004 (cit. on p. 57).

- Cornell, Eric A. et al. (1999). “Experiments in dilute atomic Bose- Einstein condensation”. In: *Bose-Einstein Condensation in Atomic Gases*. Ed. by M Inguscio et al. Ios Pr Inc (cit. on p. 71).
- Cronin, Alexander D. et al. (2009). “Optics and interferometry with atoms and molecules”. In: *Reviews of Modern Physics* 81.3, pp. 1051–1129. doi: 10.1103/RevModPhys.81.1051. arXiv: 0712.3703 (cit. on p. 15).
- D’Incao, J. P. et al. (2017). “Enhanced association and dissociation of heteronuclear Feshbach molecules in a microgravity environment”. In: *Physical Review A* 95.1, pp. 1–10. doi: 10.1103/PhysRevA.95.012701. arXiv: 1607.04650 (cit. on p. 119).
- Dalibard, J. (1988). “Laser cooling of an optically thick gas: The simplest radiation pressure trap?” In: *Optics Communications* 68.3, pp. 203–208. doi: 10.1016/0030-4018(88)90185-X (cit. on p. 41).
- Dalibard, J. and Claude N. Cohen-Tannoudji (1985). “Dressed-atom approach to atomic motion in laser light: the dipole force revisited”. In: *Journal of the Optical Society of America B* 2.11, p. 1707. doi: 10.1364/JOSAB.2.001707 (cit. on p. 53).
- Damjanic, Marcin (2013). *Thulium fiber laser manual* (cit. on p. 34).
- Damour, Thibault (1994). “The string dilation and a least coupling principle”. In: *Nuclear Physics, Section B* 423.2-3, pp. 532–558. doi: 10.1016/0550-3213(94)90143-0. arXiv: 9401069 [hep-th] (cit. on p. 21).
- Damour, Thibault (1996). “Testing the equivilant principle: why and how.pdf”. In: *Class. Quantum Grav* 13, A33–A41 (cit. on p. 21).
- Damour, Thibault et al. (2002). “Runaway dilaton and equivalence principle violations”. In: *Physical Review Letters* 89.8, pp. 081601/1–081601/4. doi: 10.1103/PhysRevLett.89.081601. arXiv: 0204094 [gr-qc] (cit. on p. 21).
- Davidson, Nir et al. (1995). “Long Atomic Coherence Times in an Optical Dipole Trap”. In: *Physical review letters* 74.8, pp. 1335–1339. doi: PhysRevLett.74.1311 (cit. on p. 47).
- Davis, J. P. et al. (2008). “A proposal for a gradient magnetometer atom interferometer”. In: *Journal of Modern Optics* 55.19-20, pp. 3173–3185. doi: 10.1080/09500340802468633 (cit. on p. 16).
- Davis, K. B., M. O. Mewes, M. R. Andrews, et al. (1995). “Bose-Einstein condensation in a gas of sodium atoms”. In: *Physical Review Letters* 75.22, pp. 3969–3973. doi: 10.1103/PhysRevLett.75.3969. arXiv: 9604005 [quant-ph] (cit. on pp. 15, 104).

Bibliography

- Davis, K. B., M. O. Mewes, and W. Ketterle (1995). "An analytical model for evaporative cooling of atoms". In: *Applied Physics B Laser and Optics* 60.2-3, pp. 155–159. doi: 10.1007/BF01135857 (cit. on p. 77).
- De Angelis, M. et al. (2009). "Precision gravimetry with atomic sensors". In: *Measurement Science and Technology* 20.2. doi: 10.1088/0957-0233/20/2/022001. arXiv: 15334406 (cit. on p. 16).
- DeCarvalho, Robert et al. (2004). "Evaporative cooling at low trap depth". In: *Physical Review A - Atomic, Molecular, and Optical Physics* 70.5 B. doi: 10.1103/PhysRevA.70.053409 (cit. on p. 77).
- DePue, Marshall T. et al. (1999). "Unity occupation of sites in a 3D optical lattice". In: *Physical Review Letters* 82.11, pp. 2262–2265. doi: 10.1103/PhysRevLett.82.2262 (cit. on p. 66).
- Dickerson, Susannah M. et al. (2013). "Multi-axis inertial sensing with long-time point source atom interferometry". In: *Physical Review Letters* 111.8, pp. 1–5. doi: 10.1103/PhysRevLett.111.083001. arXiv: 1305.1700 (cit. on p. 18).
- Dieckmann, K. et al. (Nov. 1998). "Two-dimensional magneto-optical trap as a source of slow atoms". In: *Physical Review A* 58.5, pp. 3891–3895. doi: 10.1103/PhysRevA.58.3891 (cit. on pp. 27, 29).
- Diekmann, Robin et al. (2016). "Nanoscopy of bacterial cells immobilized by holographic optical tweezers". In: *Nature Communications* 7. doi: 10.1038/ncomms13711 (cit. on p. 41).
- Dienerowitz, Maria et al. (Sept. 2008). "Optical manipulation of nanoparticles: a review". In: *Journal of Nanophotonics* 2.1, p. 021875. doi: 10.1117/1.2992045 (cit. on p. 41).
- Donnelly, Denis et al. (2005). "Symplectic integrators: An introduction". In: *American Journal of Physics* 73.10, pp. 938–945. doi: 10.1119/1.2034523 (cit. on p. 81).
- Dowling, Jonathan P. et al. (2003). "Quantum technology: The second quantum revolution". In: *Philosophical Transactions of the Royal Society A: Mathematical, Physical and Engineering Sciences* 361.1809, pp. 1655–1674. doi: 10.1098/rsta.2003.1227. arXiv: 0206091 [quant-ph] (cit. on p. 15).
- Doyle, John M. (1991). "Energy Distribution Measurements of Magnetically Trapped Spin Polarized Atomic Hydrogen: Evaporative Cooling and Surface Sticking". PhD thesis (cit. on pp. 76, 78).
- Du, Shengwang (2005). "Atom-chip Bose-Einstein condensation in a portable vacuum cell". PhD thesis. doi: 10.1103/PhysRevA.70.053606 (cit. on p. 52).

- Du, Shengwang et al. (2004). "Atom-chip Bose-Einstein condensation in a portable vacuum cell". In: *Physical Review A - Atomic, Molecular, and Optical Physics* 70.5 B, pp. 5–8. DOI: 10.1103/PhysRevA.70.053606 (cit. on p. 52).
- Dutta, I. et al. (2016). "Continuous Cold-Atom Inertial Sensor with 1 nrad/sec Rotation Stability". In: *Physical Review Letters* 116.18, pp. 1–5. DOI: 10.1103/PhysRevLett.116.183003. arXiv: 1604.00940 (cit. on p. 16).
- Eckardt, André (2017). "Colloquium: Atomic quantum gases in periodically driven optical lattices". In: *Reviews of Modern Physics* 89.1, pp. 1–30. DOI: 10.1103/RevModPhys.89.011004 (cit. on p. 118).
- Egorov, M. et al. (2013). "Measurement of s-wave scattering lengths in a two-component Bose-Einstein condensate". In: *Physical Review A - Atomic, Molecular, and Optical Physics* 87.5, pp. 1–10. DOI: 10.1103/PhysRevA.87.053614. arXiv: 1204.1591 (cit. on p. 71).
- Einstein, Albert (1924). "Quantentheorie des einatomigen idealen Gases". In: *Sitzungsbericht Kgl. Preuss. Akad. Wiss.* DOI: 10.1002/3527608958.ch27. arXiv: 1707.04192 (cit. on p. 15).
- Elder, Benjamin et al. (2016). "Chameleon dark energy and atom interferometry". In: *Physical Review D* 94.4, pp. 1–15. DOI: 10.1103/PhysRevD.94.044051. arXiv: 1603.06587 (cit. on p. 21).
- Elliott, Ethan R. et al. (2018). "NASA's cold atom lab (CAL): System development and ground test status". In: *npj Microgravity* 4.1, pp. 1–7. DOI: 10.1038/s41526-018-0049-9 (cit. on p. 117).
- Engler, H. et al. (2000). "Very long storage times and evaporative cooling of cesium atoms in a quasidelectrostatic dipole trap". In: *Physical Review A - Atomic, Molecular, and Optical Physics* 62.3, pp. 1–4. DOI: 10.1103/PhysRevE.63.031402. arXiv: 0003075 [physics] (cit. on p. 67).
- Fayet, Pierre (2017). "The light U boson as the mediator of a new force, coupled to a combination of Q,B,L and dark matter". In: *European Physical Journal C* 77.1. DOI: 10.1140/epjc/s10052-016-4568-9. arXiv: 1611.05357 (cit. on p. 21).
- Ferlaino, Francesca et al. (2009). "Ultracold Feshbach Molecules". In: *Cold molecules: theory, experiment, applications.* arXiv: 0809.3920 (cit. on p. 119).
- Feshbach, H. (1958). "Unified theory of nuclear reactions". In: *Annals of Physics* 5.4, pp. 357–390. DOI: 10.1016/0003-4916(58)90007-1 (cit. on p. 102).
- Friebel, S. et al. (1998). "CO₂-laser optical lattice with cold rubidium atoms". In: *Physical Review A* 57.1, R20–R23. DOI: 10.1103/PhysRevA.57.R20 (cit. on p. 67).

Bibliography

- Gaaloul, Naceur et al. (2006). "Theoretical study of a cold-atom beam splitter". In: *Physical Review A - Atomic, Molecular, and Optical Physics* 74.2, pp. 1–9. DOI: 10.1103/PhysRevA.74.023620. arXiv: 0601137 [quant-ph] (cit. on p. 55).
- Gajda, Mariusz et al. (2015). "Non-standard Hubbard models in optical lattices: a review". In: *Reports on Progress in Physics* 78.6, p. 066001. DOI: 10.1088/0034-4885/78/6/066001 (cit. on p. 118).
- Gallagher, Alan et al. (1989). "Exoergic collisions of cold Na/Na". In: *Physical Review Letters* 63.9, pp. 957–960. DOI: 10.1103/PhysRevLett.63.957 (cit. on p. 59).
- Ganske, Sven (2012). "Entwicklung einer Vakuumkammer für die differentielle Atominterferometrie". PhD thesis (cit. on p. 103).
- Gao, Dong Feng et al. (2018). "Atomic Interferometric Gravitational-Wave Space Observatory (AIGSO)". In: *Communications in Theoretical Physics* 69.1, pp. 37–42. DOI: 10.1088/0253-6102/69/1/37 (cit. on p. 119).
- Gaunt, Alexander L. et al. (2013). "Bose-Einstein Condensation of Atoms in a Uniform Potential". In: *Physical Review Letters* 110.20, pp. 1–5. DOI: 10.1103/physrevlett.110.200406 (cit. on p. 118).
- Gehm, M. E. et al. (1998). "Dynamics of noise-induced heating in atom traps". In: *Physical Review A - Atomic, Molecular, and Optical Physics* 58.5, pp. 3914–3921. DOI: 10.1103/PhysRevA.58.3914 (cit. on p. 71).
- Gensemer, S et al. (1997). "Trap-loss collisions of Rb85 and Rb87: Dependence on trap parameters". In: *Physical Review A* 56.5, pp. 4055–4063. DOI: 10.1103/PhysRevA.56.4055 (cit. on p. 59).
- Gierse, Andreas et al. (Oct. 2017). "A Fast and Self-Acting Release-Caging-Mechanism for Actively Driven Drop Tower Systems". In: *Microgravity Science and Technology* 29.5, pp. 403–414. DOI: 10.1007/s12217-017-9560-y (cit. on p. 117).
- Göklü, Ertan et al. (2008). "Metric fluctuations and the weak equivalence principle". In: *Classical and Quantum Gravity* 25.10. DOI: 10.1177/019263658106544322. arXiv: arXiv:0801.4553v4 (cit. on p. 21).
- Graham, Peter W et al. (2017). "Mid-band gravitational wave detection with precision atomic sensors". In: arXiv: 1711.02225 (cit. on p. 119).
- Grimm, Rudolf et al. (1999). "Optical Dipole Traps for Neutral Atoms". In: arXiv: 9902072v1 [arXiv:physics] (cit. on pp. 45, 47, 49, 53, 71, 73).

- Gröbner, Michael et al. (2017). “Degenerate Raman sideband cooling of K 39”. In: *Physical Review A* 95.3, pp. 1–7. doi: 10.1103/PhysRevA.95.033412. arXiv: 1612.02309 (cit. on p. 66).
- Gross, Noam et al. (2008). “All-optical production of L7 Bose-Einstein condensation using Feshbach resonances”. In: *Physical Review A* 77.2, p. 023604. doi: 10.1103/PhysRevA.77.023604. arXiv: 0712.0717 (cit. on p. 103).
- Grzeschik, Christoph (2017). “Experiments with Bose-Einstein Condensates in Microgravity”. PhD thesis. Humboldt-Universität zu Berlin. doi: <http://dx.doi.org/10.18452/18037> (cit. on pp. 27, 36).
- Gustavson, T L et al. (1997). “Precision Rotation Measurements with an Atom Interferometer Gyroscope”. In: *Physical Review Letters* 78.11, pp. 2046–2049. doi: 10.1103/PhysRevLett.78.2046 (cit. on p. 16).
- Hamann, S. E. et al. (1998). “Resolved-sideband raman cooling to the ground state of an optical lattice”. In: *Physical Review Letters* 80.19, pp. 4149–4152. doi: 10.1103/PhysRevLett.80.4149. arXiv: 9801025 [quant-ph] (cit. on p. 65).
- Han, Dian Jiun et al. (2000). “3D Raman sideband cooling of cesium atoms at high density”. In: *Physical Review Letters* 85.4, pp. 724–727. doi: 10.1103/PhysRevLett.85.724 (cit. on p. 66).
- Harsono, Andrian (2006). “Dipole trapping and manipulation of ultra-cold atoms Dipole trapping and manipulation of ultra-cold”. PhD thesis, p. 127 (cit. on p. 102).
- Härter, Arne et al. (2013). “Shedding Light on Three-Body Recombination in an Ultracold Atomic Gas”. In: arXiv: 1301.5518 (cit. on p. 72).
- Haslinger, Philipp et al. (2018). “Attractive force on atoms due to blackbody radiation”. In: *Nature Physics* 14.3, pp. 257–260. doi: 10.1038/s41567-017-0004-9. arXiv: 1704.03577 (cit. on p. 20).
- Hebestreit, Erik et al. (2018). “Sensing Static Forces with Free-Falling Nanoparticles”. In: *Physical Review Letters* 121.6, pp. 1–5. doi: 10.1103/PhysRevLett.121.063602. arXiv: 1801.01169 (cit. on p. 41).
- Heinzen, D. J. et al. (1990). “Quantum-limited cooling and detection of radio-frequency oscillations by laser-cooled ions”. In: *Physical Review A* 42.5, pp. 2977–2994. doi: 10.1103/PhysRevA.42.2977. arXiv: arXiv:1011.1669v3 (cit. on p. 65).
- Henderson, K. et al. (2009). “Experimental demonstration of painting arbitrary and dynamic potentials for Bose-Einstein condensates”. In: *New Journal of Physics* 11. doi: 10.1088/1367-2630/11/4/043030. arXiv: 0902.2171 (cit. on p. 101).

Bibliography

- Herr, Waldemar (2013). "Eine kompakte Quelle quantenentarteter Gase hohen Flusses für die Atominterferometrie unter Schwerelosigkeit". PhD thesis (cit. on p. 34).
- Hilton, A. P. et al. (2018). "High-efficiency cold-atom transport into a waveguide trap". In: *Physical Review Applied* 10.4, pp. 1–9. DOI: 10.1103/PhysRevApplied.10.044034. arXiv: arXiv:1802.05396v2 (cit. on p. 18).
- Hogan, Jason M. et al. (2015). "Matter Wave Lensing to Picokelvin Temperatures". In: *Physical Review Letters* 114.14, pp. 1–5. DOI: 10.1103/physrevlett.114.143004 (cit. on p. 18).
- Hohensee, Michael A. et al. (2013). "Equivalence principle and bound kinetic energy". In: *Physical Review Letters* 111.15, pp. 1–5. DOI: 10.1103/PhysRevLett.111.151102. arXiv: 1308.2936 (cit. on p. 21).
- Holland, M et al. (1996). "Trajectory simulation of kinetic equations for classical systems". In: *Quantum Semiclass Opt* 8.3, p. 571. DOI: 10.1088/1355-5111/8/3/019 (cit. on p. 77).
- Hu, Jiazhong et al. (2017). "Creation of a Bose-condensed gas of rubidium 87 by laser cooling". In: *Science (New York, N.Y.)* 358.6366, pp. 1078–1080. DOI: 10.1126/science.aan5614. arXiv: 1705.03421 (cit. on p. 65).
- Hughes, Richard J. et al. (1995). "Quantum cryptography". In: *Contemporary Physics* 36.3, pp. 149–163. DOI: 10.1080/00107519508222149. arXiv: 0101098v2 [arXiv:quant-ph] (cit. on p. 15).
- Hung, Chen Lung et al. (2008). "Accelerating evaporative cooling of atoms into Bose-Einstein condensation in optical traps". In: *Physical Review A - Atomic, Molecular, and Optical Physics* 78.1, pp. 1–4. DOI: 10.1103/PhysRevA.78.011604. arXiv: 0804.0060v1 (cit. on p. 86).
- Hung, Chen-Lung (2011). "In situ probing of two-dimensional quantum gases". PhD thesis. THE UNIVERSITY OF CHICAGO, pp. 1–216 (cit. on p. 106).
- Hung, Weilun et al. (2015). "Storage time of cold Rb atoms in an optical dipole trap formed by a multimode fiber laser". In: *Journal of the Optical Society of America B* 32.5, pp. 32–36. DOI: 10.1364/JOSAB.32.000B32 (cit. on pp. 53, 64, 72).
- Ivanov, Vladyslav Viktorovych (2007). "Cold atoms : modified radiative properties and evaporative cooling from optical traps". PhD thesis. University of Amsterdam (cit. on p. 41).
- Jackson, J. D. (1999). *Classical Electrodynamics*. 3rd. New York, NY (cit. on p. 46).
- Jackson, Stuart D. et al. (2007). "Application and development of high-power and highly efficient silica-based fiber lasers operating at 2 μm ". In: *IEEE Journal on Selected Topics in Quantum Electronics* 13.3, pp. 567–572. DOI: 10.1109/JSTQE.2007.896087 (cit. on p. 33).

- Jenkin, D. L. et al. (2011). "Bose-Einstein condensation of 87Rb in a levitated crossed dipole trap". In: *European Physical Journal D* 65.1-2, pp. 11–18. doi: 10.1140/epjd/e2011-10720-5. arXiv: 1104.0495 (cit. on p. 106).
- Jentsch, C. et al. (2004). "HYPER: A satellite mission in fundamental physics based on high precision atom interferometry". In: *General Relativity and Gravitation* 36.10 SPEC.ISS. Pp. 2197–2221. doi: 10.1023/B:GERG.0000046179.26175.f8 (cit. on p. 119).
- Kagan, Y et al. (1985). *Effect of Bose condensation on inelastic processes in gases* (cit. on p. 72).
- Karcher, R et al. (2018). "Improving the accuracy of atom interferometers with ultracold sources". In: pp. 1–5. arXiv: 1804.04909 (cit. on p. 17).
- Kasevich, Mark A. and S Chu (1992). "Measurement of the Gravitational Acceleration of an Atom with a Light-Pulse Atom Interferometer". In: *Applied Physics B* 54, pp. 321–332 (cit. on p. 17).
- Kasevich, Mark A., David S. Weiss, et al. (May 1991). "Atomic velocity selection using stimulated Raman transitions". In: *Physical Review Letters* 66.18, pp. 2297–2300. doi: 10.1103/PhysRevLett.66.2297 (cit. on p. 18).
- Keesey, Lori (2018). *Team creates and demonstrates first quantum sensor for satellite gravimetry* (cit. on p. 119).
- Kerman, Andrew J. et al. (2000). "Beyond optical molasses: 3D raman sideband cooling of atomic cesium to high phase-space density". In: *Physical Review Letters* 84.3, pp. 439–442. doi: 10.1103/PhysRevLett.84.439 (cit. on p. 66).
- Ketterle, W., K. B. Davis, et al. (1993). "High densities of cold atoms in a dark spontaneous-force optical trap". In: *Physical Review Letters* 70.15, pp. 2253–2256. doi: 10.1103/PhysRevLett.70.2253 (cit. on p. 58).
- Ketterle, W. and N.J. Van Druten (1996). *Evaporative cooling of trapped atoms*. doi: 10.1016/S1049-250X(08)60101-9 (cit. on pp. 70, 73, 84, 85).
- Khoury, Justin et al. (2004). "Chameleon fields: Awaiting surprises for tests of gravity in space". In: *Physical Review Letters* 93.17, pp. 1–4. doi: 10.1103/PhysRevLett.93.171104. arXiv: 0309300 [astro-ph] (cit. on p. 21).
- Kimura, M. et al. (2015). "Testing the Weak Equivalence Principle with an antimatter beam at CERN". In: *Journal of Physics: Conference Series* 631.1. doi: 10.1088/1742-6596/631/1/012047 (cit. on p. 21).

Bibliography

- Kinoshita, Toshiya et al. (2005). "All-optical Bose-Einstein condensation using a compressible crossed dipole trap". In: *Physical Review A - Atomic, Molecular, and Optical Physics* 71.1, pp. 1–4. DOI: 10.1103/PhysRevA.71.011602 (cit. on pp. 53, 98, 99).
- Könemann, Thorben et al. (2015). "Concept for a next-generation drop tower system". In: *Advances in Space Research* 55.6, pp. 1728–1733. DOI: 10.1016/j.asr.2014.12.028 (cit. on p. 117).
- Kopitzki, K. (1993). *Einführung in die Festkörperphysik* (cit. on p. 46).
- Kostelecký, V. Alan et al. (2009). "Prospects for large relativity violations in matter-gravity couplings". In: *Physical Review Letters* 102.1, pp. 1–4. DOI: 10.1103/PhysRevLett.102.010402. arXiv: 0810.1459 (cit. on p. 21).
- Kubelka-Lange, André (2017). "Entwicklung einer hocheffektiven Magnetfeldabschirmung für die Forschungsraketenmission MAIUS-1". PhD thesis. Uni Bremen (cit. on p. 28).
- Kubelka-Lange, André et al. (2016). "A three-layer magnetic shielding for the MAIUS-1 mission on a sounding rocket". In: *Review of Scientific Instruments* 87.6. DOI: 10.1063/1.4952586 (cit. on p. 28).
- Kulas, Sascha (2016). "Realisierung eines kompakten Laborsystems zur Durchführung atomoptischer Fallturmexperimente". PhD thesis (cit. on pp. 23, 25, 36, 62).
- Kuppens, SJM et al. (2000). "Loading an optical dipole trap". In: *Physical review A* 62.June, pp. 1–13 (cit. on pp. 55, 56, 60).
- Ladd, T. D. et al. (2010). "Quantum computers". In: *Nature* 464.7285, pp. 45–53. DOI: 10.1038/nature08812. arXiv: 1009.2267 (cit. on p. 15).
- Landini, M., S. Roy, L. Carcagní, et al. (Oct. 2011). "Sub-Doppler laser cooling of potassium atoms". In: *Physical Review A* 84.4, pp. 1–6. DOI: 10.1103/PhysRevA.84.043432 (cit. on p. 84).
- Landini, M., S. Roy, G. Roati, et al. (Sept. 2012). "Direct evaporative cooling of 39K atoms to Bose-Einstein condensation". In: *Physical Review A* 86.3, p. 033421. DOI: 10.1103/PhysRevA.86.033421 (cit. on pp. 52, 64, 84).
- Lang, Matthew J. et al. (2003). "Resource Letter: LBOT-1: Laser-based optical tweezers". In: *American Journal of Physics* 71.3, pp. 201–215. DOI: 10.1119/1.1532323 (cit. on p. 41).
- Larmor, J. (1897). "LXIII. On the theory of the magnetic influence on spectra; and on the radiation from moving ions". In: *Philosophical Magazine Series 5* 44.271, pp. 503–512. DOI: 10.1080/14786449708621095 (cit. on p. 46).

- Lauber, T et al. (Oct. 2011). "Optimized Bose-Einstein-condensate production in a dipole trap based on a 1070-nm multifrequency laser: Influence of enhanced two-body loss on the evaporation process". In: *Physical Review A* 84.4, p. 043641. DOI: 10.1103/PhysRevA.84.043641 (cit. on pp. 64, 72).
- Lett, Paul D. et al. (1988). "Observation of atoms laser cooled below the doppler limit". In: *Physical Review Letters* 61.2, pp. 169–172. DOI: 10.1103/PhysRevLett.61.169 (cit. on pp. 58, 62).
- Lévêque, T. et al. (2009). "Enhancing the area of a Raman atom interferometer using a versatile double-diffraction technique". In: *Physical Review Letters* 103.8, pp. 1–4. DOI: 10.1103/PhysRevLett.103.080405. arXiv: 0904.3266 (cit. on p. 23).
- Liao, Guan-Bo et al. (2017). "Optimization of a crossed optical dipole trap for loading and confining laser-cooled atoms". In: *Journal of the Optical Society of America B* 34.4, p. 869. DOI: 10.1111/j.0962-1075.2004.00484.x (cit. on p. 98).
- Lin, Y. J. et al. (2009). "Rapid production of R 87 b Bose-Einstein condensates in a combined magnetic and optical potential". In: *Physical Review A - Atomic, Molecular, and Optical Physics* 79.6, pp. 1–8. DOI: 10.1103/PhysRevA.79.063631. arXiv: 0904.3314 (cit. on p. 53).
- Liu, Liang et al. (2018). "In-orbit operation of an atomic clock based on laser-cooled 87Rb atoms". In: *Nature Communications* 9.1. DOI: 10.1038/s41467-018-05219-z (cit. on p. 18).
- Lorentz, H. A. (1906). *Versuch einer Theorie der Electricischen und Optischen Erscheinungen in Bewegten Körpern*. Teubner (cit. on p. 46).
- Louchet-Chauvet, Anne et al. (2011). "The influence of transverse motion within an atomic gravimeter". In: *New Journal of Physics* 13.6, p. 065025. DOI: 10.1088/1367-2630/13/6/065025 (cit. on p. 62).
- Luiten, O. et al. (1996). "Kinetic theory of the evaporative cooling of a trapped gas". In: *Physical Review A* 53.1, pp. 381–389. DOI: 10.1103/PhysRevA.53.381 (cit. on p. 78).
- Lvovsky, A. I. (2016). "Squeezed light". In: *Scientific Foundations, Technology and Applications*, pp. 1–21. arXiv: arXiv:1401.4118v2 (cit. on p. 15).
- Majorana, Ettore (1932). "Atomi orientati in campo magnetico variabile". In: *Nuovo Cimento* 9.43. DOI: 10.1007/978-3-540-48095-2_7 (cit. on p. 52).
- Marchant, A. L. et al. (2012). "Bose-Einstein condensation of 85Rb by direct evaporation in an optical dipole trap". In: *Physical Review A - Atomic, Molecular, and Optical Physics* 85.5, pp. 1–5. DOI: 10.1103/PhysRevA.85.053647. arXiv: 1203.6598 (cit. on p. 104).

Bibliography

- Marojević, Želimir et al. (2016). "ATUS-PRO: A FEM-based solver for the time-dependent and stationary Gross-Pitaevskii equation". In: *Computer Physics Communications* 202, pp. 216–232. doi: 10.1016/j.cpc.2015.12.004. arXiv: 1506.07710 (cit. on p. 22).
- Marsaglia, G. et al. (1964). "A Convenient Method for Generating Normal Variables". In: *SIAM Review* 6.3 (cit. on p. 82).
- Marte, a. et al. (Dec. 2002). "Feshbach Resonances in Rubidium 87: Precision Measurement and Analysis". In: *Physical Review Letters* 89.28, pp. 87–90. doi: 10.1103/PhysRevLett.89.283202 (cit. on p. 102).
- Marti, G. Edward et al. (2018). "Imaging Optical Frequencies with 100 μhz Precision and 1.1 μm Resolution". In: *Physical Review Letters* 120.10, p. 103201. doi: 10.1103/PhysRevLett.120.103201. arXiv: 1711.08540 (cit. on p. 15).
- Mathey, L. et al. (2009). "Collisional cooling of ultracold-atom ensembles using Feshbach resonances". In: *Physical Review A - Atomic, Molecular, and Optical Physics* 80.3, pp. 1–4. doi: 10.1103/PhysRevA.80.030702. arXiv: 0903.2568 (cit. on p. 104).
- Matthias, Jonas (2013). "Analyse einer optischen Dipolfalle für Kalium und Rubidium als Quelle für die Atominterferometrie". PhD thesis (cit. on p. 33).
- Metcalf, Harold J. et al. (1999). *Laser Cooling and Trapping*. Graduate Texts in Contemporary Physics. New York, NY: Springer New York, p. 1. doi: 10.1007/978-1-4612-1470-0 (cit. on pp. 42, 47, 62).
- Miller, J. D. et al. (1993). "Far-off-resonance optical trapping of atoms". In: *Physical Review A* 47.6, pp. 4567–4570. doi: 10.1103/PhysRevA.47.R4567. arXiv: arXiv:1011.1669v3 (cit. on p. 55).
- Milonni, Peter W. et al. (2010). *Laser physics*. Hoboken, New Jersey: Wiley (cit. on p. 47).
- Mishra, Hari Prasad et al. (2015). "Efficient production of an⁸⁷Rb F = 2, mF = 2 Bose-Einstein condensate in a hybrid trap". In: *European Physical Journal D* 69.2, pp. 1–8. doi: 10.1140/epjd/e2015-50843-y. arXiv: 1411.7628 (cit. on p. 105).
- Müller, Holger et al. (May 2008). "Atom Interferometry with up to 24-Photon-Momentum-Transfer Beam Splitters". In: *Physical Review Letters* 100.18, pp. 2–5. doi: 10.1103/PhysRevLett.100.180405 (cit. on p. 17).
- Müntinga, H. et al. (2013). "Interferometry with Bose-Einstein condensates in microgravity". In: *Physical Review Letters* 110.9, pp. 1–5. doi: 10.1103/PhysRevLett.110.093602. arXiv: 1301.5883 (cit. on pp. 19, 117).

- Nes, Johanna (2008). “Cold Atoms and Bose-Einstein Condensates in Optical Dipole Potentials”. PhD thesis (cit. on pp. 53, 73, 74).
- Nicholson, T L et al. (2015). “Optical Feshbach resonances: Field-dressed theory and comparison with experiments”. In: *Physical Review A - Atomic, Molecular, and Optical Physics* 92.2, pp. 1–15. DOI: 10.1103/PhysRevA.92.022709 (cit. on p. 118).
- NumPy (2018). *numpy.org* (cit. on p. 81).
- Nuske, Marlon et al. (2015). “Optimization of collisional Feshbach cooling of an ultracold nondegenerate gas”. In: *Physical Review A - Atomic, Molecular, and Optical Physics* 91.4, pp. 1–6. DOI: 10.1103/PhysRevA.91.043626. arXiv: 1412.8473 (cit. on p. 104).
- O’Hara, K. M., M. Gehm, et al. (Oct. 2001). “Scaling laws for evaporative cooling in time-dependent optical traps”. In: *Physical Review A* 64.5, p. 051403. DOI: 10.1103/PhysRevA.64.051403 (cit. on p. 79).
- O’Hara, K. M., S R Granade, et al. (1999a). “Ultrastable CO₂ laser trapping of lithium fermions”. In: *Physical Review Letters* 82.21, pp. 4204–4207. DOI: 10.1103/PhysRevLett.82.4204. arXiv: 0003049 [physics] (cit. on p. 55).
- O’Hara, K. M., S R Granade, et al. (1999b). “Ultrastable CO₂ laser trapping of lithium fermions”. In: *Physical Review Letters* 82.21, pp. 4204–4207. DOI: 10.1103/PhysRevLett.82.4204. arXiv: 0003049 [physics] (cit. on p. 73).
- Olson, Abraham J. et al. (2013). “Optimizing the efficiency of evaporative cooling in optical dipole traps”. In: *Physical Review A - Atomic, Molecular, and Optical Physics* 87.5, pp. 5–10. DOI: 10.1103/PhysRevA.87.053613. arXiv: 1211.3469 (cit. on pp. 78, 86, 114).
- Ospelkaus-Schwarzer, Silke (2006). “Quantum Degenerate Fermi-Bose Mixtures of 40K and 87Rb in 3D Optical Lattices”. PhD thesis. Universität Hamburg (cit. on p. 51).
- Overmeyer, Ludger et al. (2017). “Einstein-Elevator: A New Facility for Research from μg to 5 g”. In: *Gravitational and Space Research* 5.2, pp. 11–27 (cit. on p. 117).
- Paredes, Belén et al. (May 2004). “Tonks–Girardeau gas of ultracold atoms in an optical lattice”. In: *Nature* 429.6989, pp. 277–281. DOI: 10.1038/nature02530 (cit. on p. 100).
- Parker, Richard H. et al. (2018). “Measurement of the fine-structure constant as a test of the Standard Model”. In: *Science* 360.6385, pp. 191–195. DOI: 10.1126/science.aap7706 (cit. on p. 16).

Bibliography

- Pattinson, R. W. et al. (2013). "Equilibrium solutions for immiscible two-species Bose-Einstein condensates in perturbed harmonic traps". In: *Physical Review A - Atomic, Molecular, and Optical Physics* 87.1, pp. 1–7. DOI: 10.1103/PhysRevA.87.013625 (cit. on p. 118).
- Perrin, H el ene (2014). "Lecture 2 Doppler cooling and magneto-optical trapping Principle of Doppler cooling". In: *Les Houches lectures on laser cooling and trapping* (cit. on p. 58).
- Peters, A. et al. (2001). "High-precision gravity measurements using atom interferometry". In: *Metrologia* 38.1, pp. 25–61. DOI: 10.1088/0026-1394/38/1/4 (cit. on p. 17).
- Peters, A et al. (1999). "Measurement of gravitational acceleration by dropping atoms". In: *Nature* 400, pp. 849–852 (cit. on p. 16).
- Petrich, Wolfgang et al. (1994). "Behavior of atoms in a compressed magneto-optical trap". In: *Journal of the Optical Society of America B* 11.8, p. 1332. DOI: 10.1364/JOSAB.11.001332 (cit. on p. 59).
- Pfeiffer Vacuum GmbH (2013). *The Vacuum Technology - Know-how Book*. Vol. II (cit. on p. 115).
- Pinkse, P. W. H. et al. (1998). "One-dimensional evaporative cooling of magnetically trapped atomic hydrogen". In: *Physical Review A - Atomic, Molecular, and Optical Physics* 57.6, pp. 4747–4760. DOI: 10.1103/PhysRevA.57.4747 (cit. on p. 86).
- Prevedelli, M et al. (2014). "Measuring the Newtonian constant of gravitation G with an atomic interferometer". In: *Philosophical Transactions of the Royal Society A: Mathematical, Physical and Engineering Sciences* 372.2026, pp. 20140030–20140030. DOI: 10.1098/rsta.2014.0030 (cit. on p. 119).
- Pruvost, Laurence et al. (1999). "Guiding and cooling of cold atoms in a dipole guide". In: *Optics Communications* 166.1, pp. 199–209. DOI: 10.1016/S0030-4018(99)00233-3 (cit. on pp. 62, 101).
- Pu, H. et al. (1998). "Properties of two-species Bose condensates". In: *Physical Review Letters* 80.6, pp. 1130–1133. DOI: 10.1103/PhysRevLett.80.1130 (cit. on p. 118).
- Pyragius, Tadas (2012). "Developing and building an absorption imaging system for Ultracold Atoms". In: pp. 1–28. arXiv: 1209.3408 (cit. on p. 58).
- Python Software Foundation (2018). *Python.org* (cit. on p. 81).
- Raab, E. L. et al. (1987). "Trapping of Neutral Sodium Atoms with Radiation Pressure". In: *Physical Review Letters* 59.23, pp. 2631–2634. DOI: 10.1103/PhysRevLett.59.2631. arXiv: arXiv:1009.2475v1 (cit. on p. 42).

- Rasel, Ernst M. et al. (1995). "Atom wave interferometry with diffraction gratings of light". In: *Physical Review Letters* 75.14, pp. 2633–2637. doi: 10.1103/PhysRevLett.75.2633 (cit. on p. 16).
- Resch, Andreas (2016). "Hochstabiler optischer Resonator im Fallturmbetrieb für Präzisionsmessungen in Schwerelosigkeit". PhD thesis. Uni Bremen (cit. on p. 23).
- Roati, G. et al. (2007). "K39 Bose-Einstein condensate with tunable interactions". In: *Physical Review Letters* 99.1, pp. 1–5. doi: 10.1103/PhysRevLett.99.010403. arXiv: 0703714 [cond-mat] (cit. on p. 104).
- Rosi, G. et al. (2017). "Quantum test of the equivalence principle for atoms in coherent superposition of internal energy states". In: *Nature Communications* 8, pp. 6–11. doi: 10.1038/ncomms15529. arXiv: 1704.02296 (cit. on p. 21).
- Roy, Richard et al. (2016). "Rapid cooling to quantum degeneracy in dynamically shaped atom traps". In: *Physical Review A* 93.4. doi: 10.1103/PhysRevA.93.043403. arXiv: 1601.05103 (cit. on p. 101).
- Rudolph, Jan (2016). "Matter-Wave Optics with Bose-Einstein Condensates in Microgravity". PhD thesis (cit. on p. 36).
- Rudolph, Jan et al. (2011). "Degenerate quantum gases in microgravity". In: *Microgravity Science and Technology* 23.3, pp. 287–292. doi: 10.1007/s12217-010-9247-0 (cit. on p. 52).
- SAES (2007). "St 171® and St 172 - Sintered Porous Getters". In: (cit. on p. 32).
- SAES (2017). *St707 Non Evaporable Getters Activatable at Low Temperature , manufactured by SAES Pure Gas Inc., CA, USA*. (Cit. on p. 32).
- Savard, T. A. et al. (1997). "Laser-noise-induced heating in far-off resonance optical traps". In: *Physical Review A - Atomic, Molecular, and Optical Physics* 56.2, R1095–R1098. doi: 10.1103/PhysRevA.56.R1095 (cit. on p. 71).
- Schaetz, Tobias (2017). "Trapping ions and atoms optically". In: *J. Phys. B: At. Mol. Opt. Phys.* 50, p. 102001. doi: aa69b2 (cit. on p. 41).
- Schkolnik, V. et al. (2015). "The effect of wavefront aberrations in atom interferometry". In: *Applied Physics B: Lasers and Optics* 120.2, pp. 311–316. doi: 10.1007/s00340-015-6138-5. arXiv: 1411.7914 (cit. on p. 17).
- Schlamming, S. et al. (2008). "Test of the equivalence principle using a rotating torsion balance". In: *Physical Review Letters* 100.4, pp. 1–4. doi: 10.1103/PhysRevLett.100.041101. arXiv: 0712.0607 (cit. on p. 21).

Bibliography

- Schlippert, D. (2014). "Quantum test of the universality of free fall". PhD thesis (cit. on p. 62).
- Schlippert, D. et al. (2014). "Quantum test of the universality of free fall". In: *Physical Review Letters* 112.20, pp. 1–5. DOI: 10.1103/PhysRevLett.112.203002. arXiv: 1406.4979 (cit. on pp. 16, 21, 22).
- Schneider, Ch et al. (2010). "Optical trapping of an ion". In: *Nature Photonics* 4.11, pp. 772–775. DOI: 10.1038/nphoton.2010.236. arXiv: 1001.2953 (cit. on p. 41).
- Schulz, Matthias (2002). "Tightly confined atoms in optical dipole traps". PhD thesis, p. 177 (cit. on p. 71).
- Seidel, Stephan Tobias (2014). "Eine Quelle für die Interferometrie mit Bose-Einstein-Kondensaten auf Höhenforschungsraketen". PhD thesis. Uni Hannover (cit. on p. 29).
- Sesko, D. W. et al. (1991). "Behavior of neutral atoms in a spontaneous force trap". In: *Journal of the Optical Society of America B* 8.5, p. 946. DOI: 10.1364/JOSAB.8.000946 (cit. on p. 57).
- Sesko, D. et al. (1989). "Collisional losses from a light force atom trap". In: *Phys. Rev. Lett.* 63, 961.9, N–N. DOI: 10.1103/PhysRevLett.63.961 (cit. on p. 59).
- Shaevitz, Joshua W. (2006). "A Practical Guide to Optical Trapping". In: (cit. on p. 41).
- Shenoy-Hejamadi, Akshata et al. (2017). "Quantum Cryptography: Key Distribution and Beyond". In: *Quanta* 6.1, p. 1. DOI: 10.12743/quanta.v6i1.57. arXiv: arXiv:1802.05517v1 (cit. on p. 15).
- Shin, Y. et al. (2004). "Atom Interferometry with Bose-Einstein Condensates in a Double-Well Potential". In: *Physical Review Letters* 92.5, p. 4. DOI: 10.1103/PhysRevLett.92.050405. arXiv: 0306305 [cond-mat] (cit. on p. 16).
- Shoemaker, Curtis L. et al. (1981). *Feshbach Resonances in Chemical Reactions*. Vol. 14. C, pp. 169–240. DOI: 10.1016/S0065-3276(08)60328-7 (cit. on p. 119).
- Söding, J. et al. (1999). "Three-body decay of a rubidium Bose-Einstein condensate". In: *Applied Physics B: Lasers and Optics* 69.4, pp. 257–261. DOI: 10.1007/s003400050805. arXiv: 9811339 [cond-mat] (cit. on p. 72).
- Song, Ningfang et al. (2018). "Experimental Investigation of the Influence of the Laser Beam Waist on Cold Atom Guiding Efficiency". In: *Sensors* 18.3, p. 717. DOI: 10.3390/s18030717 (cit. on p. 73).
- Squires, Matthew B. et al. (2016). "Ex vacuo atom chip Bose-Einstein condensate". In: *Applied Physics Letters* 109.26. DOI: 10.1063/1.4971838. arXiv: 1608.04787 (cit. on p. 52).

- Stamper-Kurn, D. M. et al. (1998). “Reversible formation of a bose-einstein condensate”. In: *Physical Review Letters* 81.11, pp. 2194–2197. DOI: 10.1103/PhysRevLett.81.2194. arXiv: 9805022 [cond-mat] (cit. on p. 65).
- Steane, A.M. et al. (1992). “Radiation Force in the Magneto-Optical Trap”. In: *J. Opt. Soc. Am. B* 9.12, p. 2142. DOI: 10.1364/JOSAB.9.002142 (cit. on pp. 44, 45).
- Sternke, Tammo (2018). “An ultracold high-flux source for matter-wave interferometry in microgravity”. PhD thesis. Carl von Ossietzky Universität Oldenburg (cit. on pp. 19, 36).
- Storey, Pippa et al. (1994). “The Feynman path integral approach to atomic interferometry. A tutorial”. In: *Journal de Physique II* 4.11, pp. 1999–2027. DOI: 10.1051/jp2:1994103 (cit. on p. 17).
- Stuckenberg, Frank et al. (2018). *ATUS on GitHub* (cit. on p. 22).
- Surkov, E. L. et al. (1996). “Collisionless motion and evaporative cooling of atoms in magnetic traps”. In: *Physical Review A* 53.5, pp. 3403–3408. DOI: 10.1103/PhysRevA.53.3403 (cit. on p. 84).
- Suzaki, Yasuzi et al. (1975). “Measurement of the μm sized radius of Gaussian laser beam using the scanning knife-edge”. In: *Applied Optics* 14.12, pp. 2809–2810 (cit. on p. 48).
- Svoboda, K et al. (1994). “Biological Applications of Optical Forces”. In: *Annual Review of Biophysics and Biomolecular Structure* 23.1, pp. 247–285. DOI: 10.1029/PA002i006p00613 (cit. on p. 41).
- Szczepkowicz, Andrzej et al. (2009). “Optimal geometry for efficient loading of an optical dipole trap”. In: *Physical Review A - Atomic, Molecular, and Optical Physics* 79.1, pp. 1–6. DOI: 10.1103/PhysRevA.79.013408. arXiv: 0809.1999v2 (cit. on p. 56).
- Travis, Oliphant (2006). *Guide to NumPy*, p. 378 (cit. on p. 81).
- Treutlein, Philipp et al. (2001). “High-brightness atom source for atomic fountains”. In: *Physical Review A. Atomic, Molecular, and Optical Physics* 63.5, pp. 514011–514014. DOI: 10.1103/PhysRevA.63.051401 (cit. on p. 66).
- Wagner, T. A. et al. (2012). “Torsion-balance tests of the weak equivalence principle”. In: *Classical and Quantum Gravity* 29.18. DOI: 10.1088/0264-9381/29/18/184002. arXiv: 1207.2442 (cit. on p. 21).
- Wei, Chun Hua et al. (2017). “Raman sideband cooling of rubidium atoms in optical lattice”. In: *Chinese Physics B* 26.8. DOI: 10.1088/1674-1056/26/8/080701 (cit. on p. 66).

Bibliography

- Weiner, John et al. (1999). "Experiments and theory in cold and ultracold collisions". In: *Reviews of Modern Physics* 71.1, pp. 1–85. doi: 10.1103/RevModPhys.71.1 (cit. on pp. 64, 72).
- Wicht, Andreas et al. (2002). "Precision measurement of the fine structure constant based on atom interferometry". In: *Phys. Scr.* 82. doi: 10.1109/EQEC.2003.1314129 (cit. on p. 16).
- Will, Clifford M. (2009). "The confrontation between general relativity and experiment". In: *Proceedings of the International Astronomical Union* 5.S261, pp. 198–199. doi: 10.1017/S174392130999038X. arXiv: 0510072 [gr-qc] (cit. on p. 20).
- Will, Johannes (2007). "Realisierung einer Magneto-Optischen Falle für 41 K". In: (cit. on p. 53).
- Will, Sebastian (2012). *From Atom Optics to Quantum Simulation: Interacting Bosons and Fermions in Three-Dimensional Optical Lattice Potentials*. Springer Science & Business Media (cit. on p. 51).
- Williams, Jason et al. (2016). "Quantum test of the equivalence principle and space-time aboard the International Space Station". In: *New Journal of Physics* 18.2. doi: 10.1088/1367-2630/18/2/025018. arXiv: 1510.07780 (cit. on p. 21).
- Winoto, S L et al. (1999). "Laser cooling at high density in deep far-detuned optical lattices". In: *Physical Review A* 59.1, R19–R22. doi: 10.1103/PhysRevA.59.R19 (cit. on pp. 65, 66).
- Wolf, Joschka et al. (2017). "State-to-state chemistry for three-body recombination in an ultracold rubidium gas". In: *Science* 358.6365, pp. 921–924. doi: 10.1126/science.aan8721 (cit. on p. 72).
- Wolshrijn, B T et al. (2002). "Guiding of cold atoms by a red-detuned laser beam of moderate power". In: *New Journal of Physics* 4 (cit. on p. 62).
- Wu, Huang, Ennio Arimondo, et al. (1997). "Dynamics of evaporative cooling for Bose-Einstein condensation". In: *Physical Review A* 56.1, pp. 560–569. doi: 10.1103/PhysRevA.56.560 (cit. on p. 81).
- Wu, Huang and Christopher J. Foot (1996). "Direct simulation of evaporative cooling". In: *J. Phys. B* 29 (cit. on p. 80).
- Yanofsky, Noson S. (Aug. 2007). "An Introduction to Quantum Computing". In: doi: 10.1007/BF02877826. arXiv: 0708.0261 (cit. on p. 15).
- Zaiser, M. et al. (2011). "Simple method for generating Bose-Einstein condensates in a weak hybrid trap". In: *Physical Review A - Atomic, Molecular, and Optical Physics* 83.3, pp. 1–4. doi: 10.1103/PhysRevA.83.035601. arXiv: 1012.4222 (cit. on p. 106).

- Zaiser, Maic (2010). "Eine Quelle quantenentarteter Gase für die Atominterferometrie". PhD thesis (cit. on pp. 58, 73).
- ZARM (2009). *ZARM Drop Tower Bremen - User Manual*. 0 (cit. on p. 113).
- Zhang, Chuanwei et al. (2006). "Manipulation of single neutral atoms in optical lattices". In: *Physical Review A - Atomic, Molecular, and Optical Physics* 74.4, pp. 1–5. doi: 10.1103/PhysRevA.74.042316 (cit. on p. 100).
- Zhang, Hu et al. (2008). "Optical tweezers for single cells". In: *Journal of the Royal Society Interface* 5.24, pp. 671–690. doi: 10.1098/rsif.2008.0052 (cit. on p. 41).
- Zhou, Lin, Shitong Long, et al. (2015). "Test of Equivalence Principle at 10⁻⁸ Level by a Dual-Species Double-Diffraction Raman Atom Interferometer". In: *Physical Review Letters* 115.1, pp. 2–6. doi: 10.1103/PhysRevLett.115.013004. arXiv: 1503.00401 (cit. on p. 21).
- Zhou, Lin, Z. Y. Xiong, et al. (2011). "Development of an atom gravimeter and status of the 10-meter atom interferometer for precision gravity measurement". In: *General Relativity and Gravitation* 43.7, pp. 1931–1942. doi: 10.1007/s10714-011-1167-9 (cit. on p. 18).
- Zoest, Tim van et al. (2007). "Bose-Einstein condensation in microgravity". In: *Science* 328.5985. doi: 10.1126/science.1189164 (cit. on pp. 19, 52).

A. Danksagung

Die letzten Jahre waren intensiv, spannend und spaßig. Diesen, oft steinigen, Weg bin ich zum Glück nicht alleine gegangen und will die Gelegenheit hier nutzen um einer ganzen Reihe an Leute zu danken.

Zuallererst gilt mein Dank natürlich *Claus Lämmerzahl*, der die Rahmenbedingung für meine Promotion geschaffen hat. Er wird nicht müde, eine sehr breit aufgestellte Arbeitsgruppe zu führen, auch wenn das viele Abende und Wochenenden kostet.

Im selben Maße gilt mein Dank *Sven Herrmann*. Als Gruppenleiter hat er mir die Chance gegeben ein komplett neues, spannendes Feld der Physik zu ergründen. Sein lockerer Führungsstil und die vielen Freiheiten die er mir gelassen hat haben mich als Wissenschaftler weiter wachsen lassen. Er hat mir geschickt Verantwortung übertragen, ohne sie bei mir abzuladen.

Meinem Laborpartner *Sascha* danke ich dafür, dass er mir einen so leichten Einstieg in das Projekt ermöglicht hat. Von ihm habe ich gelernt Anleitungen zu lesen, bevor man etwas kaputt macht. Besonders hervorzuheben ist aber wohl das unglaublich gute Laborklima. Ich hätte mir keinen passenderen Kollegen wünschen können und außerdem ist sein Musikgeschmack wirklich gut! Ich wünsche ihm und seiner jungen Familie alles erdenklich Gute.

Meinen Bürokollegen *Andreas* und *Arne* danke ich für die netten Gespräche, einen Einblick in ihre Themen, die Hilfe bei Latex Problemen und ihren musikalischen Beitrag zu meiner Hochzeit.

Unseren Studenten *Nena*, *Nils* und *Jannik* möchte ich dafür danken, dass sie mir zugetraut haben ein Betreuer zu sein. Ich habe an euch jede Menge gelernt und will versuchen das in Zukunft zu nutzen.

Das Arbeitsumfeld am ZARM ist erfrischend und locker. Bei dem durchaus stressigen und auch frustrierenden Laboralltag, habe ich mich über die vielen Ablenkungen gefreut. Ich danke allen Kollegen der Gravi Gruppe für Volleyballturniere, Tischfußball pausen, Ensilada Abende, Freimarktsausflüge, Kohlfahrten, Geburtstage und wundervolle Hochzeiten.

Mein Dank bleibt jedoch nicht nur in Bremen. Zuallererst möchte ich hier ausdrücklich *Dennis Schlippert* danken. Er stand mir immer mit unglaublich präzisen Antworten und schwer zu

A. Danksagung

beschaffenden Bauteilen zur Seite. Außerdem hat er mir viele wichtige und gute Physiker in unserem Arbeitsgebiet vorgestellt, das hat mir wirklich geholfen!

In diesem Zuge seien auch alle anderen Mitarbeiter von Atlas genannt. Ich danke euch für die gute Zusammenarbeit.

Ein ganz besonderer Dank geht auch an *Ernst Rasel*. Zunächst danke ich ihm, dass er sich als Gutachter zur Verfügung gestellt hat. Wir haben uns in den vergangenen Jahren nicht besonders häufig gesehen, aber jedes einzelne Mal gab er mir das Gefühl wichtige und gute Arbeit zu leisten. Außerdem profitiere ich, aber auch das gesamte Projekt, von seiner kritischen Meinung, die einen davor bewahren kann, vorschnell zu handeln.

Marian will ich dafür danken, dass er mir während der Zeit des Schreibens den Rücken im Labor freigehalten hat und sich aufopferungsvoll um *mein* Experiment kümmert. Auch die letzte, sehr wichtige, Abwurfkampagne wäre ohne ihn kein Erfolg geworden.

Ich möchte der gesamten Quantus/Maius Familie danken, insbesondere aber natürlich den am Fallturm (ehemaligen) stationierten. Von "geliehenem" Laborequipment, zu Software Unterstützung, unser Projekt wäre ohne euch niemals so weit gekommen.

Einige wunderbare DPG-Tagungen und Quantus-Meetings haben mich aber auch den Rest der Truppe schätzen gelehrt. Ich danke euch allen für die hilfreichen Diskussionen, netten Worte und schönen Abende.

Viele der bisher genannten Menschen (und Kim) haben sich auch an der Fehlersuche und verbesserten Formulierung dieser Arbeit beteiligt. Dafür danke ich euch natürlich auch, die Arbeit ist dadurch unglaublich viel besser geworden.

Ein großes Dankeschön geht auch an alle technischen Mitarbeiter. FAB, Mechanik- und Elektronikwerksatt haben mir in verschiedensten Situationen freundlich und effektiv weitergeholfen.

Zu guter Letzt möchte ich auch meiner Familie für die Unterstützung danken. Ohne meinen Bruder, meine Eltern und meine Großeltern wäre ich heute nicht dort wo ich bin. Dafür danke ich euch.

Meiner Frau *Katrin* muss ich für zu vieles danken und fasse es mal so zusammen: Danke für die wundervolle Zeit.

Mein Sohn *Nikolas* hat nichts sinnvolles zu dieser Arbeit beigetragen. Für ihn bedeutet promovieren nur, dass Papa keine Zeit hat. Das ist jetzt zum Glück vorbei. Ich danke ihm dennoch dafür, dass er das Beste Kind der Welt ist.